PhD Thesis - Department of Earth Science, Freie Universität Berlin

Earth materials and processes on a molecular scale

Johannes Wagner
Matrikelnummer: 4212218

Berlin, July 2016

Promotionskommission

Prof. Dr. Timm John,	FU Berlin	(Vorsitzender)
Prof. Dr. Sandro Jahn,	U Köln	(Erstgutachter)
PD Dr. Ralf Milke,	FU Berlin	(Zweitgutachter)
Prof. Dr. Christiane Stephan,	FU Berlin	
Dr. Philipp Gleißner,	FU Berlin	

Tag der Disputation: 14.11.2016

Abstract

The present thesis deals with the investigation of geomaterials and processes on a molecular scale. Several application examples show how molecular simulation can augment and enhance our understanding of processes of the deep earth's interior. All examples describe parts of the processes of mineral-melt interactions in the mantle that comprise element mobilisation and redistribution. The first chapter provides a general introduction into the topic and how the individual chapters fit into the scope of the thesis. The second chapter thoroughly introduces the applied methods, namely molecular dynamics simulations and their theoretical framework. Chapter 3 discusses a combined simulation and experimental approach to investigate the structure of Y- and La-bearing aluminosilicate melts and glasses. Newly developed classical interaction potentials and first-principles methods are employed to investigate the local environment of Y and La depending on melt composition. Next to the insight gained into the structure of such complex melts, the benefits and drawbacks of the different simulation approaches are discussed. Chapter 4 also uses classical and first-principles simulations to develop a new tool for the prediction of trace element partition coefficients between silicate melts. A clear focus of this study lies on unravelling the influence of melt composition and structure on the partitioning behaviour of selected trace elements. Again, the findings are compared to experimental partitioning studies. The chapter shows that it is principally possible to predict element distributions between two given phases directly from molecular dynamics simulations. Chapter 5 investigates element transport properties in forsterite grain boundaries. Here, the focus lies on the influence of grain boundary structure on diffusion coefficients in aggregates typical for the upper mantle. The chapter concludes that there is a direct correlation between grain boundary excess volume and diffusion coefficient as well as a strong anisotropy in diffusion pathways, depending on the type of boundary. Chapter 6 summarises the findings of this thesis and discusses possible future developments and improvements to the applied methods.

Zusammenfassung

Die vorliegende Arbeit befasst sich mit der Untersuchung von Geomaterialien und Prozessen auf der atomaren Skala. In drei Fallbeispielen wird gezeigt, wie atomistische Simulationen unser Verständnis für Prozesse der tiefen Erde erweitern können. Im ersten Kapitel erfolgt eine allgemeine Einleitung in die Thematik. Ausführliche Einleitungen in die einzelnen Teilgebiete finden sich in den jeweiligen Kapiteln. Das zweite Kapitel führt umfassend in die angewandten Methoden ein, namentlich Molekulardynamik-Simulationen sowie die Theoriegebäude, die solchen Simulationen zugrunde liegen. Kapitel 3 befasst sich mit der Entwicklung klassischer Wechselwirkungspotentiale und deren Anwendung zur Strukturaufklärung komplexer, Y- und La-haltiger, silikatischer Schmelzen. Zur Bewertung werden experimentell bestimmte Strukturfaktoren der untersuchten Schmelzen herangezogen, dabei werden die Vor- und Nachteile der verschiedenen Simulationsmethoden diskutiert. Kapitel 4 nutzt ebenfalls diese klassischen Potentiale sowie quantenmechanische Simulationen für die Entwicklung neuer Methoden zur Vorhersage von Verteilungskoeffizienten verschiedener Spurenelemente zwischen silikatischen Schmelzen. Gleichzeitig wird dabei auf die strukturellen Eigenschaften der einzelnen Schmelzen und deren Auswirkung auf den Verteilungskoeffizient eingegangen. Kapitel 5 befasst sich mit Diffusionsprozessen an Korngrenzen und welche Rolle die Korngrenzstruktur bei solchen Prozessen spielt. In einem abschließenden Kapitel werden die Erkenntnisse der Arbeit zusammengefasst und Möglichkeiten zur Weiterentwicklung und Verbesserung der präsentierten Methoden diskutiert.

Contents

Chapter 1

Introduction

Our knowledge of the deep Earth's interior traditionally stems from two major sources. One is the interpretation of geophysical measurements, mostly of seismic wave velocities induced by earthquakes. It allows to infer physical properties of the material the wave propagates through and has lead to the established 'layered' model of the earth. The other source of information is the characterisation of natural rock samples that originate from the deep earth and are now exposed at the surface. Alternatively, geochemical laboratory experiments emulate conditions of the deep earth on a miniature scale in order to understand chemical and physical properties (phase reactions and stability, elastic properties, thermodynamic properties) of geologically relevant materials. Such experiments have often provided an explanation (e.g. in form of phase transitions) for deep earth phenomena observed by geophysics. To better understand the complex processes of the deep earth, it is mandatory to extensively study the individual subsystems involved. In the past years, a particular focus has been on the structure and properties of silicate melts (e.g. Mysen and Richet, 2005). As opposed to the solid mineral phases, reliable structure models for melts are still lacking and interpretation of experiments is far from straight forward, especially under the extreme pressure and temperature conditions of deep mantle environments. The use of computer simulations to investigate geoscientifically relevant materials and processes on all scales is a third approach that has established itself in the past decades. In particular on the scale of geomaterials, numerical simulations of minerals, melts and aqueous fluids can provide an additional perspective, namely a molecular scale view, onto a given geoscientific problem. It has so far been difficult to observe processes on the atomic scale, let alone directly investigate their influence on a macroscopic property (e.g. the heat capacity of a melt or diffusion coefficients of a mineral). With the steady increase of computing power over the last decades, it has become affordable to investigate evermore larger and com-

plex systems to resemble real experiments. Computer simulations, especially those based on density functional theory (DFT, see Chap. 2, also called 'first-principles' simulations) have the unique advantage that they empower us to calculate a thermodynamic property of interest at any given (extreme) condition while simultaneously provide insight into the molecular structure of a material. Ideally, such simulations not only deliver an explanation for experimentally observed phenomena but may make predictions for conditions that experiments can not reach. For these reasons, the annual number of publications in geoscience that involve computer simulations has steadily increased over the past years.

In this context, the present thesis has three distinct goals: (i) the development and application of methods to investigate silicatic systems, both ordered and unordered, (ii) development of structural models of silicate melts, -glasses and crystal defects and (iii) using these models to predict physical and chemical properties of geomaterials. At first, new types of classical interaction potentials are developed (see Sec. 2.3), one type by the author and one by co-workers. One of these is also formally implement into a molecular dynamics code framework (CP2K) by the author. In chapter 3, these potentials are tested regarding how well they perform to simulate complex aluminosilicate melts and glasses by investigating the structural environment of selected trace elements depending on melt composition. The results are benchmarked by comparing them to experimental studies as well as first-principles simulations. Subsequently, application examples of these models are discussed. Chapter 4 presents a new approach to predict trace element partitioning coefficients in silicate systems while simultaneously elucidating the structural driving factors that govern this partitioning. All simulations as well as data analysis and presentation have been conducted by the author. Chapter 5 investigates element transport properties in forsterite grain boundaries. The goal here is to elucidate how grain boundary structure hinders or enhances self diffusion in these grain boundaries and thus potentially influences element transport through a typical mantle aggregate. Here, another aim is to make the transition between discrete and continuous scales, showing that self diffusion and element redistribution depend strongly on grain boundary structure. The study is based on initial grain boundary structures developed by a co-worker. The simulations, data analysis and presentation have all been conducted by the author. Ultimately, all these studies describe parts of the processes of mineral-melt interactions in the mantle that comprise element mobilisation and redistribution.

Chapter 2

Computational methods

2.1 The molecular dynamics method

All studies in this thesis have in common that they employ the same method to simulate the behaviour of an arbitrary set of atoms over time: The molecular dynamics method (MD, Marx and Hutter, 2012). All atoms in a systems interact with each other and the energy of these interactions is described by a potential. At any temperature above 0 K, atoms move with a mean kinetic energy (E_{kin}) of

$$E_{kin} = \frac{3}{2} k_B T \tag{2.1}$$

where k_B is the Boltzmann constant and T the temperature. Their interactions impose forces ($\mathbf{F}$) on the atoms which relate to the potential (U) as

$$\mathbf{F} = -\nabla U \tag{2.2}$$

where ∇ is a differential operator (Nabla). With these forces, the new velocity is found by integrating Newtons equations of motion

$$\mathbf{F} = m \cdot a \tag{2.3}$$

where m is the atomic mass and a its acceleration. In molecular dynamics simulations, equation 2.3 is integrated numerically at each time step, and a new set of velocities and positions is assigned to each atom. The evolution of atomic velocities and positions is tracked in an atomic trajectory, which can subsequently be used to calculate average statistical properties of the system. To properly reflect the dynamics of such an atomic trajectory, the simulation step often has to be very small, usually 1 fs (10^{-15} s). In order to avoid surface effects when an atom reaches the boundary of the simulation cell, periodic

boundary conditions are applied in all simulations in this thesis. Essentially, an exact copy of the cell is repeated infinitely in all directions to the effect that atoms that cross a cell boundary are simply reintroduced at the opposite site (see Fig. 2.1).
Statistically, a system is described by a so called ensemble, which is defined by a set of observables that are in statistical equilibrium. There are several statistical ensembles that can be used in molecular simulations, depending on the property of interest (McQuarrie, 2000). The microcanonical ensemble (also called NVE ensemble) assumes that the system is isolated and not effected by any time dependent external forces. Thus, the simulation probes the system at constant number of particles (N), volume (V) and energy (E). However, since most laboratory experiments do not control the total energy of a system but rather the temperature, the most intuitive extension of the microcanonical ensemble is the canonical ensemble (NVT). Here, not the energy but the absolute temperature (T) is fixed during the simulation. Note however that the temperature, in contrast to N and V, is an intensive parameter of the system (i.e. independent of system size) with the kinetic energy of the particles as its extensive counterpart. NVT ensembles are realised by bringing the system in contact with a heat bath (thermostat) that is large compared to the system and assuming that no other external force interacts with it. Examples of such thermostats are the Nosé-Hoover thermostat (Nosé, 1984) or the *canonical sampling through velocity rescaling* (CSVR, Bussi et al, 2007) thermostat. Both correct deviations of the actual temperature by rescaling the atomic velocities by a certain factor, moving the systems dynamics closer to the desired temperature. Similarly, barostats algorithms may control the pressure (P) in NPE or NPT ensembles by periodically rescaling the atomic positions to result in the desired pressure.
However at the heart of every MD simulation stands the calculation of the total energy of the simulated system, necessary to derive the acting forces (Eq. 2.2). This is the computationally expensive part of such types of simulation, usually implemented using one of two approaches: the first-principles or *ab initio* approach is based on quantum mechanics and essentially parameter free, while classical MD relies on parametrised potentials and classical mechanics. Both methods are described in the following.

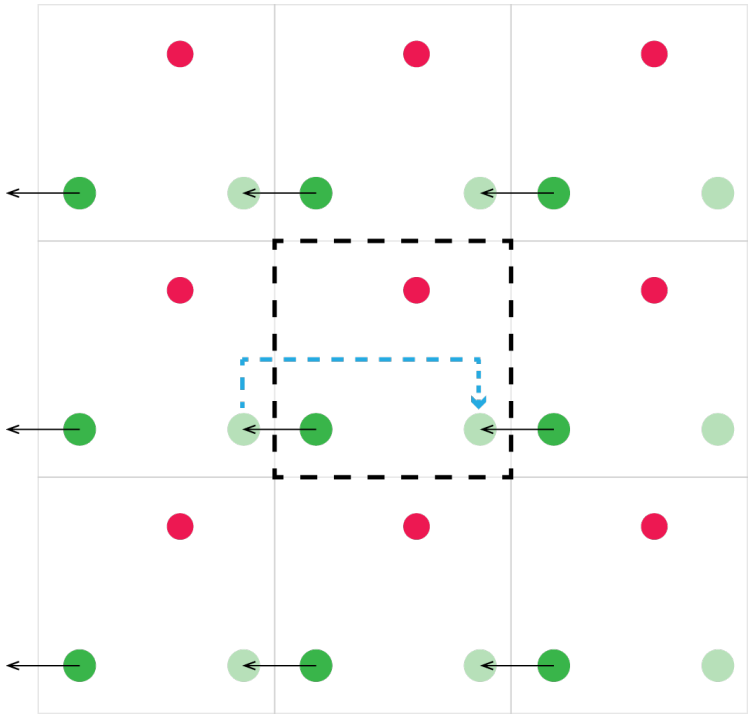

Figure 2.1: Sketch illustrating the principle of periodic boundary conditions in two dimension. The central simulation cell (bold dashed line) is repeated infinitely in each dimension (thin solid lines). If an atom is moved towards the outside of the initial simulation box, its periodic image is reintroduced at the opposite site.

2.2 First-principles simulations and density functional theory

Computer simulations of atomic systems that treat atomic interactions quantum mechanically are commonly referred to as first-principles or *ab initio* simulations. For the purposes of this thesis, the fundamental equation to be treated is the Schrödinger equation for a non-relativistic, non-spin-polarized system. As a first simplification, we treat electrons and atomic nuclei separately. This means nuclei are considered only in form of a potential acting on the electrons (the Born-Oppenheimer approximation) and all of the following considerations only depend on the electronic coordinates. For a single electron with coordinates $\mathbf{r}$ in an external potential $v_{ext}(\mathbf{r})$, the time independent Schrödinger's equation is given by

$$\hat{H}\Psi(\mathbf{r}) = \left[-\frac{\hbar^2\nabla^2}{2m} + v_{ext}(\mathbf{r})\right]\Psi(\mathbf{r}) = E\Psi(\mathbf{r}) \tag{2.4}$$

Here, $\hat{H}$ is called the systems Hamiltonian, $\Psi(\mathbf{r})$ its time independent wave function, m the mass and E the systems total energy. $\hbar$ is the Planck constant and ∇^2 the Laplace operator. If more than one electron is involved (which is the case in any system of interest in this thesis), one needs to solve a many-body problem. For N electrons, Eq. 2.4 is modified to

$$\left[\sum_i^N \left(-\frac{\hbar^2\nabla^2}{2m} + v_{ext}(\mathbf{r}_i)\right) + \sum_{i<j} U(\mathbf{r}_i, \mathbf{r}_j)\right]\Psi = E\Psi \tag{2.5}$$

where $U(\mathbf{r}_i, \mathbf{r}_j)$ is the electron-electron interaction, for a Coulomb system given by

$$U(\mathbf{r}_i, \mathbf{r}_j) = \frac{e^2}{|\mathbf{r}_i - \mathbf{r}_j|} \tag{2.6}$$

with e as the elementary charge. $v_{ext}(\mathbf{r}_i)$ contains the static potential from all electron-nuclei interactions of electron i and a constant term of nuclear-nuclear interactions. There are many methods to solve the many-body Schrödinger's equation such as Green's functions (Economou, 2006) or so called configuration interaction (CI) approaches (Sherrill and Schaefer III., 1999), however the computational power needed for systems containing more than a few electrons rapidly becomes unaffordable.
This is where density functional theory (DFT) offers an alternative by efficiently mapping the many-body problem back to the single-body problem of Eq. 2.4. One of the many properties that can be calculated by solving Schrödinger's equation is the particle density $n(\mathbf{r})$ for N particles

$$n(\mathbf{r}) = N \int d^3\mathbf{r}_2 \ldots \int d^3\mathbf{r}_N \Psi^*(\mathbf{r}, \mathbf{r}_1 \ldots \mathbf{r}_N)\Psi(\mathbf{r}, \mathbf{r}_1 \ldots \mathbf{r}_N) \tag{2.7}$$

which, for an electronic system, is essentially the probability to find an electron at a specific position (Parr and Yang, 1989). The essence of density functional theory is the Hohenberg-Kohn theorem (Hohenberg and Kohn, 1964) that states that Eq. 2.7 is invertible for a given ground state density $n_0(\mathbf{r})$. This means that from the ground-state density $n_0(\mathbf{r})$ one can infer the ground-state wave function $\Psi_0(\mathbf{r})$. In other words Ψ_0 is a *functional* of the *density* n_0 (a functional $F[f(x)]$ is a mapping from a function $f(x)$ to a number F). As a consequence, any ground state property (or observable) of the system has to be a functional of n_0 as well, and so is the energy E. Moreover, Hohenberg and Kohn (1964) could prove that n_0 always minimises the energy to the ground state energy E_0 so that

$$E_0 = E[n_0] \leq E[n'] \tag{2.8}$$

where n' is any electronic density other than the ground state density (Dreizler and Gross, 1990).
In this manner it is possible to map the problem of finding the energy depending on $3N$ variables to a problem of finding the minimum of the functional $E[n(\mathbf{r})]$, by inserting trial densities n($\mathbf{r}$) that only depend on three space variables. The only caveat remaining is that the actual form of $E[n(\mathbf{r})]$ is not explicitly known. To circumvent this, Kohn and Sham (1965) suggested to split the functional into a sum of known terms and an exchange-correlation term that would have to be approximated.

$$E[n(\mathbf{r})] = T_s[n(\mathbf{r})] + \int n(\mathbf{r}) v_{ext}(\mathbf{r}) d\mathbf{r} + \frac{e^2}{2} \iint \frac{n(\mathbf{r})n(\mathbf{r})'}{|\mathbf{r} - \mathbf{r}'|} + E_{xc}[n(\mathbf{r})] \tag{2.9}$$

where T_s is the kinetic energy functional of non-interacting electrons, expressed in so called Kohn-Sham orbitals. The second term contains electron-nuclei interactions and any additional external potentials while the third term (the Hartree-potential) describes the Coulomb interactions of electrons. All further quantum-mechanical complications of electron-electron interactions are now 'hidden' in the exchange correlation energy functional $E_{xc}[n(\mathbf{r})]$ and for this term, a variety of approximations have been proposed (Demichelis et al, 2010). The simplest (yet rather effective) of these is the local density approximation (LDA) where locally, the functional $E_{xc}[n(\mathbf{r})]$ is replaced by a partially parametrised *function* of the density. Other approximations are the generalised gradient approximation (GGA, e.g. Perdew et al, 1992, 1996) or hybrid

functionals such as B3LYP (Becke, three-parameter, Lee-Yang-Parr, Lee et al, 1988; Becke, 1993). Currently, GGA is the most commonly used approximation in standard DFT calculations but by no means always the best. The choice of an exchange correlation approximation depends strongly on the system and properties of interest and has to be considered carefully in each case. To further simplify the calculation, usually only valence electrons are treated explicitly. In this case v_{ext} contains the core electron contributions as well, in form of effective core potentials or so called pseudopotentials. The choice of pseudopotentials and exchange correlation functionals employed in the applications below is discussed in the individual chapters.

In this thesis, we apply two types of first-principles MD. The Born-Oppenheimer type (BOMD) is based on the time *independent* Schrödinger equation (Eq. 2.5) and the Born-Oppenheimer approximation described at the beginning of this chapter. It separates electronic and nuclear motion due to their difference in mass, assuming that fast electrons will quickly adjust to new positions of nuclei. The electronic ground state is calculated separately for each time step during the MD. The second type, Car–Parrinello molecular dynamics (CPMD) introduces additional degrees of freedom for electrons, thereby coupling the equations of motion for both nuclei and electrons (Car and Parrinello, 1985). This has the advantage that the electronic ground state is only converged once, allowing for often faster dynamic calculations compared BOMD. The energy of the (fictitious) electron dynamics then fluctuates around the energy of an equivalent BOMD. However, because CPMD attributes a very small (fictitious) mass to the electrons, integrating the equations of motion typically requires shorter time steps (0.1 fs) compared to BOMD (1-10 fs).

The last practical issue concerning DFT is the choice of basis sets to represent the Kohn-Sham orbitals (Eq. 2.9). For DFT calculations in periodic boundary conditions (which is the case in this thesis), plane waves have been shown to be the especially suitable (Ashcroft and Mermin, 1976; Gillan et al, 2006). For computational purposes, these plane waves are expanded in reciprocal space and a cutoff energy defines the extend of this expansion. The higher the cutoff, the higher the theoretical accuracy of the wave functions representation, the higher the computational load. To find a good compromise between efficiency and accuracy in terms of plane wave cutoff, usually convergence studies are done depending on the property of interest. E.g. if one is interested in the inner energy of a system up to a certain numerical accuracy, one would systematically increase the plane wave cutoff until the energy remains constant, up to the desired accuracy.

Despite all approximations and assumption discussed so far, DFT is currently the most powerful tool available to accurately simulate materials and their

properties, including many applications relevant in geoscience (e.g. determining lattice constants, finding phase transitions or calculating vibrational properties). However the computational effort limits the first-principles approach for MD calculations to systems containing up to a few hundred atoms and picoseconds of simulation time. For example, the computational effort for a standard Kohn-Sham based DFT simulation scales with at least M^3, where M is the number of basis functions. As a comparison, non DFT based first-principles methods usually even scale with up to $M^4 - M^7$. Thus, if one is interested in the long term dynamics of a systems or properties on a nanometre scale (e.g. the structure of a grain boundary or the intermediate-range structure of polyhedral chains in silicate melts) one often has to rely on a classical description of interatomic forces.

2.3 Classical interaction potentials

While first-principles calculations focus on electronic structure to calculate the state of a system, classical simulations consider atoms (and ions) as particles that directly interact through a potential (V), which in the sum, determines the systems energy. Interactions are modelled by (often analytical) functions that depend on the particle positions. The parameters of such models are optimised either to fit experimental data or higher theoretical methods (e.g. first-principles simulations). In this thesis, all systems of interest are ionic systems. A basic pair-potential form for such systems is the Born-Mayer form

$$V^{BM}(r^{ij}) = \frac{q^i q^j}{r^{ij}} + A^{ij} e^{-B^{ij} r^{ij}} - \frac{C^{ij}}{(r^{ij})^6} \tag{2.10}$$

where r^{ij} is the distance between two particles of species i and j, q is the (partial) charge, A, B and C are model parameters. The first term of Eq. 2.10 is the Coulomb interaction, the second term acts repulsive at very short range, ensuring that two atoms do not enter states of overlapping atomic radii. The last term is a dispersion term that acts attractive. Figure 2.2 shows such a potential and the contribution of individual terms. On closer look it becomes clear that the repulsive and attractive term quickly decay to zero, while the electrostatic term has non zero contributions even at long range. For this reason, short- and long range interactions are commonly distinguished in such models. Short range interactions by definition consider only the immediate surrounding of a particle. A usually spherical cutoff determines the boundary beyond which all additional (ideally minimal) contributions are neglected. This is done for two reasons: a) the number of pair interactions increases with

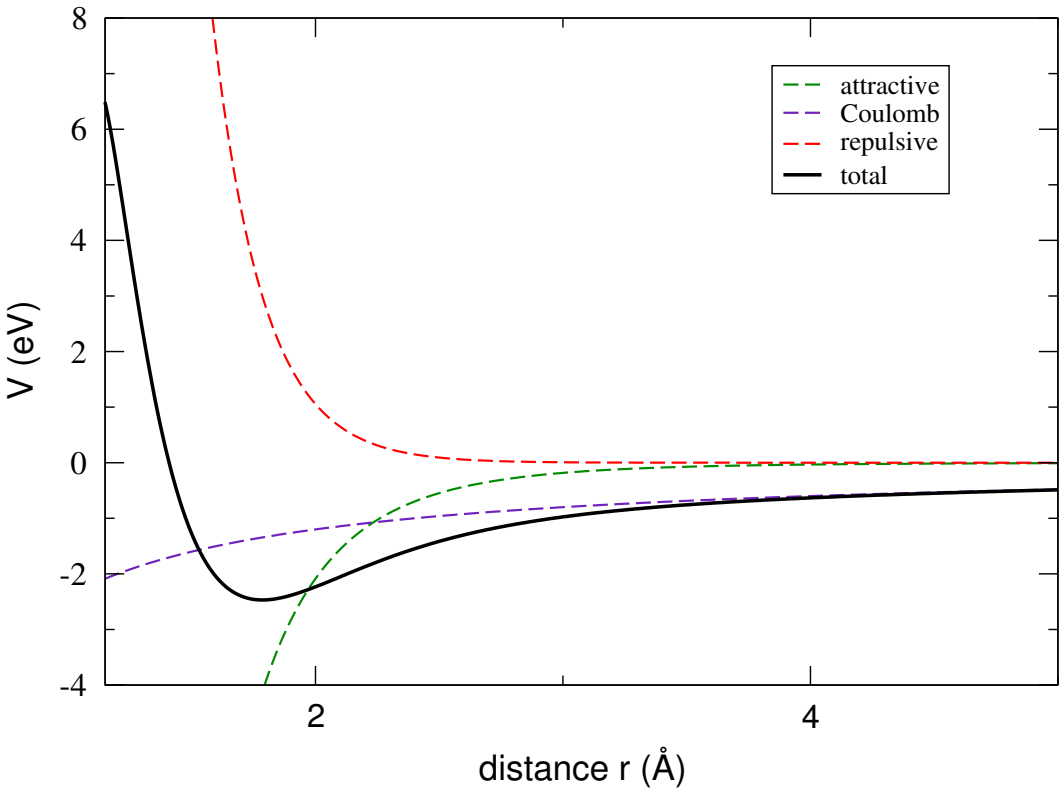

Figure 2.2: Plot of the total potential and individual contributions of a Born-Mayer type potential for Si-O (van Beest et al, 1990). Both the repulsive and attractive contributions quickly decay to zero (short range interactions), while the electrostatic (Coulomb) interaction still shows contributions at long range. In equilibrium, the average distance between the two ions would be the minimum of the total interaction potential (around 1.7 Å).

N^2 (N = number of particles) with distance, increasing the computational effort substantially while actual potential contributions are near zero and b) the application of periodic boundary conditions (Fig. 2.1) would imply that an atom interacts with itself. Long range interactions on the other hand take into account contributions of every atom in the cell. This will also raise problems in simulations that apply periodic boundary conditions (i.e. that formally involve an infinite number of atoms). There are several schemes to circumvent this, one of which is the Ewald summation method (also applied in first-principles calculations). This scheme splits a long range interaction into two terms, one that is quickly decaying and treated in real space, and one that is slowly decaying and treated on a grid in reciprocal space.
These pair wise additive potentials are usually parametrised to reproduce a certain property of a material faithfully. Conversely, they often fail to transfer to conditions that deviate to far from their training set. Moreover, as the explicit treatment of electrons is abandoned, such potentials fail to reproduce non-central forces that can be essential to describe e.g. elastic properties correctly (e.g. Price et al, 1987). This means that in an ideal case these models need to account not only for the classical electrostatic interaction but also quantum electronical effects as well, such as van der Waals repulsion and attraction as well as polarisation effects (Stone, 2008). One model that introduces the latter is the polarisable ion model (PIM, Wilson and Madden, 1993; Salanne et al, 2012b). In Chap. 3 we use such a model (dipolar polarisable ion model, DIPPIM), which is essentially an extension of Eq. 2.10 in the form of

$$\begin{aligned} V^{dippim}(r^{ij}) = &\overbrace{\sum_{i<j} \frac{q^i q^j}{r^{ij}}}^{\text{coloumb}} + \overbrace{\sum_{i<j} A^{ij} e^{-a^{ij} r^{ij}} + \sum_{i<j} B^{ij} e^{-b^{ij} r^{ij}}}^{\text{repulsive}} \\ &- \underbrace{\sum_{i<j} f_6^{ij}(r^{ij}) \frac{C_6^{ij}}{(r^{ij})^6}}_{\text{dispersive}} + \underbrace{V^{\text{pol}}(r^{ij})}_{\text{polarization}} \end{aligned} \tag{2.11}$$

Again, A, a, B, b and C are adjustable parameters. In this model, q^i and q^j are formal charges. The dispersion interactions include Tang-Toennies damping functions $f_6^{ij}(r^{ij})$ (Tang and Toennies, 1984) which yield corrections to the asymptotic $1/(r^{ij})^6$ behaviour at short distances and are defined as

$$f_6^{ij}(r^{ij}) = 1 - e^{-b_{disp}^{ij} r^{ij}} \sum_{k=0}^{4} \frac{(b_{disp}^{ij} r^{ij})^k}{k!} \tag{2.12}$$

where b_{disp}^{ij} is yet another parameter of the model. Finally, the last term on the right side of Eq. 2.11 takes into account the polarisation of the ions and contains Coulombic charge-dipole and dipole-dipole interactions as well as a self-energy term describing the energy cost to polarise an ion:

$$\begin{aligned} V^{\mathrm{pol}} = & \sum_{i<j,\alpha} \left[q_i \mu_j^\alpha f_D^{ij}(r^{ij}) - q_j \mu_i^\alpha f_D^{ji}(r^{ji}) \right] T_\alpha^{(1)} \\ & - \sum_{i<j,\alpha,\beta} \mu_i^\alpha \mu_j^\beta T_{\alpha\beta}^{(2)} + \sum_i \frac{|\boldsymbol{\mu}_i|^2}{2\alpha_i} \end{aligned} \tag{2.13}$$

Here, μ_i^α is the Cartesian component of the electric dipole moment of ion i in direction α. The interactions between ionic dipoles and charges q_i are modified at short distances by damping functions $f_D^{ij}(r^{ij})$ which account for additional dipoles induced by short-range interactions (Wilson and Madden, 1993). They have the same form as in Eq. 2.12, but now contain the parameter b_D^{ij} instead of b_{disp}^{ij}. We also use the short-hand notation $T_{\alpha\beta\ldots}^{(n)} = \nabla_\alpha \nabla_\beta \cdots 1/r^{ij}$ to denote the multipole interaction tensors, where the superscript gives the order of the derivative (Stone, 1996).

All models described so far treat particles as closed shell species or hard spheres (rigid ion models). For anions such as O^{2-}, this is possible because the confining potential in a specific phase stabilises the anion, i.e. the potential is tailored for a specific anion shape (Harding and Pyper, 1995) However the geometry of the oxygen anion in particular strongly depends on its local environment and thus, if a model is to be *transferable* between different phases and conditions, many-body effects which may reshape the ion can not be neglected, especially in ionic systems such as oxides and silicates (Salanne et al, 2012a). The potential mainly utilised in this thesis (quadrupolar aspherical ion model, QUAIM, Aguado et al, 2003; Jahn and Madden, 2007; Salanne et al, 2012a) is a further extension of the DIPPIM potential that aims to compensate for these issues and chooses a parametrisation to reproduce experimental data over a wide range of pressures and temperatures. The repulsive part of Eq. 2.11 is modified to account for shape deformations of oxygen anions, while maintaining a rigid ion model for cations. It also extends the multipole expansion up

to electronic quadrupoles. Here, the short range repulsive term has the form

$$V^{rep} = \sum_{i\in O, j\in cations} [A^{ij} e^{-a^{ij}\rho^{ij}} + B^{ij} e^{-b^{ij}\rho^{ij}} + C^{ij} e^{-c^{ij} r^{ij}}] + \sum_{i,j\in O} A^{OO} e^{-a^{OO} r^{ij}} + \sum_{i\in O} [D(e^{\beta\delta\sigma^i} + e^{-\beta\delta\sigma^i}) + (e^{\zeta^2|\nu^i|^2} - 1) + (e^{\eta^2|\kappa^i|^2} - 1)], \quad (2.14)$$

where

$$\rho^{ij} = r^{ij} - \delta\sigma^i - S^{(1)}_{\alpha}\nu^i_{\alpha} - S^{(2)}_{\alpha\beta}\kappa^i_{\alpha\beta}, \quad (2.15)$$

and summation of repeated indices is implied. $\delta\sigma^i$ characterises the deviation of the radius of oxide anion i from its default value, ν^i_{α} and $\kappa^i_{\alpha\beta}$ account for the dipolar respectively quadrupolar shape distortions. The last terms represent the energy penalty for deforming an anion with β, ζ and η as effective force constants. Additionally, the dispersion and polarisation terms of Eq. 2.11 are extended to account for quadrupolar polarisation effects (C, b_Q and c_Q, see below) but maintain the same general form (see Aguado et al, 2003; Madden et al, 2006; Jahn and Madden, 2007, for more details). Even utilising a comparatively complex model such as QUAIM, classical force fields still enable the simulation of systems containing several thousand atoms on up to nanosecond time scales. For the present thesis the QUAIM potential was implemented into the CP2K software package (Hutter et al, 2014) that supports first-principles as well as classical force field calculations. Details of the implementation are given in the appendix.

The model parameters used in this thesis have been originally derived from force-, dipole- and stress-matching with respect to density functional theory (DFT) for the System CaO-MgO-Al_2O_3-SiO_2 (CMAS) by Jahn and Madden (2007). For this work the model has been extended by adding interaction parameters for La, Y and Na while keeping all established parameters for other ions. Methodological details concerning the parametrisation can be found in Salanne et al (2012a), Madden et al (2006) and in the appendix. As a reference for the fitting procedure for the La parameters, five configurations of $La_4Al_8Si_{19}O_{56}$ melt were chosen on which we performed static DFT calculations. A similar procedure has been followed for Y and Na, only extended by several additional structure types and compositions (e.g. melts and solids of Na_2O, Y_2O_3 and $Y_3Al_5O_{12}$), to ensure the transferability of the potential to other applications. All parameters used in this study are listed in Table 2.1, parameters for the DIPPIM model parametrised by Haigis et al (2013) can be found in the appendix.

2.4 Putting MD to practice

After the theoretical treatment of the molecular dynamics method, the questions remains how to put it to practical use. A variety of codes have been developed for both first-principles MD (CPMD, CP2K, VASP, ABINIT) as well as classical force field calculations (LAMPS, CP2K, CHARMM). A typical simulation cell contains up to several thousand atoms in a classical-, and several hundred in a first-principles calculation. To generate an initial cell one provides a list of individual atoms that comprises atom types and positions. Depending on the system (e.g. a crystal or a fluid) the positions can either be taken from experimental data (e.g. crystallographic information) or randomly generated with some educated constraints (e.g. minimal distances between two atoms). In the latter case, the initial configuration is most likely far from equilibrium (or in fact resembles anything occurring in nature) and the atomic positions have to be relaxed according to their interaction potentials before the system can be studied. This can be achieved by minimising the interatomic forces. The size of the simulation box depends on the desired density, which can either be derived from experiments or by relaxing the cell parameters in a constant pressure simulation (NPT). Typical simulation times are in the order of nanoseconds for simple classical force fields and picoseconds for first-principles simulations.
From the MD trajectories one can calculate various properties that can be compared to laboratory experiments, such as lattice constants, elastic constants, temperature factors, structure factors and other thermodynamic properties (Frenkel and Smit, 2002). A fundamental structural parameter is the radial distribution function (RDF). RDFs represent the likelihood to find a specific pair of atoms at a distance r, normalised to the mean atomic number density. For individual atom types i and j the partial RDF is defined as

$$g_{ij}(r) = \frac{1}{c_i c_j \rho_0 N} \left\langle \sum_{a=1}^{N_i} \sum_{b=1}^{N_j} \delta(\mathbf{r} - (\mathbf{r}_a - \mathbf{r}_b)) \right\rangle \tag{2.16}$$

here, N is the total number of atoms, ρ_0 the atomic number density, c_i is the concentration and N_i number of atom type i. $\mathbf{r}_a$ and $\mathbf{r}_b$ are atomic position vectors of atoms a and b, $\mathbf{r}$ is a distance vector with length r. δ is the Kronecker delta. From the RDF one can infer not only the average bond distance of any specific element pair but also average coordination numbers n_i^j by integrating over the first peak of $g_{ij}(r)$ via

$$n_i^j = 4\pi\rho_0 c_j \int_0^{r_{min}} g_{ij}(r) r^2 dr \tag{2.17}$$

Conventionally, the integration is done up to the first minimum of $g_{ij}(r)$. The radial distribution function is also related to many properties such as the (x-ray and neutron) structure factor (see Chap. 3.4.4), the pressure or the compressibility.
Another property that can readily be extracted from MD trajectories is the mean squared displacement (MSD), which in turn relates to quantities such as the diffusion coefficient or the temperature factor. The MSD is a measure of the displacement of a particle over time, with respect to a reference point at time t_0

$$MSD(t) = \left\langle (\boldsymbol{r}(t+t_0) - \boldsymbol{r}(t_0))^2 \right\rangle \tag{2.18}$$

where ***r(t)*** is the position vector of a particle at time t, the angular brackets indicate averaging over time. Actual diffusion coefficients (D) can then be derived via Einstein's relation

$$D = \lim_{t\to\infty} \frac{MSD}{2 \cdot dim \cdot t} \tag{2.19}$$

where *dim* is the dimensionality of the system.
Another property of interest, in particular when it comes to chemical reactions, is the change in Helmholtz free energy. The free energy of a systems state can not directly be calculated from MD simulations. There are however methods to derive free energy *differences* between to states A and B, one of which is thermodynamic integration (Frenkel and Smit, 2002). If it is possible to calculate the potential energy (by classical or first-principles simulations) of the two states, it is also possible to define a new intermediate potential U after

$$U(\lambda) = U_A + \lambda(U_B - U_A) \tag{2.20}$$

where λ takes values between 0 ($U = U_A$) and 1 ($U = U_B$). The Helmholtz free energy (F) difference between A and B can then be written as the integral over the time averaged differences between U_A and U_B with respect to λ

$$F_B - F_A = \int_0^1 \left\langle \frac{\partial U_\lambda}{\partial \lambda} \right\rangle_\lambda d\lambda = \int_0^1 \langle U_B - U_A \rangle_\lambda d\lambda \tag{2.21}$$

Here, the angular brackets represent the averaging over time. The thermodynamic path taken during the integration can either be a real chemical- or an alchemical process (e.g. Kirkwood, 1935). In Chap. 4 we utilise such an alchemical process to transmute a trace element into a major element in order to predict element partition coefficients.

Table 2.1: QUAIM parameters in atomic units (see Jahn and Madden, 2007, for the columns O-O to Si-O, this work for the columns La-O, Y-O and Na-O). Interactions not listed or left blank here, e.g., cation-cation short-range repulsion, are taken to be absent in the model.

	O-O	Ca-O	Mg-O	Al-O	Si-O	La-O	Y-O	Na-O
A^{ij}	1068.0	40.058	41.439	18.149	43.277	99.958	99.518	19.152
a^{ij}	2.6658	1.5035	1.6588	1.4101	1.5418	1.608	1.795	1.5000
B^{ij}		50626.	59375.	51319.	43962.	10^7	626229.	40930.
b^{ij}		3.5024	3.9114	3.8406	3.9812	4.476	3.855	3.794
C^{ij}		6283.5	6283.5	6283.5	6283.5	6283.5	6283.5	6283.5
c^{ij}		4.2435	4.2435	4.2435	4.2435	4.2435	4.2435	4.2435
b_D^{ij}		1.8298	2.2148	2.2886	2.1250	2.1915	1.8660	1.6760
c_D^{ij}		2.3592	2.8280	2.3836	1.5933	3.4636	1.3725	2.2540
b_Q^{ij}		1.0711	1.9300	2.1318	1.9566	3.1336	2.2000	1.0000
c_Q^{ij}		1.0001	1.3317	1.2508	1.0592	3.5000	1.0000	1.4830
b_D^{ji}		3.4997					2.0651	
c_D^{ji}		1.0037					1.0003	
b_Q^{ji}		1.0947					1.2422	
c_Q^{ji}		1.0000					2.0666	
C_6^{ij}	44.372	2.1793	2.1793	2.1793	2.1793	2.1793	2.1793	2.1793
C_8^{ij}	853.29	25.305	25.305	25.305	25.305	25.305	25.305	25.305
b_{disp}^{ij}	1.4385	2.2057	2.2057	2.2057	2.2057	2.2057	2.2057	2.2057
α	8.7671	3.5000					3.0021	
C	11.5124	4.9789					2.4016	
D	0.49566							
β	1.2325							
ζ	0.89219							
η	4.3646							

Chapter 3

The structure of Y- and La-bearing aluminosilicate glasses and melts

This chapter is based on the following publication:
Wagner, J., Haigis, V., Leydier, M., Bytchkov, V. C., Fisher, H. E., Sadiki, N., Zanghi, D., Hennet, L. Jahn, S. (2016)
The structure of Y- and La-bearing aluminosilicate glasses and melts: a combined molecular dynamics and diffraction study
Chemical Geology (`http://dx.doi.org/10.1016/j.chemgeo.2016.12.036`)

Individual Contributions:
The following chapter is based on preliminary results published in the PhD thesis of Haigis (2013). In the present thesis the study was significantly extended by developing a new interaction potential and detailed comparison between the different models and experimental results. Passages in italics are directly adopted or partly modified from the thesis of Haigis (2013).
J. Wagner planned and performed research, parametrised the QUAIM potentials, performed QUAIM and first-principles simulations, analysed the data, participated in writing the paper.
V. Haigis planned and performed the research, parametrised the DIPPIM potentials, performed DIPPIM and first-principles simulations, analysed the data, participated in writing the paper.
V. C. Bytchkov, H. E. Fisher, N. Sadiki, D. Zanghi and L. Hennet provided experimental neutron and x-ray diffraction data.
S. Jahn planned and supervised the research, participated in writing the paper.

3.1 Introduction

Alkali and alkaline earth bearing (alumino)silicate glasses and melts have been studied extensively, due to their broad range of technological applications and their importance in geoscience. Hence, their structure and properties are relatively well understood (Stebbins et al, 1995; Mysen and Richet, 2005). On the other hand, aluminosilicates containing rare earth elements (REE) are less well studied but have recently attracted considerable interest owing to their remarkable properties and their use in various applications. They exhibit high glass transition temperatures, hardness and refractive indices as well as moderate thermal expansion coefficients (Shelby and Kohli, 1990; Iftekhar et al, 2011). REE-bearing aluminosilicate glasses have been proposed for optical devices (Kohli and Shelby, 1991; Tanabe, 1999). Since rare-earth elements represent analogues for actinides, these glasses have also been studied for applications in nuclear waste storage, and high corrosion resistance in the presence of aqueous fluids was found (Bois et al, 2002).

REE-bearing aluminosilicate glasses have been investigated by a range of experimental techniques, including nuclear magnetic resonance (NMR) (Schaller and Stebbins, 1998; Clayden et al, 1999; Marchi et al, 2005; Florian et al, 2007; Iftekhar et al, 2009, 2011), infrared spectroscopy (Clayden et al, 1999; Marchi et al, 2005) as well as neutron and x-ray diffraction (Wilding et al, 2002; Pozdnyakova et al, 2008; Simon et al, 2013). These techniques provide valuable insight into the local atomic structure of glasses such as coordination environments of the probed elements, glass network structures and vibrational properties. Often, the interpretation of experimental data relies on more or less heuristic assumptions about the atomic structure of the probed material. For instance, Iftekhar et al (2009) fitted a structural model to the measured NMR peak shifts and were able to extract information about the glass network connectivity from ^{29}Si signals alone. Another example is the interpretation of x-ray and neutron diffraction data: a common approach to obtain bond lengths and coordination numbers is to fit Gaussian peaks to the Fourier-transformed structure factor, i.e. to implicitly assume a specific structural model for the quantitative analysis of experimental data (Wilding et al, 2002; Pozdnyakova et al, 2008).

Molecular dynamics (MD) simulations are a particularly powerful and predictive method to generate three-dimensional structural models for disordered systems (Allen and Tildesley, 1987) and therefore yield information which is not directly accessible experimentally. To date, there are only a few classical MD studies on REE-bearing aluminosilicate glasses and melts: Du (2009) investigated low-silica (<40 mol%) yttrium aluminosilicates, and Iftekhar et al (2012) performed MD simulations of Y- and Lu-bearing glasses, with compo-

sitions containing less than 50 mol% SiO_2. Haigis et al (2013) used classical MD simulations to investigate structure of Y in (alumino)silicate melts, with different degree of network polymerization. Recently, Jaworski et al (2012) and Okhotnikov et al (2013) published results from classical MD simulations on aluminosilicate glasses also containing La.

The simulation of melts and glasses however also poses a fundamental challenge to the MD method: all predictions are dependent on the chosen interaction potentials and their applicability for a given set of conditions has to be tested carefully. Moreover, the MD method allows to simulate the motion of the individual atoms in the system over a certain time, and macroscopic quantities are then obtained by averaging over these atomic trajectories. *The statistical results are meaningful only to the extent that the phase space available to the system is sufficiently sampled during the simulation, i.e. that all relevant atomic configurations are visited during the MD run. It can be challenging to ensure that a system has reached equilibrium, especially in chemically complex systems such aluminosilicates. Particularly in glasses, structural relaxation is so slow that equilibrium certainly cannot be reached by atomistic simulations, which cover time spans of some tens of nanoseconds at best. Therefore, a simulated glass-structures will be trapped in one specific configuration and, within the simulation time, will not overcome the energy barriers which separate it from the remaining phase space. To address these issues, we used two complementary simulation approaches.*

Ab initio or first-principles MD is based on fundamental laws of nature (quantum mechanics) in the form of density functional theory (DFT Hohenberg and Kohn, 1964; Kohn and Sham, 1965) and yields a parameter-free description of arbitrary systems of atoms. Although some approximations have to be made for practical purposes, it is the most reliable method currently available and highly predictive in many cases. These qualities, however, come at the expense of high computational costs, which limits simulation times to some tens of picoseconds and system sizes to a few hundred atoms at most. For this study, we tackle the problem of insufficient sampling of glass configurations in ab initio MD simulations by raising the temperature, i.e. by simulating melts as analogues for glasses. The assumption of this approach is that melt structures represent a reasonable approximation to glass structures. To assess this, the effect of temperature will be investigated.

The ab initio simulations not only provide accurate structural information on melts but also serve as a benchmark for classical MD simulations, which constitute the second approach to modelling melt and glass structures. In the latter case, atomic interactions are described by a classical potential. Classical simulations are much less demanding in terms of computation time, but their

accuracy is not warranted and has to be tested carefully. Their computational efficiency allows simulated quenching of the melts to glasses at much lower rates than can be afforded with ab initio techniques (though still much faster than in experiments). The resulting glass structures can then be validated, e.g. by comparison to results from neutron and x-ray diffraction experiments. The potentials for REE-bearing aluminosilicates used here are an extension of already established and well tested sets of advanced polarisable ion potentials (Jahn and Madden, 2007; Haigis et al, 2013). It is desirable to further develop such accurate and transferable classical potentials, as they are a key to investigate complex geological systems such as mantle melts and solid solutions of mineral phases and the behaviour of trace elements therein.
Here, we present the results of a combined MD and neutron/x-ray diffraction study on yttrium- and lanthanum-bearing aluminosilicate melts and glasses, REE_2O_3-Al_2O_3-SiO_2 (REE = Y, La), with high silica content (76 mol% SiO_2). We utilize and compare more refined simulation methods than in cited previous work – new polarisable classical interatomic potentials and ab initio molecular dynamics – and systematically analyse the effects of interaction potential, temperature and quench rate on melt and glass structures. Keeping the molar fraction of SiO_2 fixed, the REE/Al ratio was varied between 0.09 and 0.5. We investigated the atomic-scale changes in the structure in response to 1) exchanging Y by La, 2) varying the REE content, i.e. the REE/Al ratio, of the system and 3) increasing the complexity of the classical interaction potential. A particular focus lies on the coordination environment of Y and La, as these are difficult to probe by the otherwise rather powerful NMR technique (Dupree et al, 1989; Schaller and Stebbins, 1998) and diffraction experiments (Leydier, 2010). Furthermore, we discuss the structural role of bridging oxygen in the aluminosilicate network and the status of the Al avoidance rule (Loewenstein, 1954) in disordered phases.

3.2 Simulation procedure

3.2.1 First-principles molecular dynamics for melts

We performed first-principles, Car-Parrinello molecular dynamics simulations using the CPMD code (Car and Parrinello, 1985; Marx and Hutter, 2000) of REE-bearing aluminosilicate melts of four different compositions, $REEAl_{11}Si_{19}O_{56}$ and $REE_4Al_8Si_{19}O_{56}$, where REE stands for either Y or La. Each simulation cell contained 174 atoms and was repeated periodically in space. Since these melts are considered here, in an approximate way, as an analogue for glasses, we chose the dimensions of the simulation cells such as to obtain the exper-

imentally determined density of the respective glass at room temperature, i.e. 2.91 g/cm^3, 2.97 g/cm^3, 2.94 g/cm^3 and 3.09 g/cm^3, respectively (Leydier, 2010).
Interatomic forces were determined within the framework of DFT, and the exchange-correlation functional was evaluated in the local density approximation (LDA). The interaction between ionic cores and valence electrons was described by Troullier-Martins pseudopotentials (Troullier and Martins, 1991). For Y, the semi-core 4s and 4p electrons were treated explicitly as valence electrons, additionally to the 4d and 5s orbitals. Similarly, for La, the semi-core 5s and 5p electrons were treated as valence electrons, additionally to the 5d and 6s orbitals. This allows for electric polarisability of the Y^{3+} and La^{3+} ionic cores. The cutoff for the expansion of the electronic wavefunctions into plane waves was 90 Ry, which was found sufficient to give converged results for the average melt structure. The reciprocal space of the simulation cell was sampled at the Gamma point only, which was sufficient to converge the interatomic forces.
The four simulation cells were pre-equilibrated at 3000 K for 50 ps with a classical MD simulation (see section 3.2.2) and further equilibrated for 5 ps using DFT. Data were collected from the following production runs of 10 ps to 15 ps duration. For the Car-Parrinello MD, the fictitious mass of the electronic degrees of freedom was 400 a.u., and the equations of motion were solved with a time step of 0.1 fs. The temperature of 3000 K and the kinetic energy of the fictitious degrees of freedom were controlled by Nosé-Hoover thermostat (Nosé, 1984; Hoover, 1985).

3.2.2 Classical molecular dynamics for melts and glasses

To evaluate the benefits and drawbacks of classical interaction potentials we use two types of these potentials with different complexity for the simulation of REE-bearing aluminosilicate melts and glasses. *In both cases, interactions between atoms are described by a polarisable ion model (Wilson and Madden, 1993). The first type of potential uses polarization up to a dipolar level and rigid, spherical ions (dipolar polarisable ion model, DIPPIM, see Chap. 2.3, Eqs. 2.11 to 2.13). It was parametrised for La-free compositions in a previous study (Haigis et al, 2013) and is extended here to include La. This modelling approach already adds true many-body effects to a simple pair potential through the inclusion of electronic polarization of oxygen, yttrium and lanthanum ions, determined self-consistently at each time step. This improvement with respect to a pure pair potential has been shown to be crucial for an adequate description of oxides (Rowley et al, 1998).* The second potential type includes polarization up to a quadrupolar level and treats oxygens as aspherical and deformable ions (quadrupolar aspherical ion model, QUAIM, see Chap. 2.3, Eq. 2.14) de-

pending on the anions local environment (Madden et al, 2006), determined self-consistently. Y- and La- free QUAIM-potentials were parametrised and successfully applied in previous studies, investigating a range of materials relevant in geoscience (Jahn and Madden, 2007). Details of the DIPPIM and QUAIM parametrisation and potential parameters can be found in Chap. 2.3 and the appendix.

One aim of the classical MD simulations is to generate structural models for the four REE-bearing aluminosilicate glasses instead of melts, which can then be validated by comparison to diffraction experiments. In order account for the problem of insufficient phase-space sampling, we first performed ab initio high-temperature simulations of melts of the four compositions, which display sufficiently fast dynamics to explore the entire phase space. Then 100 configurations were picked from each melt trajectory and used as starting configurations for subsequent quenching to room temperature. For each composition, we thus obtained a large set of different glass structures which were used for structural analysis.

Starting from the final atomic configurations of the four simulation cells from the *ab initio* simulations (each containing 174 atoms), *the cells were further equilibrated using classical MD for 10 ps at 3000 K, with a time step of 1 fs. The temperature was controlled by means of a Nosé-Hoover thermostat (Nosé, 1984; Hoover, 1985). Equilibration was followed by production runs of 50 ps duration with melts at 3000 K, from which we picked 100 starting configurations for the quench runs. During each of the latter, temperature was lowered by 100 K every 2 ps, down to 300 K, which corresponds to a quench rate of* $5 \cdot 10^{13}$ *K/s. Analysis was based on the last 1 ps of each quench run, and for each composition, an average over all the resulting glass structures is taken.*

We also checked that the results of the analysis are not affected by the finite size of the simulation cell: for the compositions $La_4Al_8Si_{19}O_{56}$ *and* $Y_4Al_8Si_{19}O_{56}$*, we simulated a glass using a simulation cell of eight times the original volume, and no significant changes were observed in the parameters discussed in this study, i.e. in the interatomic distances, coordination numbers, widths of coordination shells and overall structure factors. To check the influence of quench rate we additionally quenched one system using 10 times slower quench rates, also yielding no significant changes in the glass structure. However, we deliberately do not discuss even larger-scale network structures of the glasses (e.g., rings formed by tetrahedrally coordinated species), because these features are expected to be more heavily influenced by the periodic boundary conditions used here, and probably also by the rather high quench rate (Drewitt et al, 2012).*

3.3 Experimental procedure

3.3.1 Sample preparation

All glasses were synthesized by mixing commercially available oxides La_2O_3 (99.9% - Sigma-Aldrich), Y_2O_3 (99.9% - Sigma-Aldrich), Al_2O_3 (99.9% - Pechiney) and SiO_2 (99.5% - Prolabo). The powders were weighed and mixed together directly except La_2O_3 which was first annealed in an alumina crucible during 2 hours at 1100 °C to remove the anionic impurities (CO_3^{2-}, HO^-) and H_2O, then mixed with the other components and finally, heat-treated a second time. All mixtures were then melted in air at about 2000 °C during approximately 2 minutes on a water-cooled copper plate installed in a vertical axis laboratory solar furnace which deliver a power of 2 kW with an average solar flux of 900 - 1000 W/m^2. The temperature and melting time were chosen to ensure a good chemical homogeneity of the glasses as well as to prevent any modification of composition. The samples were cooled at a cooling rate of 200 °C/s, giving transparent quasi-spherical glass droplets between 4 and 6 mm in diameter. The glass compositions were measured by SEM-EDX analysis confirming the general formula for these glasses: $REE_xAl_{(12-x)}Si_{19}O_{56}$ where REE corresponds to Y or La.

3.3.2 Neutron diffraction

The neutron diffraction measurements were carried out on the D4C diffractometer (Fischer et al, 2002) at the Institut Laue Langevin (ILL) in Grenoble (France). In order to reduce the background, the samples were placed on a sample holder made with a thin vanadium foil and measurements were performed under vacuum. The empty holder was also measured for making the background subtraction. The neutron wavelength used was 0.4991 Å, giving a scattering vector range of 0.3-23.5 Å^{-1}. The theoretical background used for the data analysis is fully described in Fischer et al (2006). In a neutron diffraction experiment from a n-component material, the mean differential scattering cross section per atom can be written as:

$$\frac{1}{N}\left[\frac{d\sigma}{d\Omega}(Q)\right] = \left[\sum_{\alpha}^{n} c_\alpha \bar{b_\alpha}\right]^2 (S(Q)-1) + \sum_{\alpha}^{n} c_\alpha \bar{b_\alpha^2} \tag{3.1}$$

where c_α and b_α are respectively the atomic concentration and the coherent scattering length of species α present in the sample. The b_α values have been compiled by Sears (1992). $S(Q)$ is the total structure factor and is a weighted sum of the different partial $S_{\alpha\beta}(Q)$ for atomic species α and β as described

in equation 3.2. The principle for extracting the scattering cross section from the scattered intensity from the sample is to subtract the scattering from the entire sample environment and then normalize to a standard reference which is usually a vanadium sample. This procedure was performed using the program CORRECT (Wannberg et al, 1999) which corrects the data for attenuation, background, multiple scattering and inelasticity effects. $S(Q)$ is then calculated using Eq. 3.1.

3.3.3 X-ray diffraction

High energy x-ray diffraction measurements were made at the beamline ID11 at the European Synchrotron Radiation Facility (ESRF) in Grenoble (France). The incoming beam energy was 103.76 keV, corresponding to a wavelength of 0.1195 Å. Two-dimensional diffraction patterns were measured using a fast readout low noise (FReLoN) charge-coupled device detector manufactured by the ESRF (Labiche et al, 2007). In order to increase the accessible Q range the scattered beam was centred at the corner of the detector. As the highest resolution is achieved at larger sample to detector distances whereas shorter distances provide a higher scattering angle coverage, diffraction measurements were perfomed at two separate sample to detector distances of D1 = 394.344 and D2 = 173.147 mm. The diffraction data were corrected for dark current noise, geometrical effects and incident beam polarization and reduced to one-dimensional patterns using the program FIT2D (Hammersley et al, 1996). The individual diffraction patterns were normalized to the incident beam monitor and an average taken for the intensities measured at each sample to detector distance. The high-Q data taken at D2 was merged with the data taken at D1 giving a usable Q range of 0.3-20 Å^{-1} (High-Q limitation due to problems with the detector at large angle). Following the procedure described by Hennet et al (2002), the data were corrected for background, multiple and compton scattering and for attenuation. The structure factor is then calculated using Eq. 3.1 where b_α is repaced by the x-ray atomic scattering factor f_α.

3.4 Results

3.4.1 Ab initio MD of melts at 3000 K

From the trajectories of the ab initio MD simulations at 3000 K for each composition, the coordination environment of the cations has been extracted. Fig. 3.1 and Fig. 3.2 show the radial distribution functions $g_{XO}(r)$ (X = Y/La, Al, Si, O) for the Y-bearing and the La-bearing melts, respectively. The average

coordination number of a cation X is calculated as the average number of oxygen ions around the cation within a cutoff radius r_{cut}^{XO}, which is given by the first minimum of the respective radial distribution function $g_{XO}(r)$ for the pair $X-O$. The minimum has been determined by a polynomial fit to the minimum region and depends (weakly) on composition. This dependence results from the change in shape of the first coordination shell which accompanies variations in composition. In Table 3.1, we list the results characterizing the first coordination shell of the different cations. *The average cation-oxygen bond length d_{XO} is calculated as the average distance between a cation X and oxygen for pairs closer than r_{cut}^{XO}. We also determined the first maximum $\hat{d}_{XO}$ of the function $r^2 g_{XO}(r)$, i.e. the most probable $X-O$ bond length, using a polynomial fit to the maximum region. This maximum does not coincide with the average bond length in general, and the difference between the two quantities is a measure for the radial asymmetry of the first coordination shell. Finally, the standard deviation σ of the distribution of cation-oxygen bond lengths was determined, giving a measure for the width of the coordination shell.*

Table 3.1: *Ab initio MD results for the first coordination shell around cations in melts at 3000 K: cutoff radius r_{cut} for cation-oxygen pairs, average coordination number CN, average bond length d, most probable bond length $\hat{d}$ and standard deviation σ of cation-oxygen bond lengths (a measure for the width of the coordination shell).* Table from Haigis (2013).

cation	r_{cut} (Å)	CN	d (Å)	$\hat{d}$ (Å)	σ (Å)
$YAl_{11}Si_{19}O_{56}$ melt					
Si	2.32	4.1	1.69	1.63	0.151
Al	2.61	4.7	1.93	1.78	0.249
Y	3.25	7.9	2.53	2.26	0.359
$Y_4Al_8Si_{19}O_{56}$ melt					
Si	2.31	4.1	1.69	1.63	0.150
Al	2.57	4.5	1.91	1.78	0.232
Y	3.22	7.1	2.50	2.25	0.348
$LaAl_{11}Si_{19}O_{56}$ melt					
Si	2.36	4.2	1.70	1.63	0.161
Al	2.60	4.7	1.93	1.78	0.243
La	3.41	8.2	2.72	2.45	0.376
$La_4Al_8Si_{19}O_{56}$ melt					
Si	2.38	4.1	1.69	1.63	0.153
Al	2.55	4.3	1.89	1.77	0.223
La	3.44	7.9	2.71	2.43	0.388

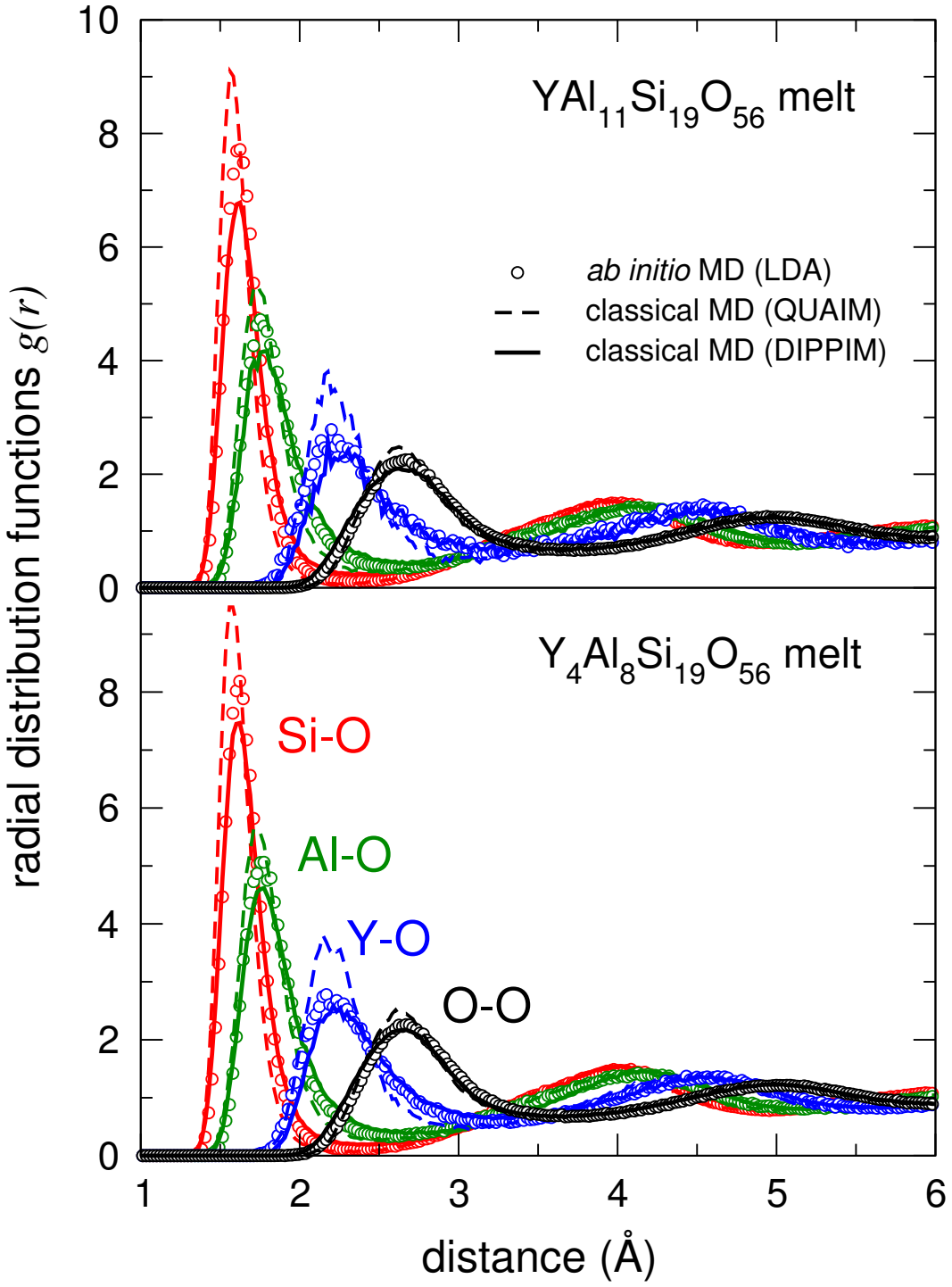

Figure 3.1: Radial distribution functions $g(r)$ for O-O and cation-O pairs in $YAl_{11}Si_{19}O_{56}$ melt (upper panel) and $Y_4Al_8Si_{19}O_{56}$ melt (lower panel), at 3000 K. Circles: *ab initio* MD, full lines: classical MD DIPPIM, dashed: classical MD QUAIM (see section 3.4.2).

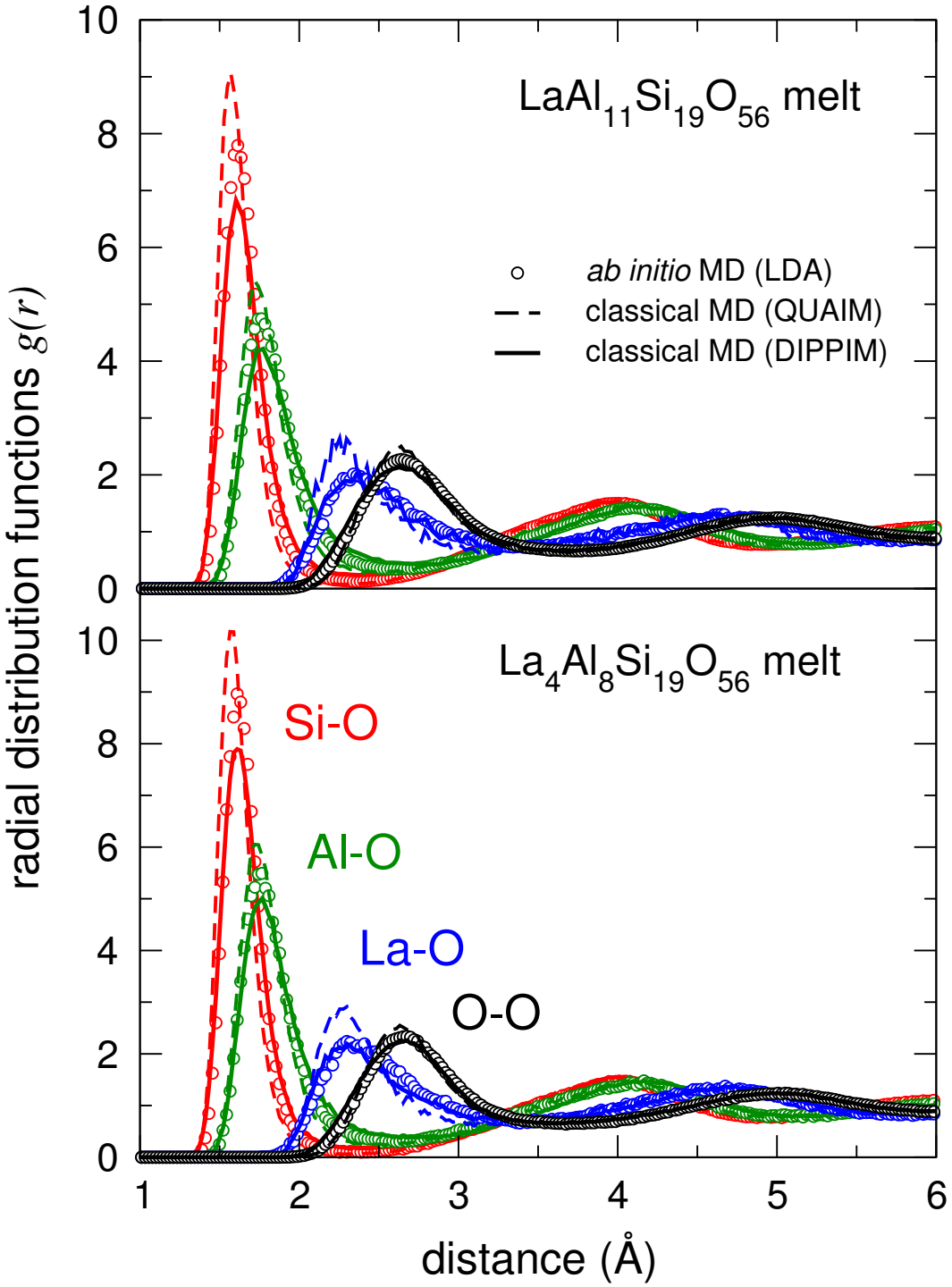

Figure 3.2: Radial distribution functions $g(r)$ for O-O and cation-O pairs in $LaAl_{11}Si_{19}O_{56}$ melt (upper panel) and $La_4Al_8Si_{19}O_{56}$ melt (lower panel), at 3000 K. Circles: *ab initio* MD, full lines: classical MD DIPPIM, dashed: classical MD QUAIM (see section 3.4.2).

As a result, it is found that the coordination shells of the different cations exhibit different sensitivities to changes in melt composition: the first-shell environment of Si is virtually the same for all melts, with a coordination number around 4.1, a Si-O average bond length around 1.69 Å and a most probable bond length of 1.63 Å. On the other hand, the coordination of Al shows a slight, but systematic variation with melt composition: for a given REE (Y or La), the coordination of Al by oxygen decreases for increasing REE content, and so does the average Al-O bond length. Moreover, the Al coordination number is smaller in the La-rich melt than in the corresponding Y-rich melt. Finally, also the coordination environments of Y and La are clearly sensitive to compositional changes. Coordination numbers decrease with increasing REE content, and for Y, this change is accompanied by a shortening of the bonds to the nearest oxygen ions.

The average coordination numbers listed in Table 3.1 are the mean of a range of coordination numbers occuring in the melt structure. The distribution of different coordination environments of Y and La for given melt compositions is shown in Fig. 3.3. The coordination numbers span a wide range, with significant contributions coming from 5- to 10-fold coordination of the REE cation by oxygen. With increasing REE content, the distributions shift to lower coordination numbers. A similar plot for the coordination of Al in the different melts is shown in Fig. 3.4. Most Al atoms are 4-, 5- or 6-fold coordinated by oxygen, and two trends in the coordination distribution are observed: first, the distribution shifts to lower coordination numbers for increasing REE content, and second, the distribution is shifted to lower numbers if Y is replaced by La, especially for the REE-rich compositions.

The medium range order of silicate melts and glasses is commonly discussed in terms of the tetrahedral network formed by fourfold coordinated Si and Al, and its perturbation by network modifiers (Mysen and Richet, 2005). In the analysis of our first-principles MD data, we follow this line, putting an emphasis on the various oxygen species which link the building blocks of the structure. Tetrahedrally, i.e. 4-fold coordinated Si and Al are counted as network formers (T), and oxygen is considered bridging (BO) if it links exactly two such tetrahedra. A terminal oxygen, which is bonded to only one T species, is referred to as non-bridging (NBO). Note that according to this terminology, an oxygen atom linking, for instance, a tetrahedrally coordinated Si and a fivefold coordinated Al atom is counted as non-bridging. The ratio NBO/T is a measure for the depolymerization of the melt or glass network. Finally, an oxygen atom which belongs simultaneously to three coordination tetrahedra around T is termed an oxygen tricluster. Note that there are oxygen atoms which do not fall into any of the mentioned categories, e.g. oxygen bonded to two five-

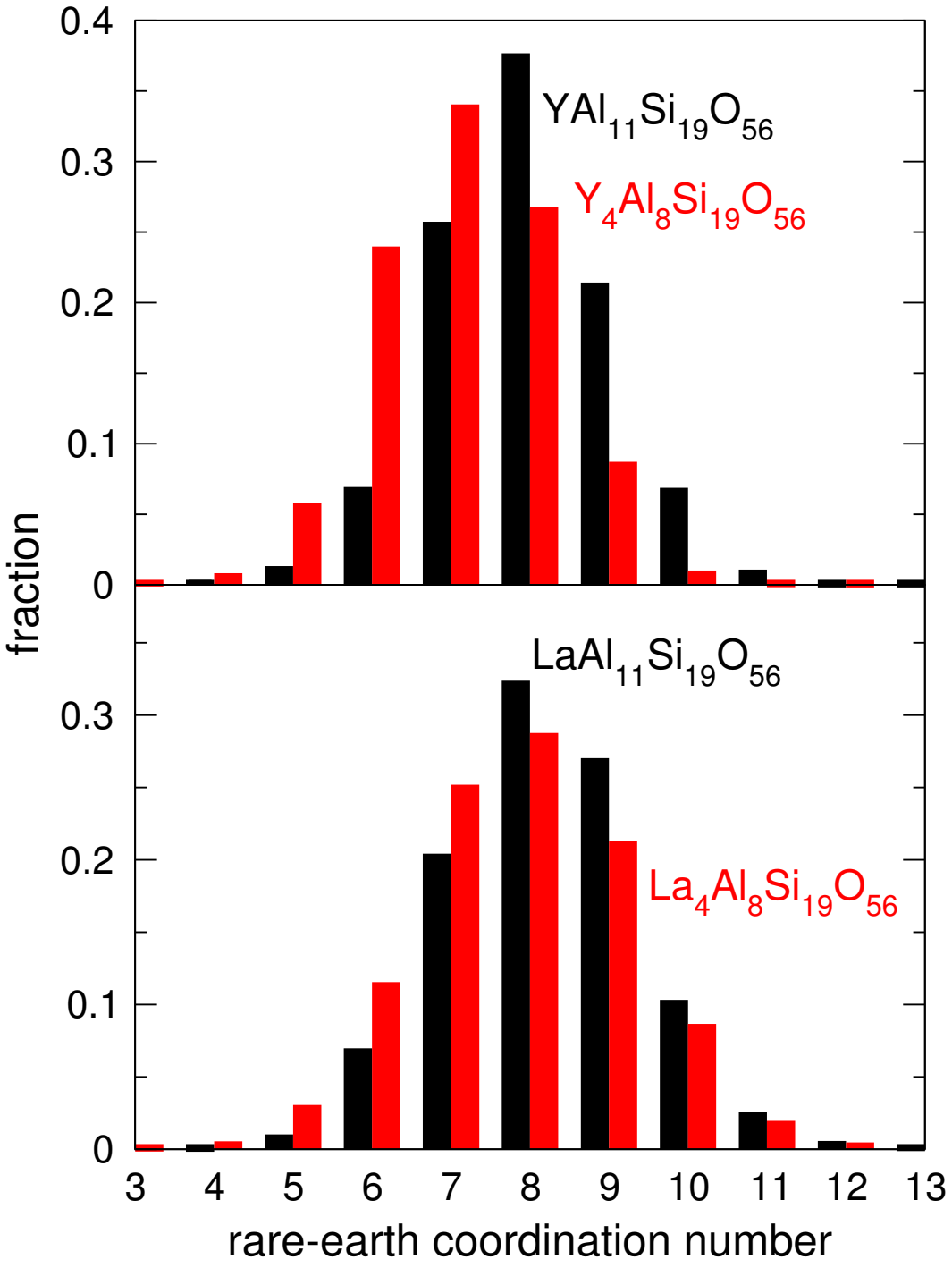

Figure 3.3: *Ab initio MD: distribution of coordination numbers of Y and La as a function of melt composition, with low (black) and high (red) REE content.* Figure from Haigis (2013).

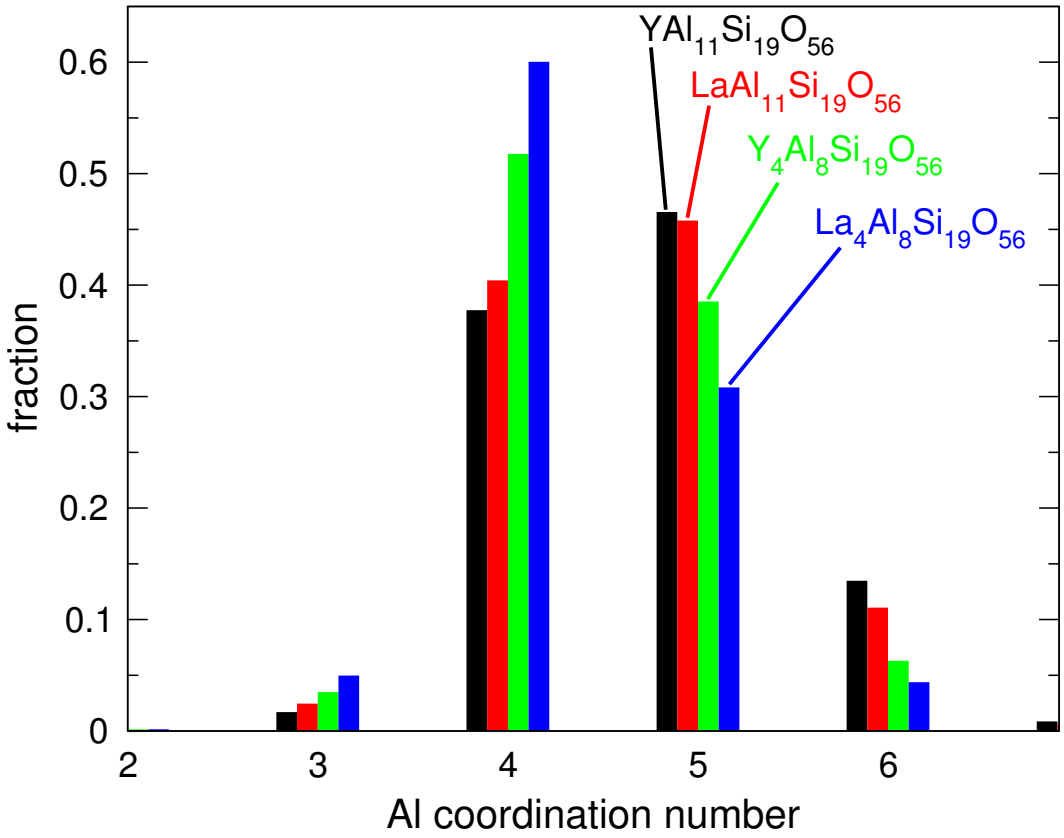

Figure 3.4: *Ab initio MD: distribution of coordination numbers of Al as a function of melt composition.* Figure from Haigis (2013).

fold coordinated Al atoms. The results of this analysis are listed in table 3.2. Whereas Si occurs predominantly as tetrahedrally coordinated network former T, less than half of Al is in T configuration in the REE-poor melts. NBO/T values are larger than 1 for all compositions, which indicates a substantial depolymerization of the network. Small amounts of oxygen triclusters (< 5%) are observed throughout.

Table 3.2: *Parameters describing melt network structure derived from ab initio MD: the fractions [Si_{IV}]/[Si] and [Al_{IV}]/[Al] of fourfold coordinated Si and Al, respectively, determine the abundance of tetrahedrally coordinated species, and NBO/T is the ratio of non-bridging oxygen to tetrahedrally coordinated species. The fraction of bridging oxygen linking T and T′, with respect to the total number of bridging oxygen, is denoted by x_{BO}(T-O-T'), the BO fractions expected for a random distribution by $x_{\mathrm{BO}}^{\mathrm{rand}}$(T-O-T'), as well as amount of oxygen triclusters [O_{tri}]/[O].* Table from Haigis (2013).

	$YAl_{11}Si_{19}O_{56}$	$Y_4Al_8Si_{19}O_{56}$	$LaAl_{11}Si_{19}O_{56}$	$La_4Al_8Si_{19}O_{56}$
[Si_{IV}]/[Si]	0.851	0.879	0.817	0.877
[Al_{IV}]/[Al]	0.377	0.517	0.404	0.600
NBO/T	1.145	1.123	1.179	1.028
x_{BO}(Si-O-Si)	0.633	0.617	0.598	0.551
x_{BO}(Si-O-Al)	0.326	0.345	0.351	0.423
x_{BO}(Al-O-Al)	0.041	0.038	0.052	0.025
$x_{\mathrm{BO}}^{\mathrm{rand}}$(Si-O-Si)	0.630	0.638	0.600	0.599
$x_{\mathrm{BO}}^{\mathrm{rand}}$(Si-O-Al)	0.333	0.326	0.355	0.355
$x_{\mathrm{BO}}^{\mathrm{rand}}$(Al-O-Al)	0.038	0.036	0.045	0.046
[O_{tri}]/[O]	0.022	0.024	0.024	0.046

3.4.2 Classical MD of melts at 3000 K

The reliability of the two classical interaction potentials (DIPPIM and QUAIM) can be assessed by comparison of its predictions either to ab initio results or to experimental data. Here, we first check melt structures derived from classical MD at 3000 K against the ones obtained from Car-Parrinello simulations (see section 3.4.1). A comparison with diffraction data will be made in section 3.4.4. The radial distribution functions for X-O pairs (X = Y/La, Al, Si, O) are plotted along with the DFT results in Figs. 3.1 and 3.2. When comparing the two classical potentials types, peak positions are reasonably well

reproduced while peak heights are systematically underestimated (DIPPIM) respectively overestimated (QUAIM) compared to first-principles data. In Table 3.3, we list structural parameters of the four melts as obtained from classical MD for both potential types, which can be compared to the ab initio results in Table 3.1. In the DIPPIM case, Al coordinations are systematically overestimated while the QUAIM potential underestimates especially La coordination numbers. Moreover, the DIPPIM potential predicts a strong variation of the most probable La-O distance with changing melt composition (decrease over 0.1 Å), not observed to such extent in the *ab initio* simulations.

Table 3.3: Classical MD (^{di} for DIPPIM, ^{qu} for QUAIM) results for the first coordination shell around cations in melts at 3000 K: cutoff radius r_{cut} for cation-oxygen pairs, average coordination number CN, average bond length d, most probable bond length $\hat{d}$ and standard deviation σ of cation-oxygen bond lengths (a measure for the width of the coordination shell).

cation	$\mathrm{CN}^{di\|qu}$	$d^{di\|qu}$ (Å)	$\hat{d}^{di\|qu}$ (Å)	σ (Å)
		$YAl_{11}Si_{19}O_{56}$ melt		
Si	4.3 | 4.0	1.72 | 1.64	1.63 | 1.59	0.197
Al	5.1 | 4.3(1)	2.00 | 1.85	1.80 | 1.75	0.294
Y	7.5 | 7.2(2)	2.57 | 2.40	2.31 | 2.22	0.351
		$Y_4Al_8Si_{19}O_{56}$ melt		
Si	4.2 | 4.0	1.71 | 1.64	1.63 | 1.59	0.188
Al	4.9 | 4.2(1)	1.97 | 1.85	1.79 | 1.76	0.284
Y	7.3 | 6.9(1)	2.55 | 2.38	2.29 | 2.21	0.357
		$LaAl_{11}Si_{19}O_{56}$ melt		
Si	4.3 | 4.0	1.72 | 1.64	1.63 | 1.59	0.191
Al	5.2 | 4.3(1)	2.01 | 1.85	1.79 | 1.76	0.308
La	7.5 | 7.1(2)	2.67 | 2.56	2.46 | 2.32	0.353
		$La_4Al_8Si_{19}O_{56}$ melt		
Si	4.2 | 4.0	1.70 | 1.64	1.63 | 1.59	0.177
Al	4.8 | 4.1	1.96 | 1.84	1.78 | 1.75	0.285
La	7.0 | 6.7(1)	2.65 | 2.55	2.35 | 2.30	0.367

3.4.3 Diffraction experiments on glasses

Figures 3.5 and 3.6 show the measured as well as simulated (see below) neutron and x-ray structure factors $S_N(Q)$ and $S_X(Q)$. Neutron scattering data show rather similar features for all measured compositions and REE concentrations.

X-ray structure factors on the other hand show significant differences with varying REE concentration, such as a splitting and flattening of the main peak around 4 Å. For $Y_4Al_8Si_{19}O_{56}$, the corresponding pair distribution functions calculated from these structure factors is shown in Fig. 3.7.

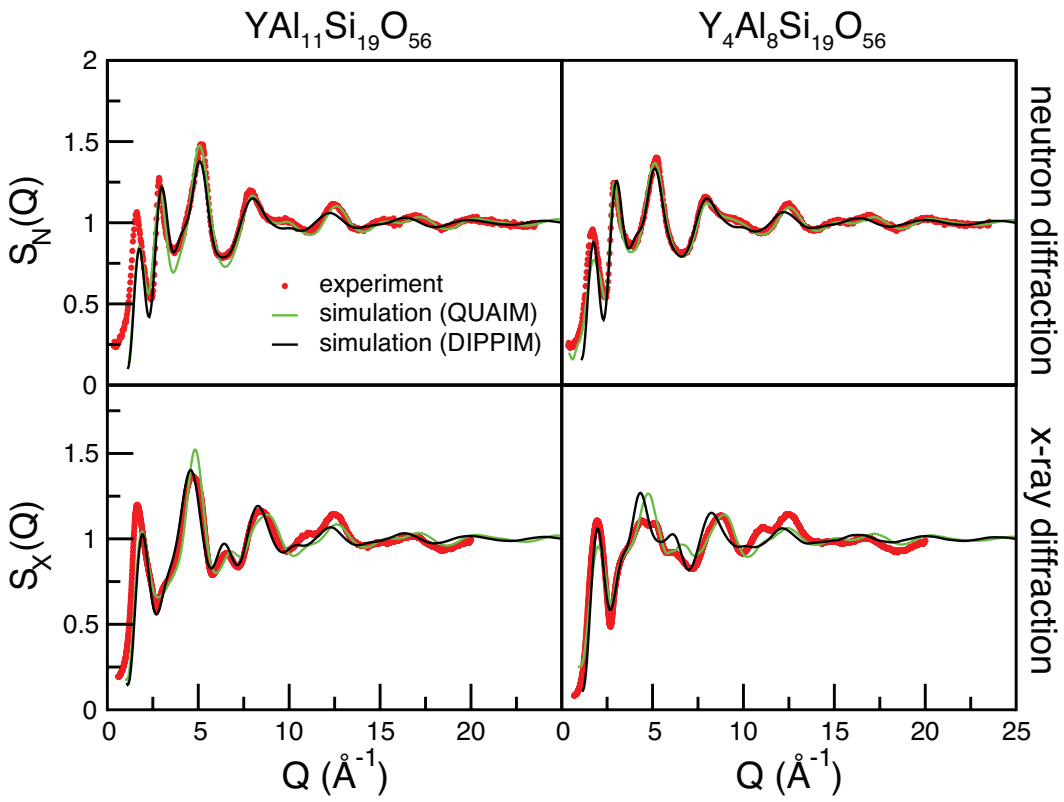

Figure 3.5: Neutron (upper panel) and x-ray (lower panel) structure factors $S(Q)$ of $YAl_{11}Si_{19}O_{56}$ (left) and $Y_4Al_8Si_{19}O_{56}$ (right) glass. Red circles: experiment, black and green lines: MD simulation.

3.4.4 Classical MD of glasses

We turn now to the simulated glass structures obtained from multiple quenches of melt structures to 300 K. In order to compare simulation results to experiments, it is necessary to convert the structural information contained in the classical MD trajectories to experimentally observable quantities, i.e. to neutron and x-ray (static) structure factors $S_N(Q)$ and $S_X(Q)$, respectively. These can be written as a weighted sum of Faber-Ziman partial structure factors $S_{\alpha\beta}(Q)$, each corresponding to a pair of elements $\alpha, \beta \in \{$REE, Al, Si,

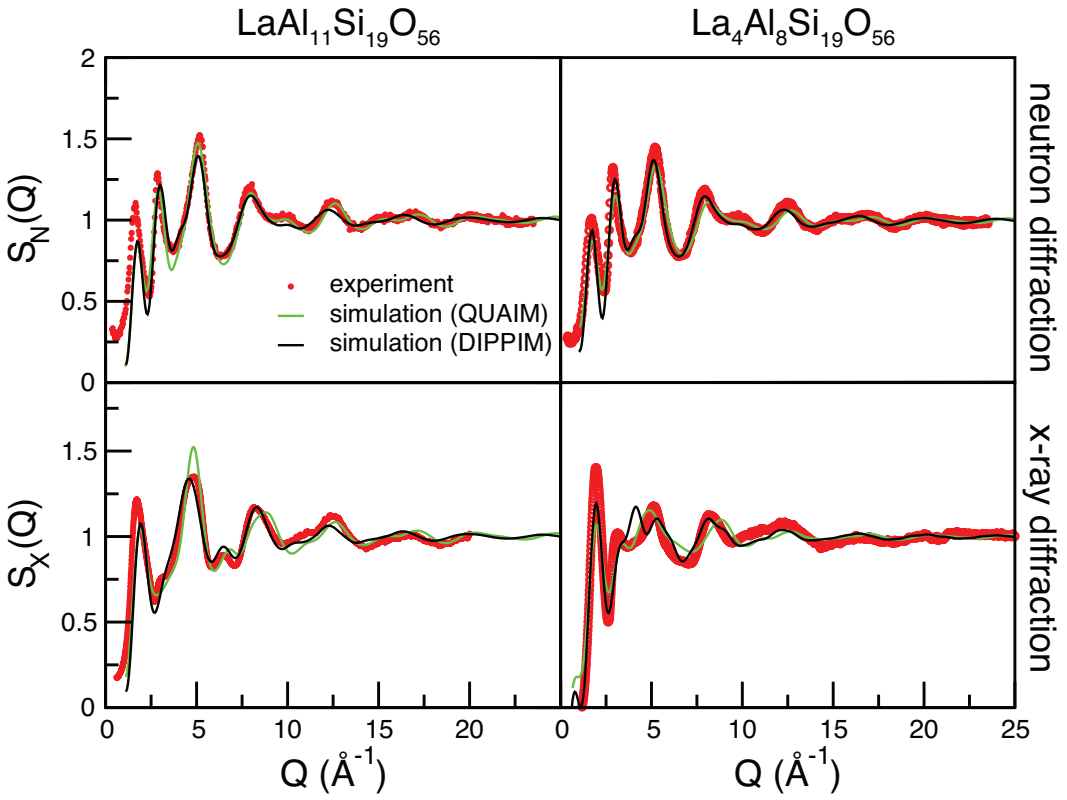

Figure 3.6: Neutron (upper panel) and x-ray (lower panel) structure factors $S(Q)$ of $LaAl_{11}Si_{19}O_{56}$ (left) and $La_4Al_8Si_{19}O_{56}$ (right) glass. Red circles: experiment, black and green lines: MD simulation.

O} (Faber and Ziman, 1965):

$$S(Q) - 1 = \frac{1}{\left(\sum_\alpha c_\alpha b_\alpha\right)^2} \sum_{\alpha,\beta} c_\alpha c_\beta \, b_\alpha(Q) b_\beta(Q) (S_{\alpha\beta}(Q) - 1) \tag{3.2}$$

where Q is the magnitude of the scattering vector $\boldsymbol{Q}$, c_α denotes the concentration of element α and b_α its neutron or x-ray scattering length. The latter is Q-dependent. Scattering lengths are tabulated in Sears (1992) and Ibers and Hamilton (1974). The partial structure factors are the Fourier transforms of the partial radial distribution functions $g_{\alpha\beta}(r)$, which in turn are obtained from the MD simulations:

$$S_{\alpha\beta}(\boldsymbol{Q}) - 1 = n_0 \int d\boldsymbol{r} \; (g_{\alpha\beta}(\boldsymbol{r}) - 1) \exp(-i\boldsymbol{Q} \cdot \boldsymbol{r}) \tag{3.3}$$

with the atomic number density n_0 of the glass. The partial radial distribution functions for all glass compositions, obtained from classical MD simulations, have been converted to neutron and x-ray structure factors by use of eq. 3.3 and eq. 3.2, and the structure factors are compared to the experimental ones in Figs. 3.5 and 3.6.

Conversely, x-ray or neutron weighted radial distribution functions *g(r)* can be calculated from the corresponding structure factors by inverse Fourier transformation given in eq. 3.4

$$g(r) - 1 = \frac{1}{2\pi^2 r n_0} \int Q[S(Q) - 1] \sin(Qr) dQ \tag{3.4}$$

Fig. 3.7 shows the weighted radial distribution functions for the composition $Y_4Al_8Si_{19}O_{56}$ derived from both experiment and classical MD simulation.

To conclude the results section, we give the parameters describing the first coordination shell around cations in the glasses for all four compositions in Table 3.4. Also listed are coordination numbers and bond lengths extracted from the neutron diffraction experiments by fitting Gaussian peaks to the Fourier-transformed structure factor (Leydier, 2010). This procedure yields coordination numbers for Si and Al to within 0.5 only. Coordination numbers of Y and La could not be obtained from the diffraction experiments because the first peaks in the respective partial radial distribution functions were superposed by others and could not be unambiguously resolved.

3.5 Discussion

3.5.1 Melt structures: Ab initio vs. classical MD

The quality of the structure models for the melts and glasses obtained from classical MD simulations is assessed by comparison to ab initio-derived melt

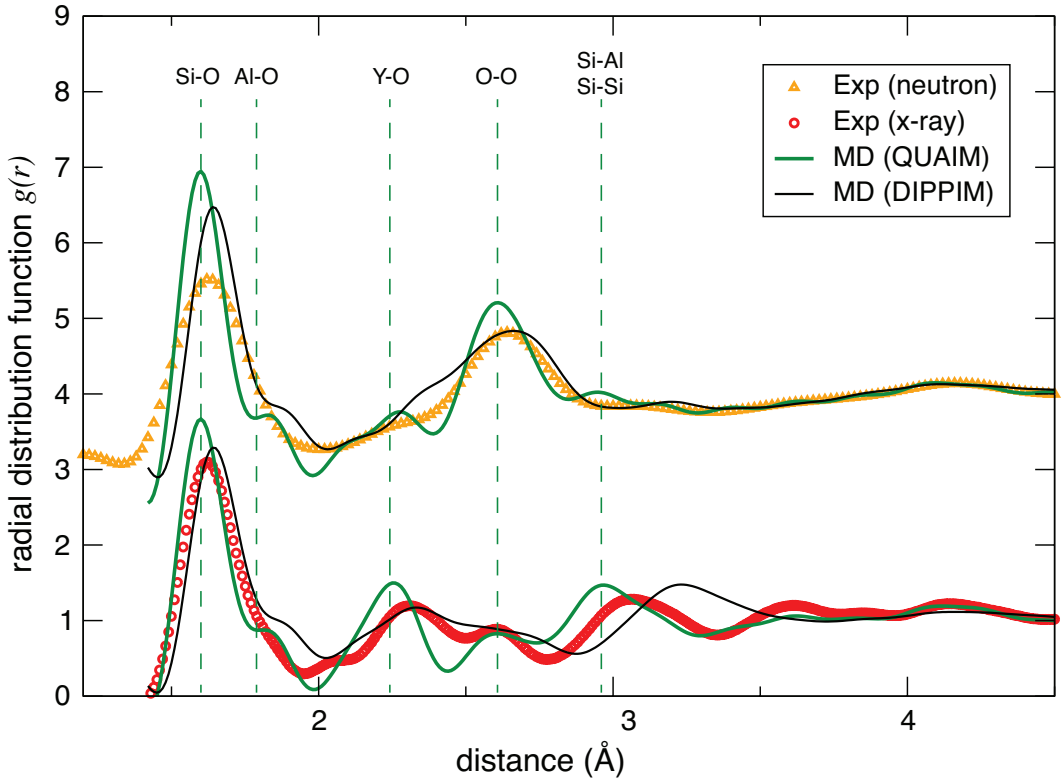

Figure 3.7: Calculated versus experimental total radial distribution function in $Y_4Al_8Si_{19}O_{56}$ glass. Orange triangles: experimental data (neutron scattering); red circles: experimental data (x-ray scattering), green lines: QUAIM, black lines: DIPPIM. Indicated are the peak positions of the partial ion pair contributions (for QUAIM only). Note how several DIPPIM peaks are shifted to higher distances while QUAIM shifts to lower distances compared to experimental findings. Neutron data are shifted by 3 along the y-axis for visibility. For a detailed discussion of regions >3Å see Fig.3.8

Table 3.4: Classical MD (^{di} for DIPPIM, ^{qu} for QUAIM) and neutron diffraction results for the first coordination shell around cations in glasses: cutoff radius r_{cut} for cation-oxygen pairs, average coordination numbers CN, experimental $\mathrm{CN}^{\mathrm{exp}}$, average bond length d, most probable bond length $\hat{d}$, peak of $rg_{\alpha\beta}(r)$ derived from experiments $\hat{d}^{\mathrm{exp}}$ and standard deviation σ of cation-oxygen bond lengths.

cation	$\mathrm{CN}^{di\|qu}$	$\mathrm{CN}^{\mathrm{exp}}$	$d^{di\|qu}$ (Å)	$\hat{d}^{di\|qu}$ (Å)	$\hat{d}^{\mathrm{exp}}$ (Å)	σ (Å)
			$YAl_{11}Si_{19}O_{56}$ glass			
Si	4.2 | 4.0	4.0(5)	1.68 | 1.60	1.64 | 1.61	1.62(3)	0.109
Al	5.2 | 4.2	4.3(5)	1.94 | 1.80	1.81 | 1.76	1.80(3)	0.210
Y	7.6 | 7.1(1)	-	2.51 | 2.31	2.35 | 2.28	2.30(3)	0.256
			$Y_4Al_8Si_{19}O_{56}$ glass			
Si	4.2 | 4.0	4.1(5)	1.67 | 1.60	1.64 | 1.60	1.62(3)	0.104
Al	5.0 | 4.1	4.1(5)	1.92 | 1.79	1.80 | 1.78	1.81(3)	0.219
Y	7.3 | 6.7(1)	-	2.50 | 2.29	2.33 | 2.25	2.32(3)	0.272
			$LaAl_{11}Si_{19}O_{56}$ glass			
Si	4.2 | 4.1	4.0(5)	1.67 | 1.65	1.63 | 1.61	1.62(3)	0.101
Al	5.1 | 4.4(1)	4.3(5)	1.93 | 1.90	1.81 | 1.80	1.81(3)	0.205
La	7.9 | 7.5(2)	-	2.65 | 2.60	2.46 | 2.40	2.51(3)	0.309
			$La_4Al_8Si_{19}O_{56}$ glass			
Si	4.1 | 4.0	4.2(5)	1.66 | 1.60	1.64 | 1.60	1.62(3)	0.095
Al	4.8 | 4.1	4.1(5)	1.89 | 1.78	1.79 | 1.78	1.82(3)	0.180
La	7.3 | 6.2(1)	-	2.62 | 2.37	2.42 | 2.44	2.51(3)	0.309

structures and to experimental diffraction data for the glasses. Figs. 3.1 and 3.2 demonstrate an overall reasonable agreement between classical and DFT simulations for the partial radial distribution functions in the four investigated melts. In the case of the DIPPIM potential, peaks corresponding to the first coordination shells of oxygen around Si and Al come out somewhat lower in the classical MD for all compositions, and they extend to a larger distance (more so for Al-O than for Si-O). For the $La_4Al_8Si_{19}O_{56}$ melt, the classically simulated La-O peak falls off faster on the large-distance side than the one obtained from the ab initio simulation. In the QUAIM case, peaks in the partial radial distribution functions are systematically higher and narrower, reflecting a slightly too strong cation-oxygen bonding. *These differences lead to some variation in the structural parameters describing the first coordination shells around cations, listed in Table 3.1 (ab initio) and Table 3.3 (classical): DIPPIM coordination numbers for Si are overestimated by the classical simulations*

by up to 0.2, and Al coordination numbers by up to 0.5. QUAIM on the other hand underestimates Si coordination numbers by up to 0.2 and Al up to 0.3. Both potential types underestimate La coordination in $La_4Al_8Si_{19}O_{56}$ melt by 0.9 with respect to the *ab initio* result. *On the other hand, average cation-oxygen bond lengths in melts agree well between all three simulation methods, the largest deviation being 0.08 Å for Al-O bonds in* $LaAl_{11}Si_{19}O_{56}$ *melt* (DIPPIM potential).
Note, moreover, that both classical and ab initio simulations yield the same trends for structural variations in response to compositional changes: REE and Al coordination numbers decrease with increasing REE content. For the DIPPIM case of Al, this decrease is even quantitatively the same as in ab initio results, while the effect is less pronounced for the QUAIM potential. Finally, we point out that the coordination numbers of REE predicted by the DIPPIM and *ab initio* methods are considerably larger than those reported in previous simulation studies (Du, 2009; Iftekhar et al, 2012; Okhotnikov et al, 2013). For example, Okhotnikov et al (2013) found Y coordination numbers below 6.6 and La coordination numbers of approximately 6.4, using a non-polarizable interatomic potential, but also different glass compositions. QUAIM predictions in this study tend to be somewhat lower than the *ab initio* MD data but still higher than the previous simulation studies.

3.5.2 Glass structures: Diffraction vs. classical MD

As another test of the classical interaction potentials, we compare neutron and x-ray structure factors derived from simulated glass structures to experimental data in Figs. 3.5 and 3.6. The simulated and the experimental neutron structure factors are found in good agreement in terms of peak positions, and in most cases also with regard to peak intensities (upper panels). The aspherical ion model (QUAIM) potential reproduces peak positions and intensities more accurately in most cases, especially in the higher Q regions (7 - 25 $Å^{-1}$). *The overall agreement of the x-ray structure factors (lower panels) is reasonable for the REE-poor compositions, but less satisfactory for* $Y_4Al_8Si_{19}O_{56}$ *(Fig. 3.5 right panels) and* $La_4Al_8Si_{19}O_{56}$ *(Fig. 3.6 right panels).* Here, both QUAIM and DIPPIM potentials show differences to experimental findings that require further inspection.
The discrepancy between experiment and simulation in glasses as well as the contribution of the utilized potential can be further elucidated by analyzing the weighted radial distribution functions derived directly from the corresponding structure factors. Figure 3.7 shows the calculated versus measured total radial distribution function of $Y_4Al_8Si_{19}O_{56}$ glass. For QUAIM, especially in the x-ray case, an underestimation of bond lengths becomes clear when comparing

peak positions of Y-O or Si-Al which are shifted to lower distances (green line, Fig. 3.7). DIPPIM on the other hand systematically overestimates bonds involving Al, as indicated by the shift of peaks to higher distances (black line, Fig. 3.7). This also leads to the observed overestimation of Al coordination number in DIPPIM simulations. These shifted peaks directly translate to differences in the calculated structure factors. *The reason why the discrepancy between simulation and experiment are more profound in the x-ray compared to the neutron experiments is that Y and La have a large x-ray scattering length $b(Q)$, due to their large number of electrons. Therefore, correlations involving Y and La make a larger contribution to the total x-ray structure factor while the neutron structure factor tends to represent the overall oxygen structure of a compositions and is less influenced by larger cations.*

Differences in glass structure predicted by QUAIM and DIPPIM are illustrated in Fig. 3.8, showing a detailed view of the region >3 Å of the x-ray weighted radial distribution functions (upper panel). When comparing the contributions of cation - cation pairs of the two potentials (lower panel) it appears that in the DIPPIM case, the first peaks of the Al-Y and Si-Y correlations are shifted compared to Si-Al and Si-Si (orange and maroon vs. violet and brown lines). In the total g(r) this leads to a peak at about 3.23 Angstrom, which is significantly larger than the peak at 3.1 Angstrom in the experimental $g(r)$. On the other hand, there are two distinct features to observe in the QUAIM case. First, the four main peaks (Si-Al, Si-Si, Si-Y, Al-Y) overlap more closely around 3 Å and second, Al-Y as well as Si-Y develop a second peak at about 3.5 Å. While QUAIM underestimates cation distances in the 3 Å region, these split peaks coincide well with the experimental double peak feature between 3.5 and 4.5 Å which is entirely absent in the DIPPIM case. The Y-Y contribution also shows this double peak feature only in the QUAIM case (blue lines). Visual inspection of the MD trajectories suggests that in the glass structure as predicted by QUAIM, Y-O polyhedra are mainly connected to Al-O octahedra via shared corners and edges. In the DIPPIM case, on the other hand, only edge sharing dominates the Y-O / Al-O polyhedral connection. Calculated Al-O-Y bond angle distributions also confirm these observations. In the QUAIM case, Al-O-Y bond angles peak at about 90° (edge sharing) and 125° (corner sharing), while in the DIPPIM case, there is only one peak around 100° (edge sharing). Similar distributions can be found for Y-O-Y bond angles, explaining the double peak feature observed in experiments. The La bearing glasses also behave similarly, however much less pronounced.

From the preceding discussion, we conclude that the classical interaction potentials yield melt and glass structures with the following caveats: the coordination numbers of Al seem too large by up to 0.5 in the DIPPIM case, and those of La

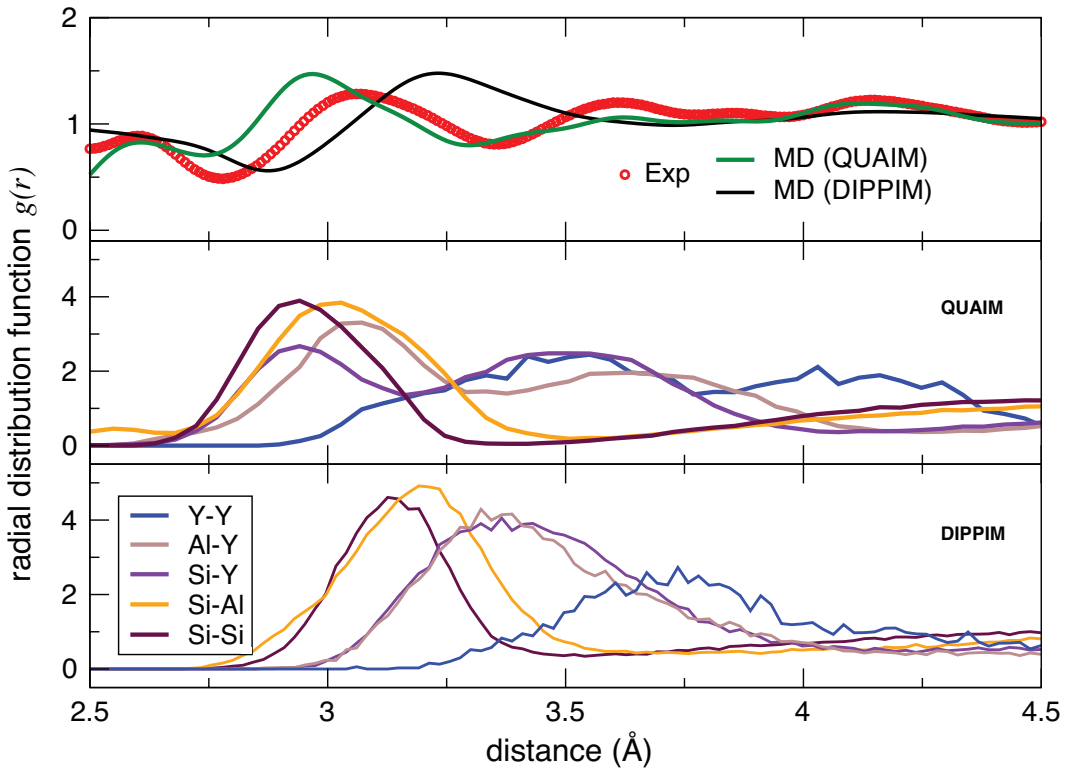

Figure 3.8: Detailed view of the partial (lower two panels) and total (upper panel) radial distribution functions of $Y_4Al_8Si_{19}O_{56}$ glass. Red circles: experimental data (x-ray scattering), solid lines: simulated data (QUAIM and DIPPIM). Note that in the QUAIM case, all contributions involving Y are split up into two peaks corresponding well to the double peak feature of the measured data. These features are entirely absent in the DIPPIM case.

seem to be on the low side for both potential types. MD derived coordination numbers of Y between 6-7 are in good agreement with coordination numbers that have been calculated directly from the experimental structure factors presented in this study. Simon et al (2013) also derive coordination numbers between 6-7 from EXFAS studies of Y bearing silicate melts. However, there are some substantial differences between QUAIM and DIPPIM potentials when comparing structural features beyond the nearest-neighbor range (correlations between network formers and REE cations and how they interconnect). Only the QUAIM potential seems to describe correctly the connectivity of Al-O and Y/La-O polyhedra. If the connectivity was only dominated by edge sharing polyhedra as described by the DIPPIM potential, the total $g(r)$ would look different.

3.5.3 Melt vs. glass and simulated quenching

We next discuss structural similarities and differences between melts and glasses of the same composition. *The Al coordination numbers found in the ab initio and classical MD simulations of REE-bearing aluminosilicate melts are significantly larger than the ones extracted from the diffraction experiments (Table 3.4) and from experiments using NMR or infrared spectroscopy on glasses of similar compositions (Schaller and Stebbins, 1998; Marchi et al, 2005; Florian et al, 2007; Iftekhar et al, 2011). In these studies, AlO_4 was always found to be the most abundant Al species by far, although noticeable amounts of 5- and 6-fold coordination were detected. This raises the question whether the simulation results are inaccurate or whether the discrepancies reflect real structural differences between melts at 3000 K and glasses at room temperature.*
The effect of temperature on structure has been investigated experimentally: Florian et al (2007) performed in-situ ^{27}Al NMR measurements on melt samples with compositions very similar to ours and found that fivefold coordinated Al is favored at high temperatures, without quantifying the extent to which this happens. An increase of the Al coordination number with temperature was even observed in nominally fully polymerized glasses, where AlO_4 could theoretically be fully charge-balanced by modifier cations: by extrapolation to high temperatures of NMR data obtained on $CaAl_2Si_2O_8$ glasses, quenched with varying rates and hence representing varying fictive temperatures, Stebbins et al (2008) predicted that at 2800 K, up to 39% of Al should be fivefold coordinated. In a temperature-dependent NMR study on calcium aluminate liquid, Massiot et al (1995) observed an increase of the average Al coordination number above the glass transition temperature by 0.2 per 1000 K. In a neutron diffraction study also on calcium aluminate, (Drewitt et al, 2012) report a significant decrease of Al coordination and other structural rearrangements upon vitrification. These

experimental findings lead us to the conclusion that the large Al coordination numbers found in our ab initio simulations of melts do not indicate a deficiency of the method but are due to the high temperature (3000 K) of the modeled systems. In the DIPPIM MD simulations of melts, the even higher Al coordination numbers are explained by the combined effect of high temperatures and the tendency of the interaction potential to over-coordinate Al (see section 3.5.1).

If the large Al coordination numbers in the simulated melts are explained by the high temperature, so why are they still so large in the simulated glasses (table 3.4)? The model glasses in this study have been generated by cooling from high-temperature melts (see section 3.2), with a quench rate of $5 \cdot 10^{13}$ *K/s. This exceeds experimental quench rates, which are typically below* 10^5 *K/s (see e.g. Stebbins et al, 2008), by many orders of magnitude. Since the fictive temperature, at which the melt structure is frozen into the glass, increases with increasing quench rate (Mysen and Richet, 2005, Chap. 1), the preceding argument for high Al coordination applies as well to rapidly quenched glasses. To assess the influence of the quench rate, we also generated a glass structure of composition* $YAl_{11}Si_{19}O_{56}$ *with a 10 times slower simulated quench. For DIPPIM and QUAIM, no significant changes in the structural parameters were observed with respect to the quickly cooled glass. However, this slower quench is still much faster than in experiments, and we suppose that lower rates are required to produce structural changes in the resulting glass.*

3.5.4 Relation between cation coordination and field strength

We suggest to rationalize the observed changes in cation coordination as a function of glass composition (classical MD simulations) in terms of cation field strength (CFS), which gives a simple measure of a cation's ability to force the surrounding oxygen anions into an energetically favorable configuration. It is defined as $CFS = q/r^2$*, with nominal ionic charge* q *and ionic radius* r*. The ionic radii were taken from Shannon (1976), assuming 4-fold coordinated Si, 5-fold coordinated Al and 7- or 8-fold coordinated Y and La, depending on composition (see table 3.4).*

The increasing variability of cation coordination as a function of glass composition, in the order Si, Al, Y, La, reflects their decreasing CFS. The fact that the Si coordination is virtually independent of composition can be explained by its large CFS: in the competition for oxygen bonding among the cations, the Si ions' preference for tetrahedral coordination is satisfied foremost, be it at the expense of more unfavorable coordination environments of the the other

cations. The distribution of oxygen between the coordination shells around Al and REE cations is determined by the "reaction"

$$\mathrm{AlO}_n + \mathrm{REEO}_m \rightleftharpoons \mathrm{AlO}_{n+1} + \mathrm{REEO}_{m-1} \tag{3.5}$$

between coordination polyhedra in the glass. Y has a larger field strength than La and therefore requires a more compact coordination shell with less but shorter and stronger bonds to surrounding oxygen atoms. Thus, the equilibrium in Eq. 3.5 is shifted more to the right for the Y-bearing glasses, as compared to the La-bearing compositions, which explains the higher Al coordination numbers in the former. This trend in Al coordination number has also been observed in a number of experimental studies (Schaller and Stebbins, 1998; Marchi et al, 2005; Florian et al, 2007; Iftekhar et al, 2011).
Also the changes in Al coordination as a function of REE content (for a given REE) can be rationalized in terms of field strength effects: in the REE-rich compositions, the environment of Al is richer in lower-field-strength Y or La and contains less higher-field-strength Si and Al than in the REE-poor glasses, so that Al readily forms a tighter coordination shell in the REE-rich glasses. Furthermore, the low-REE glasses are peraluminous, $[Al_2O_3]/[REE_2O_3] > 3$, and full charge compensation for fourfold coordinated Al is not possible. This also forces Al into higher coordination in these glasses. The same dependence of Al coordination numbers on REE content is also confirmed experimentally by Schaller and Stebbins (1998) and Florian et al (2007). The latter investigated glass compositions very similar to ours, and they found that the average Al coordination number drops from 4.3 in the Y-poor to 4.1 in the Y-rich glass, which is the same change by 0.2 as found with classical MD simulations. The decreasing REE coordination with increasing REE content can be explained in the same way. It is consistent with the findings in Haigis et al (2013), where the Y coordination number in Ca-bearing aluminosilicate melts was shown to decrease with increasing Ca content, since Ca shows a lower cation field strength than Si and Al.
Not only the coordination numbers of cations can be linked to the field strength, but also the width of the coordination shell formed by oxygen around the cations. Whereas high field strength cations are expected to form a tight coordination shell with well defined bond lengths, less powerful cations are anticipated to be forced into more disordered environments with a wider range of nearest-neighbor distances. This behaviour is confirmed by the simulation results shown in Fig. 3.9, where the standard deviation of cation-oxygen bond lengths (a measure for the width of the coordination shell) is plotted against the inverse cation field strength. For all four compositions, a (non-linear) correlation is clearly visible. Moreover, the oxygen shell around Si and Al in the La-bearing glasses

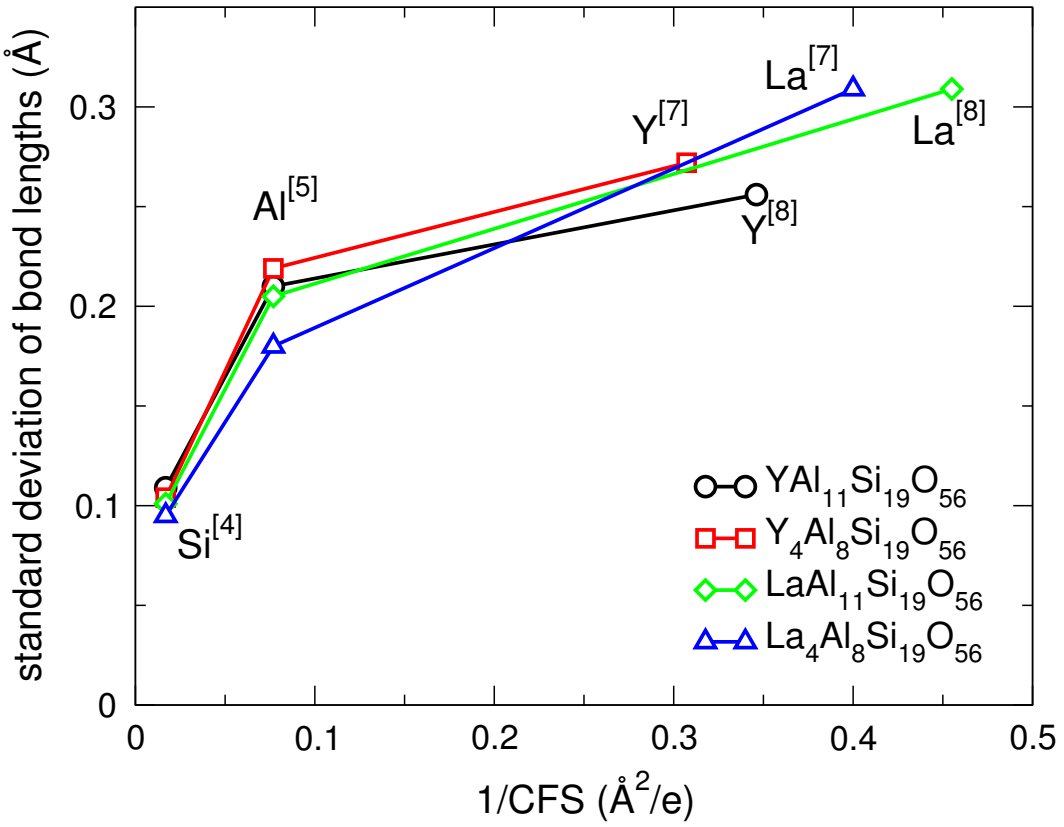

Figure 3.9: *Classical MD on glasses: width of the oxygen coordination shell around cations, given as the standard deviation of the distribution of cation-oxygen bond lengths, as a function of inverse cation field strength. The coordination numbers used for the calculation of the field srength are indicated as superscripts. Lines are a guide to the eye.* Figure from Haigis (2013).

is found to be narrower, i.e. less perturbed, than in the Y-based compositions. This further corroborates the interpretation of coordination environments in terms of a competition for oxygen bonding between cations of different field strengths.

Coordination shells of cations and their evolution upon compositional changes have been discussed here in terms of the glass structures obtained from classical MD simulations, but the same trends are also observed in the ab initio MD simulations of melts (Table 3.1). Therefore, the results appear to be robust with respect to the simulation method and seem to hold for both melts and glasses.

3.5.5 Medium-range order: Al/Si ordering

To conclude this section, the distribution of bridging oxygen among the various pairs of tetrahedral species is discussed. Iftekhar et al (2009) investigated this distribution by means of ^{29}Si NMR experiments on La-bearing aluminosilicate glasses, which were, however, considerably richer in La than our compositions. Their results are based on fitting several distribution models to the data and suggest a nearly random distribution of BO between tetrahedrally coordinated Si and Al. But given the uncertainty of their assumptions and structural models, they caution against over-interpreting this conclusion. Our ab initio MD simulations of aluminosilicate melts containing Y and La are a unique opportunity to complement the experimental data and to address this question quantitatively and without further assumptions.

In aluminosilicate minerals, the distribution of tetrahedrally coordinated Si and Al in the crystal structure is subject to the Al avoidance or Loewenstein rule which states that due to their excess negative charge, pairs of Al tetrahedra linked by BO are strongly unfavored, and instead alternation of Si and Al tetrahedra occurs in the crystal structure (Loewenstein, 1954). Since silicate melts and glasses are composed of the same tetrahedral building blocks, it may be conjectured that they also obey this ordering principle. We tested if the rule applies to the amorphous phases studied here by checking the distribution of bridging oxygen, T-O-T, among the motifs Si-O-Si, Si-O-Al and Al-O-Al. It is instructive to compare the BO distribution actually found in the melt to the random distribution, which would be expected simply on the basis of the abundances of tetrahedral Si and Al, in the absence of any ordering rule. This random distribution is found as follows: if there are N_T tetrahedrally coordidated species of type T and $N_{T'}$ of type T' ($T, T' \in \{\mathrm{Si}, \mathrm{Al}\}$) in the simulation cell, then the number $p_{T,T'}$ of possible pairs of tetrahedra T, T' linked

by bridiging oxygen is

$$p_{T,T'} = \frac{1}{2} N_T (N_{T'} - \delta_{TT'}) \tag{3.6}$$

where $\delta_{TT'}$ is 1 for $T = T'$, i.e. for like pairs (Si-O-Si or Al-O-Al), and 0 otherwise. The factor 1/2 corrects for double counting of pairs, and the number of unlike pairs (Si-O-Al) is understood to be the sum $p_{\mathrm{Si,Al}} + p_{\mathrm{Al,Si}} = 2p_{\mathrm{Si,Al}} = N_{\mathrm{Si}} N_{\mathrm{Al}}$. For a random distribution, the fraction of BO linking T and T' would then be

$$x_{\mathrm{BO}}^{\mathrm{rand}}(T - O - T') = \frac{(2 - \delta_{TT'}) p_{T,T'}}{\sum_{T,T'} p_{T,T'}} \tag{3.7}$$

The results concerning the BO statistics are given in table 3.2.
In all four compositions studied here, the molar ratio [Al]/[Si] is considerably less than 1, so that strict avoidance of Al-centered tetrahedra linked by BO could formally be achieved (Loewenstein, 1954). However, the results presented in table 3.2 indicate that in all compositions except for the La-rich melt, the BO partitioning between Si and Al is close to random. Only in $La_4Al_8Si_{19}O_{56}$, the $Al^{[4]}$-BO-$Al^{[4]}$ motif is less frequent than expected for a random distribution, in favor of an elevated amount of $Si^{[4]}$-BO-$Al^{[4]}$, but still a significant degree of randomness is observed. A priori, this structural disorder in simulated REE-bearing aluminosilicates may be an effect of the high temperature, which favors configurations of higher entropy. Recently, Jaworski et al (2012) and Okhotnikov et al (2013) reported an essentially random Al/Si distribution in La-bearing aluminosilicate glasses which were considerably richer in La than the compositions studied here. They performed classical MD simulations with a simple pair potential. From our ab initio simulations in conjunction with the experimental data of Iftekhar et al (2009) and the results of Jaworski et al (2012) and Okhotnikov et al (2013), we conclude that the Al avoidance rule is not obeyed in the melts studied here and that it probably does not (or at least not strictly) apply to the glasses either.
This may be attributed to the greater structural flexibility of amorphous structures as compared to crystalline phases, which allows excess charges on BO between Al-centered tetrahedra to be compensated more easily. On the other hand, in aluminosilicate glasses containing divalent network modifiers, Al avoidance was found to be realized to a large extent, although not strictly (Lee and Stebbins, 2006). This indicates that also the higher charge and field strength of trivalent Y and La have a share in the Al/Si disorder found in our study, by facilitating charge compensation of otherwise unfavorable structural motifs. This suggests that the traditional picture of glasses, derived from alkali- and alkaline earth-bearing aluminosilicates, should be used carefully when applied to

REE-bearing glasses, since trivalent elements may behave differently in terms of network modification and charge balancing.

3.6 Conclusions

The atomic-scale structure of four Y- and La-bearing aluminosilicate glasses and melts with high SiO_2 content (76 mol%) was investigated by ab initio and classical MD simulations as well as neutron and x-ray diffraction experiments. By combining information from all four approaches, we described the coordination environments of the cations and found robust evidence for structural trends as a function of composition: coordination numbers of REE cations decrease with increasing REE content, and so do Al coordination numbers. Moreover, Al was found to be in a higher coordination state in Y-rich than in La-rich composition. These trends can consistently be explained by the various cation field strengths: they impose a hierarchy on the melts and glasses as to which cation's coordination requirements are satisfied preferentially, at the expense of the others' bonding requirements. Furthermore, the Al avoidance rule obeyed in aluminosilicate minerals was found to be almost completely invalidated in REE-bearing aluminosilicate melts.
Ab initio and DIPPIM simulations consistently yield a coordination number of Y in REE-bearing aluminosilicate melts and rapidly quenched glasses between 7 and 8, depending on composition.This is larger than the values found for the QUAIM case (around 7) and in other classical MD studies on glasses, which lie below 7 (Du, 2009) or even below 6 (Iftekhar et al, 2012). La coordination numbers in aluminosilicate melts containing REE were determined by means of *ab initio* simulations, yielding values close to 8. The new classical interaction potentials for La have shown to produce reasonable melt and glass structures but to form a slightly too tight coordination shell around La, especially in La-rich compositions, which leads to underestimated coordination numbers especially in the QUAIM case, similar to results for REE bearing melts of Okhotnikov et al (2013). Furthermore, we find that some features of the experimental structure factors can potentially be explained by a mixture of corner and edge sharing Al-O/Y-O polyhedra with a predominance of edge sharing. The two classical potentials diverge in their prediction of this feature, the QUAIM potential being much closer to experimental observations.
Calculated structure factors, especially neutron scattering factors agree well with experimental findings, emphasizing that regardless of uncertainties in a particular coordination environment, the overall structure of melts and glasses is predicted rather well. Three major effects may cause the shortcomings in x-ray structure factors: 1) effects (over- or underestimation) of the utilized

potential on nearest and next-nearest neighbour environments, 2) alteration of peaks due to the Fourier transformations effects when calculating structure factors and 3) effects of fast quench rates (too little time to rearrange cations, prevention of clustering of REE in glasses etc). At least the latter could be ruled out by directly comparing experimental and simulated structure factors for melts. For future classical MD studies, an improved description of La might be achieved by using more training structures (La-bearing crystals and more glasses) for the parametrisation of the classical potential. Most shortcomings of the classical approach seem to be emphasized when REE content is increased. The overall accurate description of the REE behaviour in melts and the fact that both elements usually occur as trace elements in geologically relevant systems encourages future use of the presented potentials (e.g. to calculate trace element distributions or the structure of REE in natural melts).

Chapter 4

Trace element partitioning between silicate melts

This chapter is based on a manuscript submitted as:
Wagner, J., Künzel, D., Haigis, V., Jahn, S.
Trace element partitioning between silicate melts - a molecular dynamics approach
Contributions to Mineralogy and Petrology

Individual Contributions:
J. Wagner planned and performed research, performed classical and first-principles simulations, analysed the data, wrote the paper.
D. Künzel and V. Haigis were involved in planing the research, participated in writing the paper.
S. Jahn planned and supervised the research, participated in writing the paper.

4.1 Introduction

The use of trace elements as tracers of magmatic processes in the Earth's interior is a standard tool on the geochemist's workbench and as such, these elements have received much attention throughout the last decades (Goldschmidt, 1937; Ringwood, 1966; Blundy and Wood, 2003; Shaw, 2006). The distribution of an element between phases involved in a geochemical reaction is conventionally quantified with the partition coefficient D. D is defined as the concentration ratio of element X between two phases α and β (e.g. a mineral and a melt) (Beattie et al, 1993):

$$D_X^{\alpha/\beta} = \frac{[X_\alpha]}{[X_\beta]} \tag{4.1}$$

Knowledge of these partition coefficients is essential for quantitative modelling of mineral-melt reactions and the corresponding experimental studies are numerous (e.g. Green, 1994; Stalder et al, 1998; Klein et al, 2000; Corgne and Wood, 2002; Pertermann et al, 2004; Sun and Liang, 2011; Beyer et al, 2013). D values are not constants but may strongly depend on pressure, temperature and compositions of both mineral and melt. The most widely used model to predict mineral-melt partition coefficients is based on the lattice strain theory (Blundy and Wood, 1994). The model predicts partition coefficients by evaluating the mismatch in atomic radius and charge when a trace element is substituted for a major element in a regular crystal lattice. It has been applied and adjusted successfully in many studies (Wood and Blundy, 1997; van Westrenen et al, 2001; van Westrenen and Draper, 2007; Sun and Liang, 2011; Corgne et al, 2012; Sun and Liang, 2013; Davis et al, 2013).
By definition, the lattice strain model is focused on crystal structure and treats a potential influence of the corresponding melt indirectly. There is some debate about what control melt structure exerts on partitioning and many recent studies address this issue with conclusions varying from insignificant influence to several orders of magnitude difference in D values (Kohn and Schofield, 1994; O'Neill and Eggins, 2002; Mysen, 2004; Prowatke and Klemme, 2005; Schmidt et al, 2006; Huang et al, 2006; Evans et al, 2008; Girnis et al, 2013). Results of such studies are even harder to interpret as, in contrast to crystals, the structure of most melts and the local environment of trace elements therein is usually not well constrained. One way to circumvent this issue is to investigate element partitioning using computer simulations. Molecular simulations in particular offer a unique insight into structural properties of melts and crystals alike, while simultaneously provide access to many of their physicochemical and thermodynamic properties. Up till now most simulation studies have investigated element partitioning by statically calculating defect- and so-

lution energies in crystals and relating these properties to lattice strain theory (Purton et al, 1997, 2000; van Westrenen et al, 2000; Allan et al, 2003). On the other hand, studies explicitly focusing on melt properties are rare. Haigis et al (2013) explored an approach based on classical molecular dynamics (MD) to directly calculate trace element partitioning between a melt pair in the CaO-Al_2O_3-SiO_2 system. The authors used a thermodynamic integration method (Frenkel and Smit, 2002) to obtain the free energy difference of an element exchange reaction between the two melts, which directly relates to partitioning. In this contribution we aim to further investigate the potential of this method by calculating trace element partition coefficients for several experimentally well known systems. The goals of this study are (a) to predict partition coefficients from first-principles and classical model systems where experimental data are available and (b) to elucidate the effect of melt structure on the predicted partitioning behaviour. The first goal also serves as a benchmark of this method's capability to explore systems where experimental data may be lacking. We use molecular dynamics simulations in conjunction with thermodynamic integration (Marx and Hutter, 2012) to simulate partitioning of minor elements between several silicate melts. We explicitly focus on the effect of melt composition because the element exchange with a crystal usually involves coupled substitutions. Taking these into account would further complicate the thermodynamic integration approach we aim to test and needs to be discussed in future simulations involving this method. Therefore, our model systems are a gabbroic and granitic melt, similar in composition to coexisting melts investigated by Schmidt et al (2006), as well as a Ti bearing silicate melt pair, resembling melts studied by Prowatke and Klemme (2005). Note that we by no means suggest that the two Ti-bearing melts are coexisting in nature. We rather evaluate the effect of melt composition on mineral-melt partitioning by assuming a virtually unchanged crystal as opposed to a changing corresponding melt (see original experimental study, Prowatke and Klemme, 2005, for details). We chose to investigate the trace elements Y, La and As for two reasons. Firstly, experimental data for these elements are readily available for the investigate melt systems and secondly, all three elements have the same formal charge ($^{3+}$) but varying ionic radii (Y 1.04 Å, La 1.17 Å, As 0.58 Å, Shannon, 1976), making it possible to use the same substitution for Al^{3+} during thermodynamic integration (see below). The atomic interactions are either described by first-principles methods or classical force fields to compare their suitability for the thermodynamic integration approach. Also, the first-principles simulations may be used as reference points for end members of classical integrations (see Section 4.2.2).

First-principles MD is based on quantum mechanics, usually in the form of

density functional theory (DFT, Hohenberg and Kohn, 1964; Kohn and Sham, 1965) and provides an essentially parameter-free description of the total energy of any given set of atoms. In many cases it has been shown to be highly accurate and predictive, also in investigating the structure and properties of melts over a range of pressures and temperatures (Alfè et al, 2002; de Koker et al, 2013; Muñoz Ramo and Stixrude, 2014). However, first-principles methods are limited by their comparatively high computational cost, typically up to about a hundred atoms for MD simulations of complex silicate melts. Classical simulations, on the other hand, rely on force fields to describe atomic interactions. This makes the simulation of significantly larger systems and longer simulation times computationally affordable and thus enables the study of processes such as diffusion or the structure of melts and fluids beyond nearest neighbour distances. However, classical force fields can only be as accurate as the training set used for its parametrisation. Here, we use an advanced ionic interaction potential that has been successfully applied to simulate oxides and silicate crystals, melts and glasses (e.g. Jahn and Madden, 2007; Adjaoud et al, 2011; Finkelstein et al, 2014).

4.2 Simulation Procedure

4.2.1 Molecular dynamics simulations and compositions

We performed both first-principles and classical MD simulations of four silicate melts at room pressure. The composition of the first melt pair was inspired by experiments of Schmidt et al (2006) and resembles a granite and a gabbroic melt. The second melt pair are two Ti-bearing silicate melt (asi200 and asi280), resembling melts of titanite-melt partitioning experiments by Prowatke and Klemme (2005). The two melts vary mainly in their Al and Na contents. The simulation cells contained between 100 and 107 atoms. For the classical MD simulations we also used 2x2x2 supercells with 824 and 856 atoms to test for finite size effects. An overview over compositions and densities of all investigated systems is given in Table 4.1. All first-principles simulations are Born-Oppenheimer-type simulations, performed using the QUICKSTEP module (VandeVondele et al, 2005) of the CP2K software package (Hutter et al, 2014). We used the Perdew-Burke-Ernzerhof exchange correlation functional (Perdew et al, 1996) and Goedecker-Teter-Hutter (Goedecker et al, 1996) norm-conserving pseudopotentials. As basis sets we employed double-zeta valence plus polarisation basis sets (VandeVondele and Hutter, 2007). A planewave cutoff of 160 Ry was chosen as a compromise between accuracy and efficiency. For classical simulations, we used the FIST module of CP2K with an imple-

mentation of the utilised interaction potential by the authors. The classical interaction potentials were initially parametrised for the CaO-MgO-Al_2O_3-SiO_2 system by reference to first-principles electronic structure calculations (Jahn and Madden, 2007). In addition to charge-charge (Coulomb) interactions and dispersion, this model includes true many-body effects by accounting for polarisation effects (electronic multipoles up to quadrupoles) as well as aspherical shape deformation of anions, depending on their local environment (Madden et al, 2006). Multipoles and shape deformations are computed self-consistently at each simulation step. For this study, we extended the original set with interaction potentials for Y, La and Na (see Sec. 2.3, Tab. 2.1). Details about the parametrisation procedure can be found in the appendix.
As a precursor for production runs, we equilibrated two versions of each composition: one free of trace elements and one containing one or two atoms of Y, La, or As. Those serve as end-member reference for the thermodynamic integration (see below). These initial configurations were derived by generating random atom positions, taking into account typical, minimal bond distances. Densities were derived for 0 GPa and 3000 K from classical constant pressure (P) and temperature (T) simulations with equilibration times of at least 20 ps (NPT ensemble, N: constant number of particles). P and T are controlled by canonical sampling through rescaling (CSVR, Bussi et al, 2007) thermostat and barostat. Densities where subsequently fixed for the reference configurations. These cells have been further equilibrated at constant volume (V) for at least 20 ps (NVT ensemble) and subsequently used as basis for the thermodynamic integration. All simulations are performed with 1 fs time steps. Periodic boundary conditions are applied at all times.

4.2.2 Thermodynamic integration

Thermodynamic integration is a means to extract free energies from MD simulations (Frenkel and Smit, 2002). The change in free energy of a reaction is obtained by integrating changes in total energy over a reaction path. In an MD simulation framework, one possible reaction path is an alchemical transmutation in which the identity of an atom is gradually changed (e.g. Al is transmuted into Y). In this study, an exemplary reaction would be the exchange of Al and Y between a gabbro and granite melt:

$$Y^{3+}_{gabbro} + Al^{3+}_{granite} \rightleftharpoons Al^{3+}_{gabbro} + Y^{3+}_{granite} \tag{4.2}$$

This reaction is split into two separate sub-reactions, each comprising one alchemical transmutation:

$$\begin{aligned} Y^{3+}_{gabbro} &\rightleftharpoons Al^{3+}_{gabbro} \\ Y^{3+}_{granite} &\rightleftharpoons Al^{3+}_{granite} \end{aligned} \tag{4.3}$$

Table 4.1: Composition of all investigated systems (*sim*) and their experimental reference (*ref*). All compositional data are given atoms per eight oxygens. N and N^{super} are the total number atoms per simulation cell. The density ρ (g/cm^3) is given at 3000 K, derived from classical MD simulations. The line NBO/T lists the degree of depolymerisation calculated from reference compositions and simulations. The explicit chemical formulas for all simulated systems is given in the appendix.

	granitic		gabbroic		asi200		asi280	
	sim	*ref*[1]	*sim*	*ref*[1]	*sim*	*ref*[2]	*sim*	*ref*[2]
N	103	-	107	-	104	-	100	-
N^{super}	824	-	856	-	-	-	-	-
Si*	3.25	3.320	2.29	2.236	2.45	2.46	2.32	2.27
Al(+Fe)*	0.5	0.433	0.38	0.254	0.26	0.23	0.77	0.84
(Mg+Ca)*	0.375	0.442	2.79	2.594	0.77	0.79	0.65	0.71
(Na+K)*	0.75	0.435	0.13	0.128	1.29	1.21	0.52	0.43
Ti*	-	-	-	-	0.65	0.67	0.65	0.64
NBO/T	0.27	0.252	2.0	2.25	0.77	0.76	0.28	0.27
ρ_{3000K}	2.26	-	2.43	-	2.22	-	2.30	-

*per 8 oxygens; [1]Schmidt et al (2006); [2]Prowatke and Klemme (2005)

The progress along the reaction path for each transmutation is measured by a transmutation parameter λ, taking values from 0 to 1. The transmuted element is 100% Y^{3+} for λ equals 0 and 100% Al^{3+} once λ equals 1. During each step of the transmutation, forces f and energies V are computed for each end-member configuration (one containing Y^{3+}, one Al^{3+}). The resulting force f_{mix} during a transmutation is calculated as a linear combination of the two end-members as:

$$f_{mix} = (1 - \lambda) f_Y + \lambda f_{Al} \tag{4.4}$$

The final change in Helmholtz free energy ΔF for one of the transmutations in Eq. 4.3 is given by the integral over the average energy difference between the two end-members:

$$\Delta F = \int_0^1 \left\langle \frac{\partial V_\lambda}{\partial \lambda} \right\rangle_\lambda d\lambda = \int_0^1 \langle V_{Al} - V_Y \rangle_\lambda d\lambda \tag{4.5}$$

$V_{Al} - V_Y$ is evaluated at each MD step, the angular brackets indicate the average over time. In this study, we used three intermediate values for λ (0.25, 0.5, 0.75) in addition to the end-members. The total change in free energy ΔG^{exc} of Eq. 4.2 is then obtained as:

$$\Delta G^{exc} = \Delta F_{gabbro}^{Y \to Al} - \Delta F_{granite}^{Y \to Al} \tag{4.6}$$

assuming that $\Delta G \approx \Delta F$ for $P = 1$ bar.
In order to ensure path independence, every transmutation is conducted forwards and backwards, using the output configuration of the forward reaction as input for the back-reaction. Production runs of these thermodynamic integrations were performed at constant volume and temperature (NVT) at 2500 K (classical) and 3000 K (first-principles), also using a CSVR thermostat. Each integration step was run for at least 100 ps in the classical- and at least 20 ps in the first-principles based simulations. Because of the computational demand, simulation times are much shorter in the first-principles case. Aiming to compensate for this and achieve equilibrium more quickly in each transmutation step, the integration temperature is higher in the first-principles simulation.

4.2.3 Structural analysis

To gain further insight into structural controls of the partitioning behaviour we analyse the radial distribution functions (RDF) for each individual system and integration step. RDFs represent the likelihood to find a specific pair of atoms at a distance r, normalised to the mean atomic number density. For

individual atom types i and j the partial RDF is defined as:

$$g_{ij}(r) = \frac{1}{c_i c_j \rho_0 N} \left\langle \sum_{a=1}^{N_i} \sum_{b=1}^{N_j} \delta(\mathbf{r} - (\mathbf{r}_a - \mathbf{r}_b)) \right\rangle \tag{4.7}$$

In Eq. 4.7, N is the total number of atoms, ρ_0 the atomic number density, c_i is the concentration and N_i number of atom type i. $\mathbf{r}_a$ and $\mathbf{r}_b$ are atomic position vectors of atoms a and b, $\mathbf{r}$ is a distance vector with length r. δ is the Kronecker delta. Peak positions in $g_{ij}(r)$ represent the most probable bond distance in the corresponding coordination shell. From Eq. 4.7 we may derive the average coordination of atom type i by j by integrating $g_{ij}(r)$ to its first minimum. Comparing RDFs derived from first-principles and classical simulations also gives us a tendency of the accuracy of the structure predicted by our classical potentials.
To describe medium range order in melts, it is common practice to analyse the interplay of network formers such as Si, Al and Ti and network modifiers (larger cations such as Ca and Mg, Mysen, 2004). This is done by analysing the the interlinkage of oxygen atoms between those species. Oxygen atoms that link two 4-fold (tetrahedron) coordinated network formers (T) are considered to be bridging oxygen (BO). A terminal oxygen, bonded to only one network former is considered non-bridging (NBO). The ratio NBO/T acts as a measure of depolymerisation of the melt.

4.3 Results

4.3.1 Melt structure

We derive structural information from the MD trajectories of all investigated melts by calculating partial radial distribution functions (Eq. 4.7). The first-principles and classical MD results for granitic and gabbroic melt containing Y are given in Fig. 4.1. First-principles results for the Ti-bearing melts asi200 and asi280 are given in the appendix. From the partial RDFs, we also calculate the average coordination numbers and bond distance, which represent a mean through all occurring configurations of a specific element pair throughout the melt and over time (Tab. 4.2). TNote that, while peak positions agree well, peak maximum and shape of the partial RDFs predicted by classical simulations are systematically narrower and higher than corresponding first-principles simulations. This is because oxygen bonds are generally predicted to be slightly stronger than calculated by first-principles, which is a known caveat of the utilised potential type (e.g. Adjaoud et al, 2008). In

general, gabbroic and granitic melts show rather similar partial RDFs. The average oxygen-oxygen distances is shifted to higher distances and its distribution is broader (peak width) in the gabbro. Differences become clearer when looking at average coordination numbers. When comparing classical and first-principles simulations for these melts, the latter predict slightly higher average coordination numbers for all cations except Y, where both predict similar values. However, in both cases, the major elements Al, Ca and Na systematically show slightly higher average coordination numbers in the gabbro. The trace elements Y, La and As as well reach higher coordination numbers in gabbro (Y ∼7, La ∼6, As ∼4) as compared to granite. The Ti-bearing melts asi200 and asi280 on the other hand are very similar in their structure. There are only slight deviations in coordination numbers for both melts. Ti reaches coordination numbers of up to 4.5, Y and Ca are 6 fold coordinated. We also calculated the average NBO/T of all investigated melts (see Tab. 4.1).

4.3.2 Thermodynamic integration

For each of the four melts, we performed thermodynamic integrations by transmuting one Al atom into one of the three trace element atoms Y, La or As, with a total of five integration steps ($\lambda \in [0, 0.25, 0.5, 0.75, 1.0]$). As an example, Fig 4.2 shows the time averaged differences in total energy $< V_{Al} - V_Y >$ for different lambdas of the gabbro and the granite melts. Each curve represents one transmutation as described in Eq. 4.3 and integrating over a single curve yields the corresponding change in free energy of the transmutation reaction. The individual transmutation steps should plot on a monotonous curve between the end member configurations. Based on the energy fluctuations during MD simulations at constant lambda, we estimate the maximum statistical error of the individual energy differences to about 30 kJ/mol. The difference between the integrations for subreactions (i.e. the area between the two curves) gives the change in Gibbs free energy ΔG_{exc}. Integrating over a 4th order fit (see Fig. 4.2) of the data gives similar results as integrating over a linear extrapolation. From ΔG_{exc} the equilibrium constant K can be derived via

$$K_{exc} = exp(-\frac{\Delta G_{exc}}{RT}) \tag{4.8}$$

where T is the temperature and R the universal gas constant. The resulting equilibrium constants K_{exc} are given in Tab. 4.3 (third column). To illustrate the structural response to the thermodynamic integration within the melt, we also plot the partial RDF of the transmuted atom for each intermediate step in the inset in Fig. 4.2. Between the two end-members representing the ordinary partial RDF of Al and Y, there is a linear transition of the RDF (and

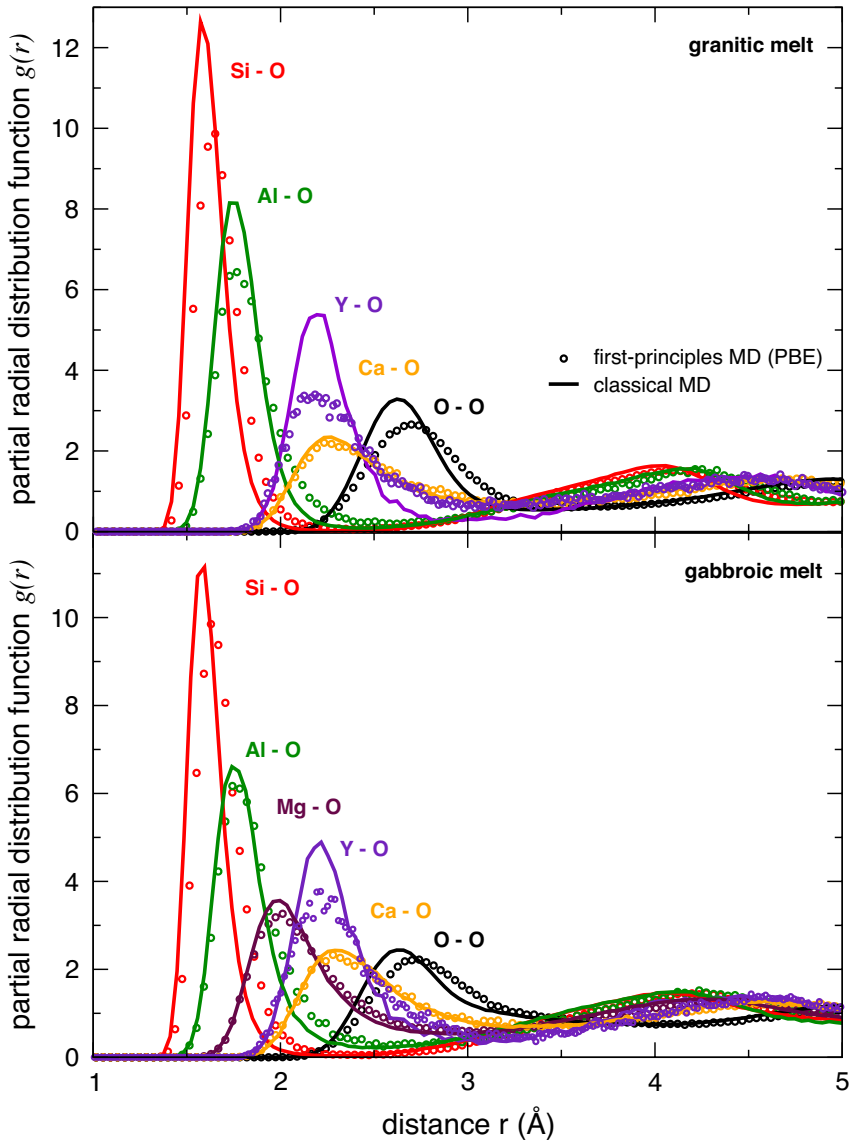

Figure 4.1: Partial radial distribution functions of the granitic (top) and gabbroic (bottom) melts doped with one Y each. First-principles results are shown as dotted lines, results from classical simulations as solid lines. Note that while peak positions agree rather well, the classical interaction potential systematically predicts higher and narrower peaks (i.e. on average tighter cation-oxygen bonds).

Table 4.2: Average oxygen coordination number CN, average bond length d and its standard deviation σ (width of the coordination shell) of major cations and trace elements in all investigated melts. Presented are classical (QUAIM) and first-principles (DFT) simulations

cation	CN	d (Å)	σ (Å)	CN	d (Å)	σ (Å)
	granitic (QUAIM)			gabbroic (QUAIM)		
Si	4.0	1.63	0.11	4.0	1.63	0.12
Al	4.0	1.81	0.14	4.3	1.85	0.17
Ca	5.6	2.59	0.36	7.0	2.60	0.34
Na	5.4	2.67	0.38	6.7	2.62	0.38
Mg				5.4	2.22	0.30
Y	5.9	2.31	0.24	6.9	2.36	0.25
La	5.1	2.31	0.28	6.4	2.48	0.30
	granitic (DFT)			gabbroic (DFT)		
Si	4.0	1.70	0.14	4.1	1.74	0.27
Al	4.1	1.90	0.16	4.5	1.99	0.31
Ca	6.0	2.64	0.38	7.6	2.61	0.45
Na	5.8	2.75	0.39	7.5	2.71	0.46
Mg				5.5	2.37	0.46
Y	5.6	2.42	0.39	6.8	2.45	0.40
As	3.4	1.99	0.26	3.8	2.09	0.38
	asi200 (DFT)			asi280 (DFT)		
Si	4.0	1.70	0.14	4.0	1.71	0.14
Al	4.1	1.88	0.20	4.1	1.88	0.20
Ti	4.5	1.97	0.25	4.5	1.98	0.25
Ca	6.2	2.64	0.39	6.2	2.67	0.39
Y	5.8	2.45	0.31	5.9	2.44	0.32

with it, coordination environment) via an intermediate, theoretical element. The results of the classical simulations for various starting configurations of gabbro and granite agree well, as they all predict equilibrium constants of ∼4 for 2500 K, no matter if one or two Y are transmuted. Also, there seems to be no finite size effect at least for these transmutations as similar results are obtained from large cells containing up to 856 atoms (denoted with ^{super} in Tab. 4.3). The transmutations based on first-principles however are less distinct. Two independent transmutations of Y in gabbro and granite both give equilibrium constants close to 1 for 3000 K. The arsenic transmutation gives a K_{exc} of ∼0.3. The exchange of Al and Y between the two Ti-bearing silicate melts results in an equilibrium constant of ∼3.5 for 3000 K, and thus suggest preferential partitioning of Y into the less polymerized melt (asi200, see discussion).

4.4 Discussion

4.4.1 Predicting trace element partitioning

The equilibrium constant of the exchange reaction K_{exc} relates to element concentrations in the involved phases by taking into account the activity coefficients γ (in the case of melts), giving

$$K_{exc} \cdot \frac{\gamma^{Al}_{gabbro}\gamma^{Y}_{granite}}{\gamma^{Y}_{gabbro}\gamma^{Al}_{granite}} = \frac{[Y_{gabbro}][Al_{granite}]}{[Al_{gabbro}][Y_{granite}]} \tag{4.9}$$

To our knowledge, there are no experimental data on the activity of the investigated trace elements in silicate melts. For the purpose of this study we assume that they are similar in both melts involved, and thus cancel out. Furthermore, we assume that the transmuted major element Al^{3+} does not partition significantly between the two, i.e. $D^{gabbro/granite}_{Al}$ is considered to be ∼1 (e.g. Veksler et al, 2006), leaving the right hand side of Eq. 4.9 reduced to the original definition of the partition coefficient D (Eq. 4.1) as

$$K_{exc} \approx D^{gabbro/granite}_{Y} = \frac{[Y_{gabbro}]}{[Y_{granite}]} \tag{4.10}$$

This means that we directly approximate the partition coefficient with the equilibrium constant K_{exc}. To compare our calculations to experimental results, we scale K_{exc} from the temperatures of the thermodynamic integrations to experimental temperatures, assuming ΔG does not vary significantly with temperature. The results are summarised in Table 4.3, column 5 (D_{est}), with

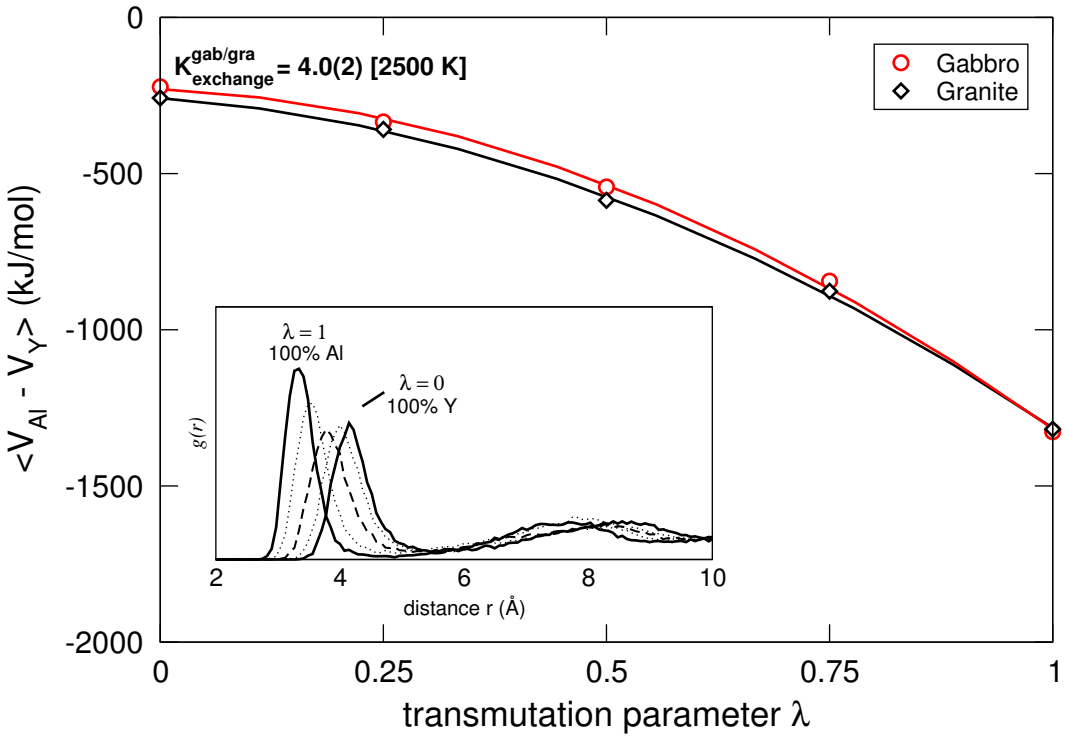

Figure 4.2: Thermodynamic integration (based on classical potentials) for the exchange reactions of Y and Al in a granitic and a gabbroic melt (see Eq. 4.5). Discrete data points represent the average energy difference $< V_{Al} - V_Y >$ for each value of λ. The curves are 4th order interpolations between the data. The area between the two curves corresponds to the total change in Gibbs free energy of the exchange reaction, as outlined in Eq. 4.2. The corresponding equilibrium constant of the reaction is given in the upper left corner. Error bars are smaller than symbols. Inset: Shown is the shift of the RDF of the affected atom during transmutation. The first shell structure gradually changes from that of an Y to that of an Al.

Table 4.3: Thermodynamic integration results from classical and first-principles MD. T_{exc} is the temperature of the transmutation, ΔG_{exc} the calculated change in free energy and K_{exc} the corresponding equilibrium constant. D_{est} is the corresponding *estimated* (see text) partition coefficient at experimental temperatures (T_{exp}). D_{exp} are experimental coefficients derived from the corresponding literature. In classical simulations, ^{super} denotes that the transmutation has been done using a 2x2x2 supercell (up to 856 atoms)

melt pair & element	T_{exc} (K)	ΔG_{exc} (kJ/mol)	K_{exc}	D_{est}	D_{exp}	T_{exp} (K)
			classical MD			
gab/gra Y	2500	-25.6	3.4(1)	8	9.3(18)[1]	1450
gab/gra Y^{super}	2500	-28.8	4.0(2)	10		
gab/gra 2Y	2500	-30.2	4.2(1)	12		
gab/gra 2Y^{super}	2500	-31.1	3.3(1)	8		
gab/gra La	2500	-23.8	3.2(2)	7	9.9(19)[1]	1450
			first-principles MD			
gab/gra Y a	3000	-2.8	1.1(1)	1.2	9.3(18)[1]	1450
gab/gra Y b	3000	3.1	0.9(1)	0.8		
gab/gra As	3000	28.8	0.31(2)	0.09	0.086(52)[1]	1450
asi200/asi280 Y	3000	-31.4	3.5(1)	15*	∼50[2,*]	1400

* - estimate, see text; [1]Schmidt et al (2006); [2]Prowatke and Klemme (2005)

experimental references (D_{exp}) and the corresponding experimental temperature (T_{exp}) in columns 6 to 7.

Given all assumptions and methodical uncertainties the classical MD results for Y and La are in reasonable agreement with experimental data, predicting not only the right direction of partitioning but also the correct order of magnitude, close the experimental uncertainty. The first-principles simulations on the other hand show a different picture. Two independent simulations of the system gabbro - granite containing Y, despite having been integrated from the same initial configurations as the classical MD, show partition coefficients close to 1. Transmutation of a system containing As on the other hand shows both the correct order of magnitude and partitioning behaviour (enrichment in granite). The simulation of the Ti-bearing silicate melts points in the correct direction (preference of asi200) but is too low by a factor of 3. Note, however, that in this case the two melts do not coexist in the experiment and that our derived D describes the relative change of titanite-melt partitioning as a

function of melt composition. In this case, also the reference is only a rough estimate derived from the Y concentration in each melt of the original publication, assuming that the corresponding crystal does not change between the different titanite-melt partitioning experiments (see Prowatke and Klemme, 2005, for experimental details). One reason for the large difference in Y partition coefficients between gabbro and granite melts predicted by first-principles simulations compared to experiments could be that run durations (20 ps run duration as compared up to 200 ps in the classical case) are too short to successfully sample all configurations in phase space and thus finding substantial differences in free energy in the two melts. This would also explain why the predicted D_{As} between the two melts is in closer agreement with experiment than D_Y. Arsenic usually shows coordination numbers close or below 4, which is similar to those of Al. This means that the structural environment of major and trace element involved in the transmutation is already rather similar and thus, the short simulation times suffice to achieve equilibrium. This may not be the case for Y, where the melt has to accommodate a change in coordination from 4 (Al) to 6-7 (Y). Moreover, especially in the more polymerised melt this change of Y coordination is expected to lead to a local rearrangement of the tetrahedral network structure, which may take longer than the total simulation time of 20 ps (e.g. Spiekermann et al, 2016). A possible solution would be to perform transmutations onto sites that already feature high coordination numbers (e.g. onto a calcium site), using coupled substitutions (Ca + Si $\rightarrow$ Y + Al) to remain charge neutral. In particular in the case of the Ti-bearing silicate melts, another source of error could be the activity coefficient of Y in such exotic melt systems, which potentially influence the partitioning by an order of magnitude.

4.4.2 The role of melt composition and structure

The first parameter we consider when trying to shed light on the structural influence on partitioning is the degree of depolymerisation (NBO/T). In this study, both Y and La prefer melts that have a higher degrees of depolymerisation (the gabbroic and the asi200 melt), an effect observed by experiments as well as previous simulations (Haigis et al, 2013; Prowatke and Klemme, 2005; Schmidt et al, 2006). When calculating a hypothetical exchange between the two melts with similar NBO/T (asi280 and granite), the corresponding equilibrium constant is in fact $\sim$1. However, solely relying on NBO/T seems ambiguous when it comes to partitioning. The two Ti-bearing silicate melts that should experimentally differ largely regarding their trace element incorporation (Prowatke and Klemme, 2005) show a much smaller difference in NBO/T ($\sim$0.7 and $\sim$0.3) as compared to the gabbroic and granitic melts ($\sim$2.0 and

$\sim$0.3), yet D-values of the latter are much smaller (up to a D of 10 or 0.1 respectively). To find a more direct link between composition and partitioning, Haigis et al (2013) argue that Y prefers melts with high amounts of Ca, as it performs as a 'weak competitor' for the oxygen needed to create the rather high coordination shell of Y (and La). This observation holds true in the case of the silicate melts investigated here as well, where melts with higher amounts of Ca (and Mg) are preferred by both Y and La. Another general observation is that both elements show higher coordination numbers in the depolymerised melt ($\sim$7 in gabbro as opposed to 6 in granite). For arsenic, the fractionation follows the opposite trend (into the polymerised, granitic melt) and conversely, coordination is lower in granite compared to gabbro. Assuming that Y and La prefer a coordination close to 7 in silicate melts, we can conclude that these elements will always partition into the melt that allows them to attain this environment with the least 'resistance' possible, i.e. where large cations that loosely bond oxygen prevail as compared to oxygen tightly bond in Si, Al or Ti tetrahedra. Thus, in a network dominated by Si and Al polyhedra, ions that form large coordination shells (6-7, Y^{3+}, La^{3+} or also Cr^{3+}) would partition into the more depolymerised melt in order to satisfy their oxygen demands. Ions with potential small first shells similar to those of Al^{3+} (3-4, e.g. As^{3+} or Sb^{3+}) will partition into the polymerised melt to be accommodated within the tetrahedra network. Schmidt et al (2006) argue that, at least for elements that vary only slightly (up to a D of 10) with melt polymerisation, the overall effect on mineral-melt partitioning will be negligible and dominated by the crystal. However, if both effects fall in the same order of magnitude, the melt effect will have to be considered, especially in systems that are not well constraint by experiments yet. In the case of the Ti-baring silicate melt pair, there seems to be no direct influence of the structure (at least in terms of first shell environments) onto partitioning. Due to the lack of suitable interaction potentials we could only investigate these melts using first-principles and thus rather small simulation cells. The latter may inhibit the formation of a proper coordination environments for Y. Given that both melts are structural very similar and that there are no direct experimental data for coexisting melts, the results have to be considered with care. The two melts differ mainly in their Al and Na content and thus, the explanation for the experimentally observed strong melt dependence of the titanite-melt partitioning must lay either in the 'competitor' model discussed above and/or in the chemistry of the crystal as well.

4.5 Conclusions

From the previous discussion we may draw the following conclusions:
(1) it is possible to employ a thermodynamic integration scheme to predict element partitioning, given that simulation times are long enough to thoroughly sample the phase space
(2) the approach seems sensitive enough (even when simulating small systems sizes) to meaningfully predict partitioning with an order of magnitude accuracy
(3) our simulations confirm that elements that require large oxygen coordination shells preferentially partition into melts with high degrees of depolymerisation and thus, comparatively more loosely bond oxygen enabling them to easily satisfy their oxygen requirements. The opposite effect seems to hold true for elements with coordination shells similar to those of Si or Al
(4) to further advance the method, future challenges include the determination of realistic trace element activity coefficients, evaluating the influence of temperature, pressure as well as finite size and time effects on predicted partitioning coefficients and melt structures, as well as taking into account coupled substitutions (in particular for the calculation of mineral-melt partitioning)

Chapter 5

Anisotropy of self-diffusion in forsterite grain boundaries

This chapter is based on the following publication:
Wagner, J., Adjaoud, O., Marquard, K., Jahn, S. (2016)
Anisotropy of self-diffusion in forsterite grain boundaries derived from molecular dynamics simulations
Contributions to Mineralogy and Petrology 171:98 (`http://dx.doi.org/10.1007/s00410-016-1308-y`)

Individual Contributions:
J. Wagner planned and performed research, analysed the data, wrote the paper.
O. Adjaoud was involved in the planing of the research, provided initial structures, participated in analysing the data.
K. Marquard was involved in the planing of the research, the analysis of the data and writing of the paper.
S. Jahn planned and supervised the research, participated in writing the paper.

5.1 Introduction

Grain boundaries (GBs) in oxides and silicates have received increased attention in the last decades, as they are known to influence many key physical and chemical properties of rocks (Dohmen and Milke, 2010) such as reaction kinetics (Keller et al, 2008), fluid transport (Gardés et al, 2012), chemical alteration (Hartmann et al, 2008), electrical conductivity (Pommier et al, 2015) and solid state diffusion (Marquardt et al, 2011). GBs in the mineral group olivine, $(Mg,Fe)_2SiO_4$, have been studied extensively to elucidate their role in the rheological behaviour of the upper mantle. The ongoing debate whether dislocation or diffusion creep dominates the plastic deformation of the mantle and where transitions between the two may occur (Karato and Wu, 1993; Hansen et al, 2012; Hirth and Kohlstedt, 2013), has led to extensive research of the bulk self-diffusion kinetics of olivine (e.g. Chakraborty et al, 1994; Dohmen et al, 2002, 2007; Fei et al, 2012, 2013) and its polymorphs (Farber et al, 1994; Shimojuku et al, 2004; Kubo et al, 2004; Shimojuku et al, 2009). However, in the case of grain boundary self-diffusion rates of olivine, experimental data are limited. Diffusion measurements in forsterite GBs have been reported by Farver et al (1994) for magnesium, Farver and Yund (2000) and Fei et al (2016) for silicon, and Condit et al (1985) for oxygen. Another approach that has been much less utilized so far is to look at (grain boundary) diffusion from a molecular simulation perspective. Such simulations enable us not only to calculate physical and thermodynamic properties of a given system (total energy, electrical conductivity, chemical diffusion) but simultaneously link them to structural properties on a molecular scale. Ammann et al (2010) used static first-principles simulations to calculate bulk diffusion rates in perovskite and periclase. In such static studies, an atom is moved deliberately from its equilibrium position. The calculated energetic response can be translated into diffusion rates. Ghosh and Karki (2013) investigated the energetics and structure of a set of Mg_2SiO_4 forsterite tilt grain boundaries using similar methods and infer that, depending on misorientation, areas of low density in these GBs may serve as fast diffusion pathways. An alternative approach is to perform molecular dynamics (MD) simulations where atoms may move freely depending on the potential applied. Subsequently the systems evolution is tracked over time in order to average over a property of interest. However, simulations based on first-principles are computationally expensive and typically limited to the simulation of a few hundred atoms and picoseconds of simulation time. In the case of GBs, simulation cells need to be sufficiently large to exclude finite size effects (e.g. interaction of repeated GBs introduced by the periodic boundary conditions) and to capture the entire repeat unit length along a GB. To investigate self-diffusion directly by molecular dynamics simulations,

simulation times have to be sufficiently long to generate statistically meaningful displacements of atoms that may be considered as diffusing. One possible solution to these obstacles is to perform MD simulations based not on first-principles but on classical interaction potentials. Such simulations have the advantage that they are computationally much less expensive and thus enable the simulation of comparatively large systems (several 1000 atoms) and long timescales (several nanoseconds). Nevertheless, classical MD still requires comparatively high temperatures to reach a sufficient degree of atomic mobility in order to catch diffusive processes at all. In this study, we estimate major element grain boundary self-diffusion coefficients in a set of Mg_2SiO_4 forsterite tilt grain boundaries using classical MD simulations. We utilize an advanced ionic interaction potential that has been successfully applied in the simulation of many oxides and silicates, including forsterite (e.g. Jahn and Madden, 2007; Adjaoud et al, 2012; Finkelstein et al, 2014).

5.2 Simulation Procedure

5.2.1 Grain boundary setup

We constructed several Mg_2SiO_4 forsterite (space group *Pbnm*, $a = 4.7535$ Å, $b = 10.1943$ Å, $c = 5.9807$ Å $\alpha = \beta = \gamma = 90°$) grain boundaries with misorientation angles varying from 9.58° to 90°. Details about the procedure, grain boundary energies and structure of all (0kl)/[100] symmetric tilt grain boundaries are reported in Adjaoud et al (2012). In short, they are generated by cutting intact grains at a specific angle and rotating one half of the thus created bicrystal with respect to the other by 180°, the axis of rotation perpendicular to the cutting plane. The thus constructed symmetric tilt grain boundary is subsequently equilibrated at ambient conditions. Additionally, as they are among the most abundant GBs in undeformed forsterite aggregates (Marquardt et al, 2015), a 90° misorientation grain boundary containing 9744 atoms is constructed by bringing in contact two forsterite grains with free (100) and (010) surfaces. We then systematically shift the two grains with respect to each other along the interface plane. Subsequently the total energy of each configuration is calculated until a stable structure is found. The new cell containing the 90° misorientation grain boundary is then annealed at ambient conditions. The termination of the (100) and (010) surfaces is chosen as to represent the lowest energy termination according to Watson et al (1997).

5.2.2 Estimating self-diffusion coefficients from MD simulations

We use classical MD simulations to study the structure and transport mechanisms of the constructed grain boundaries. First, we equilibrate each system at ambient pressure and temperatures between 1900-2200 K (NPT ensemble, constant number of particles N, constant pressure P, constant temperature T) for at least 2 ps. Given the short timescale available to our simulations, such comparatively high temperatures are necessary to reach a sufficient degree of atomic mobility. The temperature and pressure are controlled by a Nosé-Hoover thermostat (Nosé and Klein, 1983) coupled to a barostat (Martyna et al, 1994). We subsequently fix the cell volume V and track the systems evolution at a given temperature for at least 1000 ps with 1 fs timesteps (NVT ensemble using a Nosé-Hover thermostat to control the temperature (Nosé, 1984)). System sizes range from 4032 to 9744 atoms, periodic boundary conditions are applied in every simulation. The movement of individual elements is evaluated by analysing their mean squared displacements (MSD) over the duration of the simulation. Self-diffusion coefficients can then be estimated using Einstein's relation between self-diffusion coefficient and MSD (Allen and Tildesley, 1987):

$$D_i = \lim_{t\to\infty} \frac{\left\langle (\boldsymbol{r}(t+t_0) - \boldsymbol{r}(t_0))^2 \right\rangle}{2 \cdot dim \cdot t} \tag{5.1}$$

where D_i is the self-diffusion coefficient of element i (Mg, Si, O). $\boldsymbol{r(t)}$ is the position vector of an individual atom of type i at time t and dim the dimensionality of the system. The numerator at the right hand side of Eq. 5.1 is the mean squared displacement, which is averaged over all atoms N_i of a specific element i starting with an initial time t_0 (angular brackets). Eq. 5.1 is defined for systems where all atoms of a specific element contribute to a homogeneous self-diffusion coefficient (e.g. a fluid). However, in the case of grain boundaries, diffusion within the bulk crystal can be several orders of magnitude slower as compared to the GB (e.g. Farver and Yund, 2000; Dohmen and Milke, 2010; Marquardt et al, 2011). As a consequence, a MSD that averages over all the atoms of a specific element in these systems also averages over the comparatively immobile atoms within the bulk crystal. This leads to a considerable underestimation of the grain boundary diffusion and it is thus compulsory to treat the GB and the bulk crystal as two sub-systems (e.g. Fisler and Mackwell, 1994). Therefore, we analyse the distribution of the MSDs of each individual atom and only consider those that have been displaced more than 7 Å^2 at a time interval of at least 1000 ps and hence contribute significantly to GB diffusion. We chose this cutoff in order to make sure that atoms that are con-

sidered in the calculation have at least moved beyond their nearest neighbour distance. To gain further insight into the influence of grain boundary geometry and stability on the self-diffusion coefficient we also calculate the excess free volume (V_{Gb}) of each individual GB as follows:

$$V_{Gb} = \frac{V_{bc} - V_{sc}}{2A_{Gb}} \tag{5.2}$$

where V_{bc} and V_{sc} are the total volumes of a the grain boundary cell and a reference single crystal, respectively. A_{Gb} is the area of the grain boundary.

5.2.3 Classical interaction potential

All simulations are performed using a set of classical interaction potentials for the Calcium-Magnesium-Aluminosilicate (CMAS) system, parametrised by reference to first-principles electronic structure calculations (Jahn and Madden, 2007). In addition to charge-charge (Coulomb) interactions and dispersion, this model includes true many-body effects by accounting for polarization effects (electronic multipoles up to quadrupoles) as well as aspherical shape deformation of anions, depending on their local environment (Madden et al, 2006). Multipoles and shape deformations are computed self-consistently at each simulation step. Such aspherical ion model (AIM) potentials have been successfully applied in the simulation of several geomaterials including forsterite (Jahn and Madden, 2007; Jahn and Martoňák, 2008; Jahn, 2010; Adjaoud et al, 2011), oxide and silicate melts and interfaces (Adjaoud et al, 2008; Jahn and Madden, 2008; Gurmani et al, 2011) as well as forsterite grain boundaries (Adjaoud et al, 2012). All simulations in this contribution are performed using the CP2K code package (Hutter et al, 2014) with an implementation of the AIM potential type made recently by the authors. All potential parameters are listed in Jahn and Madden (2007).

5.3 Results

Grain boundary self-diffusion coefficients for magnesium, silicon and oxygen for the respective temperatures are given in Table 5.1. In the case of silicon and occasionally oxygen, self-diffusion rates are very slow and only few atoms move beyond the MSD cutoff (see above) within the simulation timeframe. This makes it impossible to extract meaningful self-diffusion coefficients and the respective entries in the dataset are thus left blank. Experimental data for the temperature range of our simulations are not available. However, Figs.

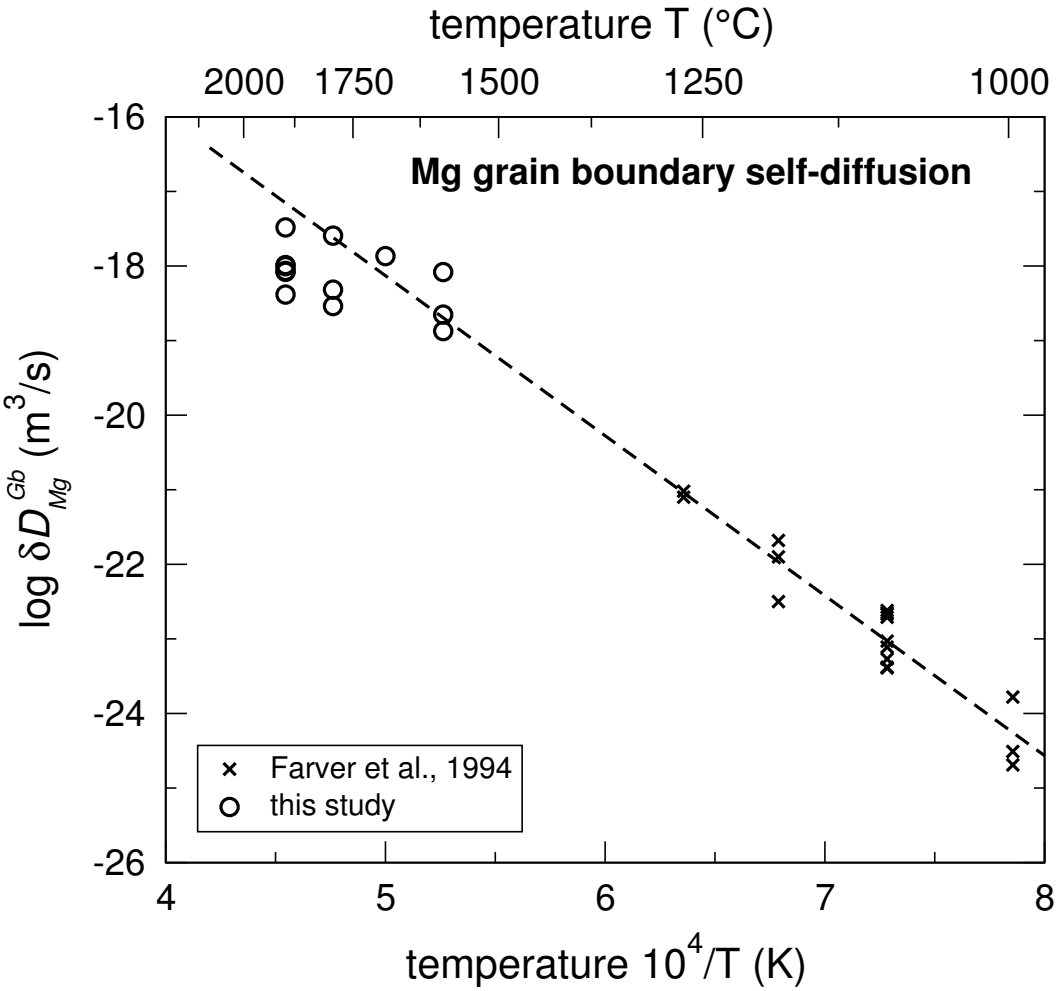

Figure 5.1: MD simulation results and experimental data for magnesium self-diffusion coefficients ($\delta = 1nm$). Error bars are smaller than symbols. The dashed line is a linear extrapolation of data by Farver et al (1994).

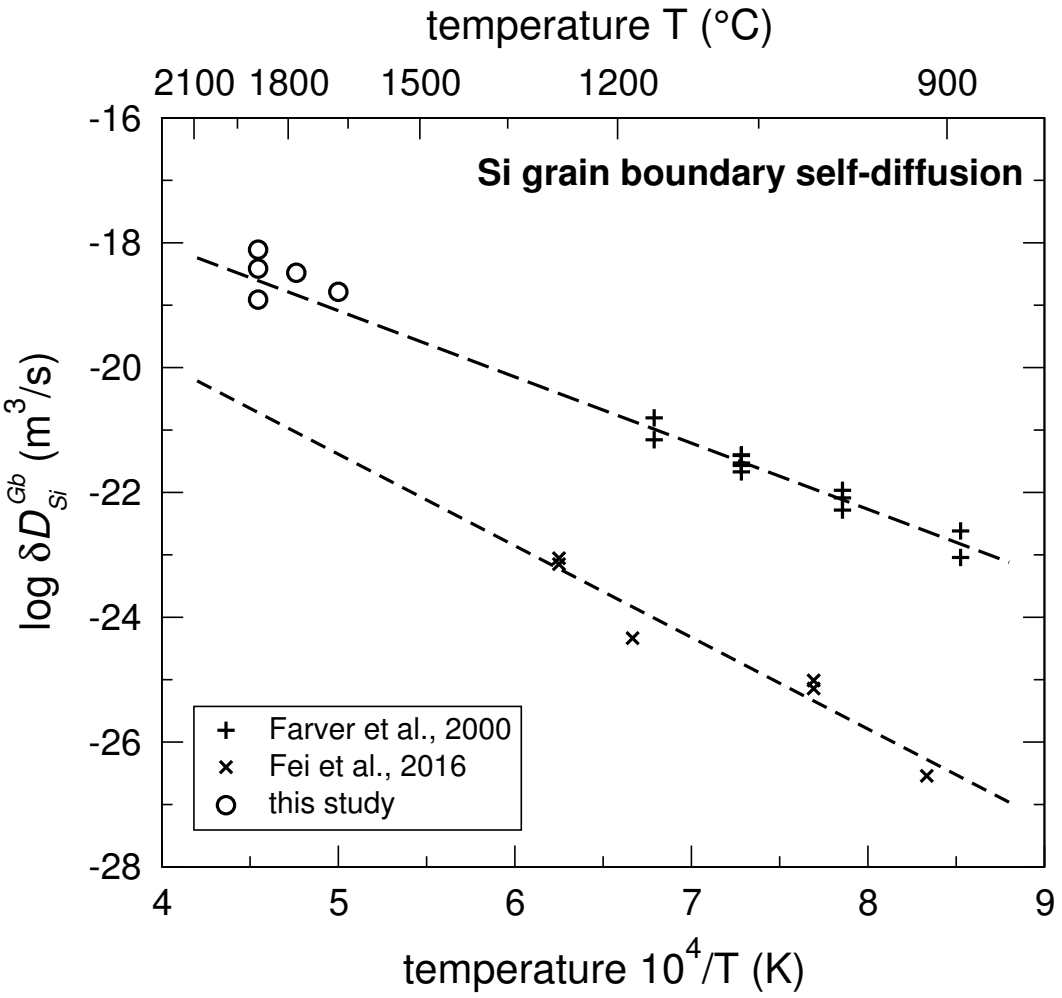

Figure 5.2: MD simulation results and experimental data for silicon self-diffusion coefficients ($\delta = 1nm$). Error bars are smaller than symbols. The dashed lines are linear extrapolations of data by Farver and Yund (2000) and Fei et al (2016).

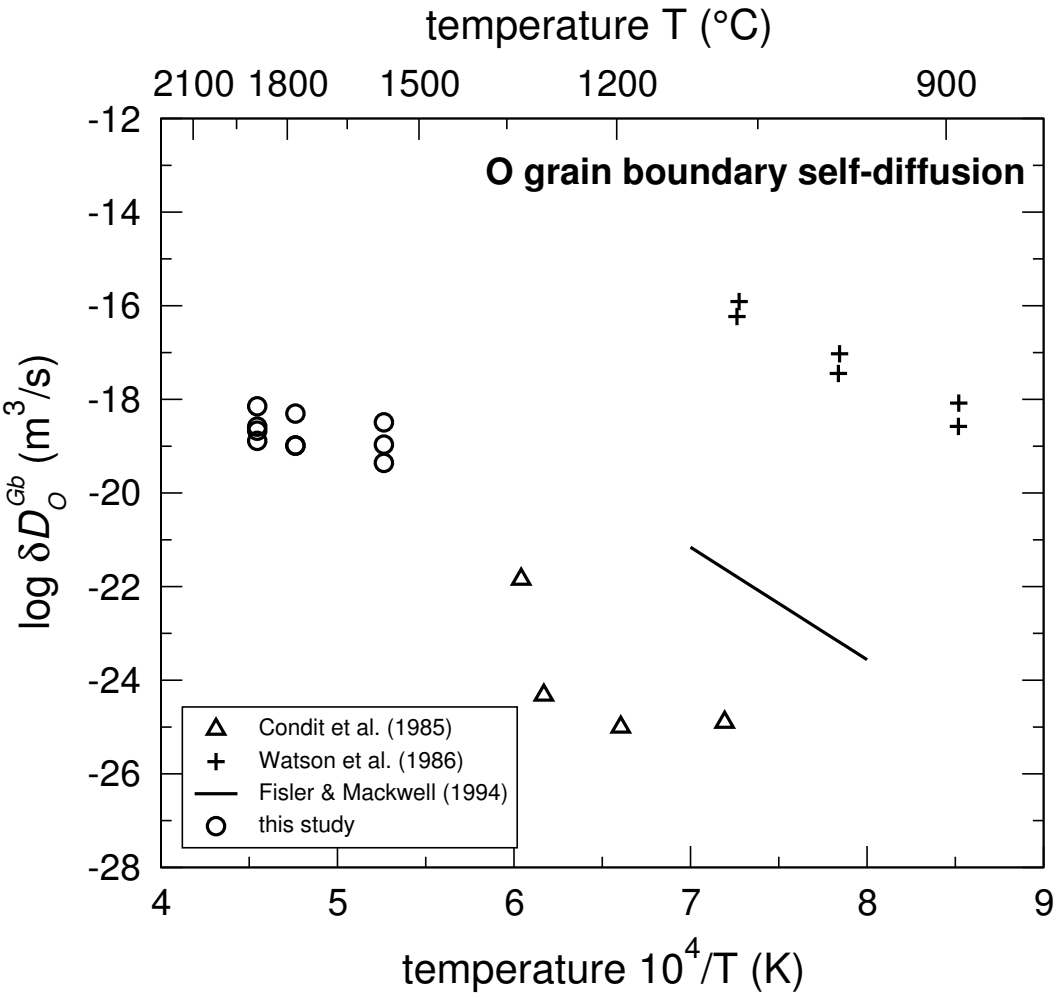

Figure 5.3: MD simulation results and experimental data for oxygen self-diffusion coefficients ($\delta = 1nm$). Error bars are smaller than symbols.

Table 5.1: MD simulation results for all investigated grain boundaries comprising Mg, Si and O self-diffusion coefficients derived from their MSDs after 1000 ps run duration ($\delta = 1nm$). Additionally, the free excess volume for every configuration is given (see text). Gaps in the dataset occur when diffusion was to slow to be statistically captured by the MSD method.

GB angle (°)	T (K)	δD^{Gb}_{Mg} $(10^{-19}m^3/s)$	δD^{Gb}_{Si} $(10^{-19}m^3/s)$	δD^{Gb}_{O} $(10^{-19}m^3/s)$	V_{Gb} $(Å^3/Å^2)$
9.58	2200	8.34	-	-	0.66
11.17	2200	1.03	-	2.61	0.72
16.69	2200	9.93	5.77	2.14	0.80
32.7	2200	9.98	-	-	0.94
	2100	4.82	-	1.02	1.00
	1900	2.23	-	1.08	0.92
60.8*	2200	3.42	-	-	0.34
60.8	2200	4.14	-	1.30	0.55
	2100	2.90	-	1.04	0.51
	1900	1.34	-	0.44	0.52
90.0	2200	32.9	7.75	7.11	1.30
	2100	25.5	3.31	4.97	1.20
	2000	13.6	1.64	3.09	1.19
	1900	83.0	-	3.23	1.18

*asymmetrical

5.1, 5.2 and 5.3 compare our results to linear extrapolations of various experimental studies in lower temperature regimes. Grain boundary excess volumes calculated according to Eq.5.2 are also given in Table 5.1.

5.4 Discussion

5.4.1 Self-diffusion coefficients

Overall, data derived directly from our MD simulations fit well to the extrapolations of lower temperature experimental data. In the case of Mg it appears that the change of D^{Gb}_{Mg} with temperature flattens out in the high temperature field. This may be explained by the fact that for such high temperatures, approaching the melting point of forsterite, activation energy for the breaking of bonds is lowered to a minimum and diffusivity ultimately levels out to a rate of an equivalent silicate melt, which is in the order of magnitude of 10^{-18} m^3/s for Mg (Gurmani et al, 2011; Adjaoud et al, 2011). In the case of Si, the few data that can be extracted from our simulations plot on the linear regression of the dataset of Farver and Yund (2000) but diverge from an extrapolation of data recently published by Fei et al (2016) by two orders of magnitude. Oxygen self-diffusion rates predicted by our simulations diverge by several orders of magnitude from experimental data. However, oxygen experimental data themselves are in rather big disagreement, ranging from 10^{-16} - 10^{-24} m^3/s for temperatures between 1200 - 1500 K. The large discrepancies may be due to the various methodologies employed in the experiments, comprising isotopic tracers (Condit et al, 1985), rim growth measurements (Fisler and Mackwell, 1994) and indicator mineral reactions (Watson, 1986). The low self-diffusion rates predicted by our simulations may be due to the used AIM potential, which is known to generally predict too strong oxygen bonds, thus reducing oxygen mobility (Adjaoud et al, 2011).

5.4.2 Grain boundary transport mechanisms and volume dependence

To visualise the molecular scale transport mechanism in different GB types, Figs. 5.4 and 5.5 show exemplary snapshots of the MD trajectories for a low angle (9.58°) and a high angle grain boundary (60.8°). The upper panels (A) in both figures show the overall displacement of individual atoms at the last snapshot of the the respective simulation. Low angle GBs in general can be described as an array of aligned partial dislocations and stacking faults (e.g. Ikuhara et al, 2003, in alumina). In Fig. 5.4 it is readily visible that diffusion

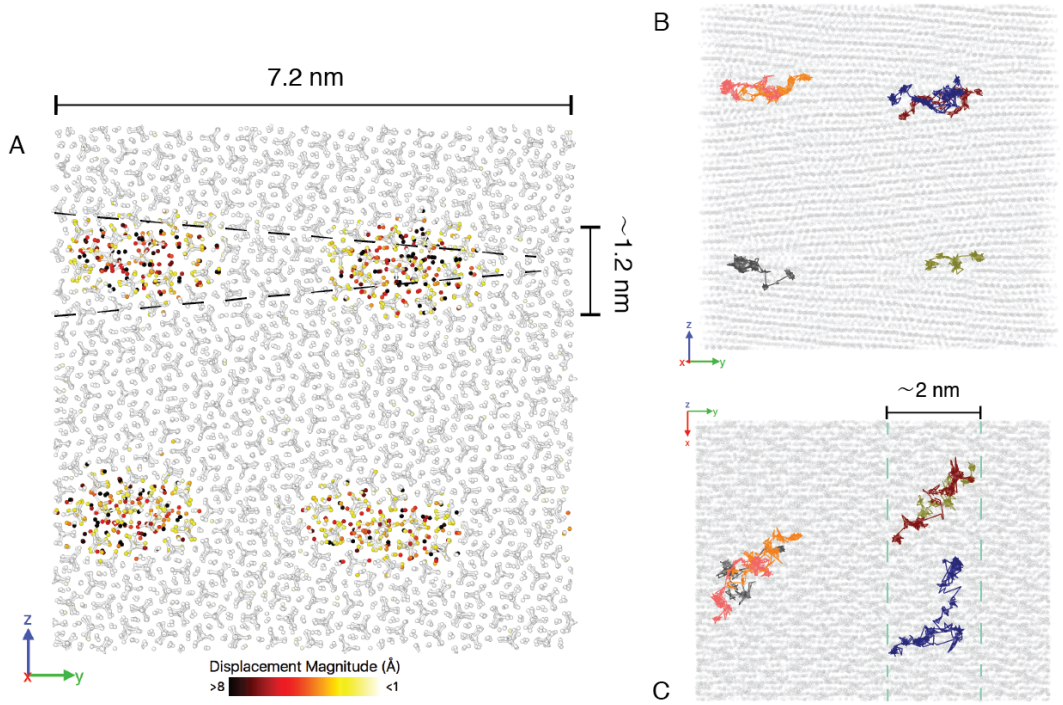

Figure 5.4: A: Snapshot of the trajectory of a low angle grain boundary (9.58° misorientation) with individual atoms coloured according to their overall displacement with respect to the first step of the run. The black dashed lines indicate the misorientation angle. The panels B and C show exemplary trajectories of Mg atoms propagating through the diffusion channel (see text). The green dashed line indicates the extend of one of these channels. Different trajectory colours are individual atoms. The cell in B is rotated about 2° around the z-axis. All figures are created using the OVITO software (Stukowski, 2010).

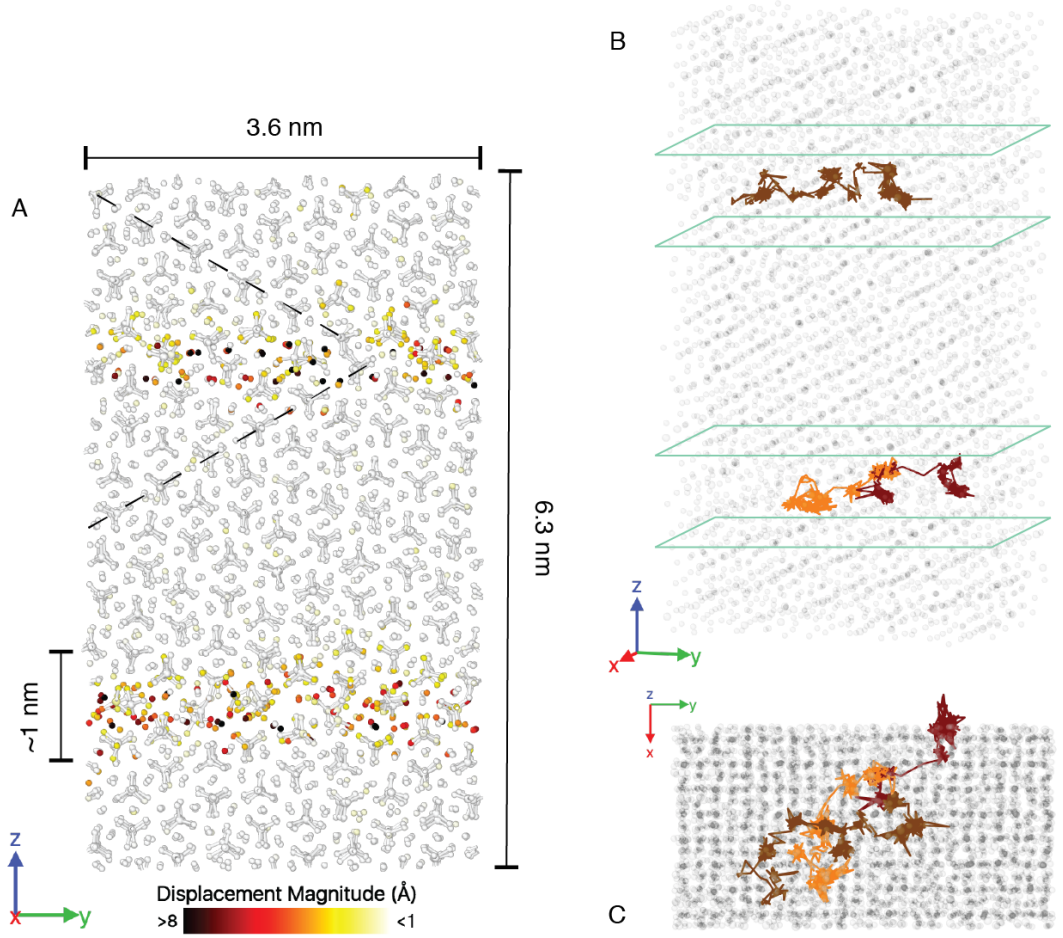

Figure 5.5: A: Snapshot of the trajectory of a high angle grain boundary (60.8° misorientation) with individual atoms coloured according to their overall displacement with respect to the first step of the run. The black dashed lines indicate the misorientation angle. The panels B and C show exemplary trajectories of Mg atoms propagating through the diffusive layer (outlined in green) of the GB interface (see text). Different trajectory colours are individual atoms. The cell in B is rotated about 20° around the z-axis. All figures are created using the OVITO software (Stukowski, 2010).

takes place in a confined space around these partial dislocations in the bicrystal lattice (see Adjaoud et al (2012) for a detailed analysis of the structures presented). These areas of highest mobility are likely correlated to the spatial extend of the dislocation cores, have radii of approximately 1.2 - 2 nm and propagate cylindrical through the grain boundary interface, parallel to the a-axis of the two forsterite crystals (the x-axis in Fig. 5.4, the dashed green line outlines such a diffusion channel). When analysing exemplary trajectories of Mg atoms through these diffusion channels one can observe a typical diffusion pattern where longer jumps are intermitted by phases of stagnation (e.g. Fig. 5.4 lower two panels). However, diffusion paths are not straight along the length of the channel but may also span its width entirely. High angle grain boundaries on the other hand show no such diffusion channels (Fig. 5.5). Here, the area of highest mobility spans the entire grain boundary interface, about 1 - 2 nm in width. Atoms move more or less randomly in any direction parallel to the interfacial plane whereas in the low-angle grain boundary, a long-term transport between two channels within the same GB interface plane (parallel to the y-axis in Fig. 5.4) should be considered rather slow, thus greatly limiting diffusion in this direction. These two modes of transport, however, do not necessarily result in enhanced or reduced overall self-diffusion within a GB. Instead, it seems that the rate-determining factor is the overall free excess volume of a grain boundary at any given temperature. Fig. 5.6 shows the calculated self-diffusion coefficients as a function of free excess volume for different temperatures. Both slowest and fastest rates are observed in high-angle grain boundaries (60.80° and 90° misorientation). On the other hand, the relation to the grain boundary energy is much less pronounced, as e.g. the 32.70° GB exhibits the overall lowest GB energy (at ambient conditions) of the set investigated by Adjaoud et al (2011). A theoretical relationship between excess free volume and self-diffusion coefficients has previously been proposed by Chuvil'deev (1996). More generalised, excess free volume as a measure of 'non-equilibrium state' of GBs in metals has been suggested to correlate with key physical properties such as sliding, migration and segregation (Chuvil'deev et al, 2002; Petegem et al, 2003). Tucker and McDowell (2011) infer from atomistic simulations that different initial GB configurations retain their excess free volume differently under stress. This raises the question of how the self-diffusion coefficients presented here will vary with the respective GB free volume under pressure (e.g. under mantle conditions). It is likely that different forsterite GB configurations will react differently to mantle conditions and thus change in their relative contribution to average diffusion in the polycrystaline bulk rock.

5.5 Conclusion

From the preceding discussion we may draw the following conclusions:
1. grain boundary diffusivity in olivine is explicitly dependent on the type of GB, specifically on its excess free volume
2. (self-) diffusion in low angle grain boundaries shows a strong anisotropy which may be explained by their structure of stacked (partial) dislocations. On the contrary, the GB diffusion in high angle GB is essentially isotropic in the GB plane
3. classical MD simulations are a viable tool to study diffusive processes at within grain boundaries at high temperatures, given that sufficiently long trajectories can be achieved.

Further work should be focused one the effect of pressure on the free volume and the related self-diffusion in forsterite grain boundaries in order to obtain a better understanding of GB diffusion in olivine under conditions of the upper mantle.

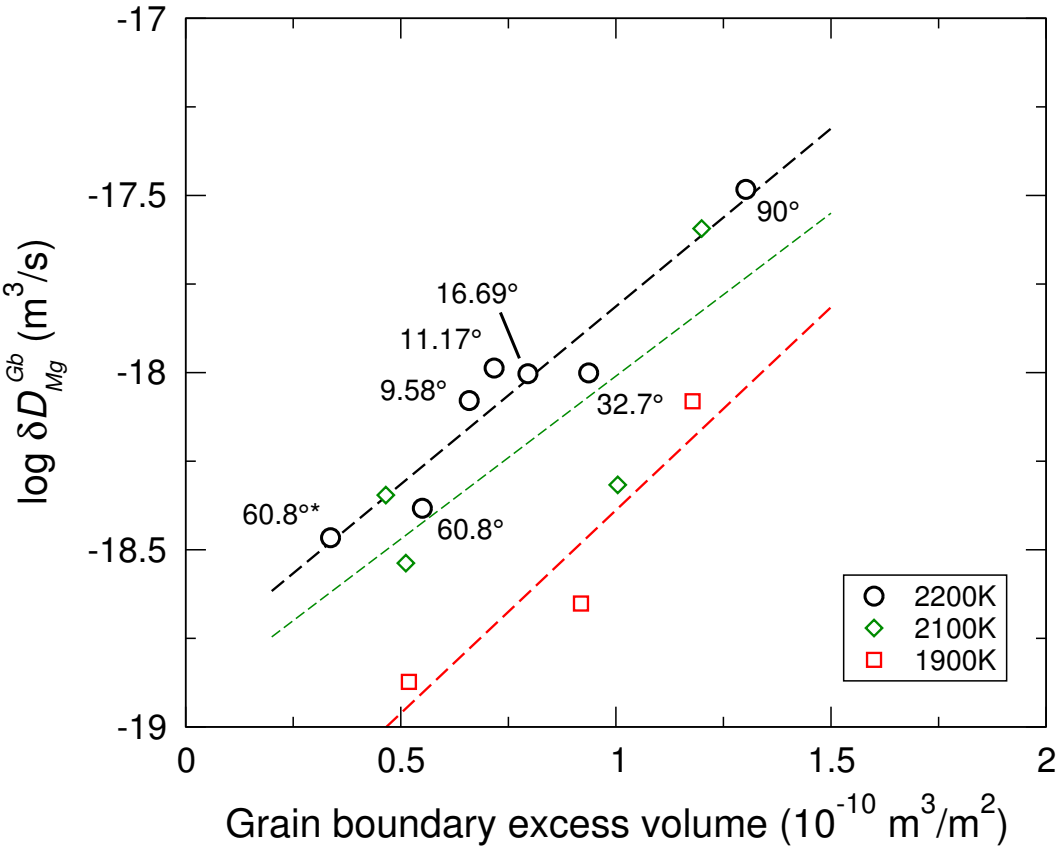

Figure 5.6: Grain boundary self-diffusion coefficients (Mg) versus grain boundary excess volume for different T. Dashed lines are linear fits to the data. *-asymmetrical grain boundary.

Chapter 6

Conclusions and outlook

Several example applications of molecular simulations in geoscience are discussed in this thesis. One is the investigation of the rare earth elements (REE) yttrium and lanthanum in aluminosilicates and how their structural environment changes with composition. To this end, several Y and La bearing glasses and melts are investigated using a combined approach of first-principles and classical molecular dynamics simulations as well as experimental studies. This study uses classical interaction potentials newly developed by co-workers (DIP-PIM) and the author (QUAIM) and thus also serves as a benchmark for their application in the following chapters. In the chapter it is shown that firstly, the average coordination of REE decreases with increasing concentration and secondly, the average coordination of Al is higher in Y bearing melts and glasses as compared to their La counterpart. These findings are generally in fair agreement with experimental neutron- and x-ray diffraction studies conducted on the same compositions. Moreover, the simulations give insight regarding the Y-O/Al-O polyhedral structure to explain some features observed in experiments. Several conclusions are drawn from this chapter. One is that the Al avoidance rule obeyed in aluminosilicate minerals was almost completely invalidated in REE-bearing aluminosilicate melts. Also it is shown that the employed simulations methods are principally suited to describe the structures of such complex silicate melts (coordination environments and especially neutron scattering data), however problems remain regarding the simulation of glasses. While their general structure can be reasonably reproduced, details of the structure factors are either over- or underestimated. This is either due to the very fast quenchrates of the glasses due to limited MD simulations times or shortcomings in the employed interaction potential. However, these problems are particularly pronounced in systems containing high amounts of Y and La, while in nature, these elements usually occur in trace amounts only.
The second study uses, again in conjunction with first-principles simulations,

the classical QUAIM potentials to explore a new tool to predict trace element distributions during magmatic processes. Here, a thermodynamic integration approach is employed to determine the Gibbs free energy change of an exchange reaction between two phases. The study shows that it is principally possible to derive element partition coefficients in this manner, by reproducing the findings of two independent experimental melt-melt and melt-mineral partitioning studies. Prerequisites for this method are (a) that the element's partition coefficient is large enough (presumably at least in the order of 10) to be detectable within the statical uncertainties and (b) that the molecular dynamics simulations are sufficiently long to sample all configurations in phase space. This study also focuses on the effect of melt composition on the observed partitioning behaviour. It is concluded that elements requiring large oxygen coordination shells preferentially partition into melts with high degrees of depolymerisation and thus, comparatively more loosely bond oxygen, enabling them to easily satisfy their oxygen requirements. The opposite effect seems to hold true for elements with coordination shells similar to those building tetrahedral units in the melt network (Si or Al). Further work is necessary to test the pressure and temperature limits of this method. However, it bears the potential to enable the prediction of partition coefficients in geoscientifically relevant systems that are not well constraint or not well accessible by experiments (e.g. carbonate melts). Also during this particular study, the QUAIM potential was implemented into the CP2K software by the author and will be published in a coming version of the code.
Chapter 5 investigates element transport properties in forsterite grain boundaries, elucidating how grain boundary structure hinders or enhances self-diffusion. This is done by tracing atoms (Si, Mg and O) along grain boundaries with varying misorientation angle by means of comparatively long classical molecular dynamics simulations. The atomic trajectories are used to calculate the mean squared displacements of these atoms and infer their self-diffusion coefficients. Not only is it possible to reproduce experimentally determined self-diffusion coefficients in these grain boundaries but also to show that there is a strong anisotropy in terms of direction of diffusion in low- and high-angle grain boundaries. Furthermore, it is shown that the diffusion coefficient directly relates to a grain boundary's free excess volume, a relationship that has been theoretically predicted but never directly been shown. The study is based on forsterite grain boundaries provided by a co-worker. All simulations described in the study, as well as data analysis and evaluation have been conducted by the author.
Combining the simulation of transport properties in such aggregates as well as insight into melt-mineral (i.e. element-) exchange reactions with an in-depth

structural knowledge of the phases involved, clearly bears a lot of opportunity. Molecular simulations may soon be able investigate systems relevant to earth science and crossing any of these scales. It is however desirable to further improve upon the theoretical models used in this thesis. The thermodynamic integration method for example shows potential, but is computationally rather expensive and some issues arising in the first-principles simulations need to be addressed. There are other methods to obtain free energy changes from atomistic simulations (e.g. Umbrella sampling or free energy perturbation) which could be explored for theoretical partitioning studies. The classical interaction potential still has some caveats that can be addressed, e.g. the over bonding of cation-oxygen bonds that leads to shifted structure factors. Another improvement would be to extend the potential to include water or other, strongly polarisable anions such as chlorine in addition to oxygen. Particularly water poses the problem of finding formalisms to describe dissociation processes and how to unify interaction potentials in radically different environments (i.e. that an oxygen my be equally part of a water molecule as well as a SiO_4 tetrahedra). First-principles methods on the other hand will undoubtedly advance even further in the coming years, as their major drawbacks, namely rather small system sizes and very short equilibration times are being increasingly compensated by the constant increase of computing power available. Undoubtedly molecular simulations will be more and more established as an additional tool to study the processes of deep earth environments and planetary systems in general.

Appendix

Fitting classical interaction potentials

Traditionally, classical interaction potentials have been fitted empirically to reproduce experimental data (Fumi and Tosi, 1964; Tosi and Fumi, 1964; Lantelme and Turq, 1982). However, since the advancements in theory and computational power have made first-principles techniques affordable, a new tool to develop classical force fields has become available. First-principles MD is considered to be very accurate but is unfortunately unable to access time scales needed to predict many material properties. The ultimate aim of fitting classical force fields to first-principles data is to reproduce the same inter atomic forces a first-principles simulation would have predicted. If this is achieved, the entire MD trajectory will mimic that of a first-principles calculation, yet featuring all advantages of a classical simulation (large system sizes and long run durations). This so called force-matching approach (Laio et al, 2000) has been applied to generate the classical potentials used in this thesis (DIPPIM and QUAIM, see Chap. 2.3).
A central goal of the utilised ionic models is to be transferable to a variety of temperatures, pressures and conditions. We therefore fit the model parameters to series of configurations (e.g. high and low pressure phases, different configurations of liquids), that ideally should be represented. The first step is to calculate from first-principles the forces, stress tensor and multipole moments for all these individual configurations. The forces and stresses are readily obtained by finding the ground-state electronic wave function (see Chap. 2.2). The multipole moments can be derived from DFT simulations by calculating maximally localized Wannier function (Marzari and Vanderbilt, 1997; Silvestrelli and Parrinello, 1999). The second step is to adjust the model parameters to optimally reproduce DFT data, beginning with the multipole moments. This is done by iteratively adjusting model parameters that influence the classical multipole moments in order to minimise the functions

$$\chi^2_D = \frac{1}{N_c}\sum_{n=1}^{N_c}\frac{1}{N_j}\sum_{i=1}^{N_j}\frac{\mid \boldsymbol{\mu}^i_{DFT} - \boldsymbol{\mu}^i_{classical} \mid}{\mid \boldsymbol{\mu}^i_{DFT} \mid^2}$$
$$\chi^2_Q = \frac{1}{N_c}\sum_{n=1}^{N_c}\frac{1}{N_j}\sum_{i=1}^{N_j}\frac{\sum_{\alpha\beta} \mid \boldsymbol{\theta}^i_{\alpha\beta,DFT} - \boldsymbol{\theta}^i_{\alpha\beta,classical} \mid}{\sum_{\alpha\beta} \mid \boldsymbol{\theta}^i_{\alpha\beta,DFT} \mid^2} \tag{6.1}$$

where N_c and N_j are the number of configurations and number of ions of configuration j, respectively. $\boldsymbol{\mu}$ and $\boldsymbol{\theta}$ are the dipole and quadrupole moments, derived from either first-principles or the classical model (Salanne et al, 2012a). All parameters for the multipole moments are subsequently fixed, and forces and stresses are fitted in a similar fashion

$$\chi^2_F = \frac{1}{N_c}\sum_{n=1}^{N_c}\frac{1}{N_j}\sum_{i=1}^{N_j}\frac{\mid \boldsymbol{F}^i_{DFT} - \boldsymbol{F}^i_{classical} \mid}{\mid \boldsymbol{F}^i_{DFT} \mid^2}$$
$$\chi^2_S = \frac{1}{N_c}\sum_{n=1}^{N_c}\frac{1}{N_j}\sum_{i=1}^{N_j}\frac{\sum_{\alpha\beta} \mid \boldsymbol{\sigma}^i_{\alpha\beta,DFT} - \boldsymbol{\sigma}^i_{\alpha\beta,classical} \mid}{\sum_{\alpha\beta} \mid \boldsymbol{\sigma}^i_{\alpha\beta,DFT} \mid^2} \tag{6.2}$$

where $\boldsymbol{F}$ and $\boldsymbol{\sigma}$ are the forces and stresses tensors of configuration j. The only interaction that has not been accounted for is the dispersion interaction (Eq. 2.11). Dispersion interactions can not be accurately represented by DFT methods that rely on exchange correlation functionals (Hult et al, 1999) and thus, they are empirically fixed before the fitting procedure. The parameters obtained after minimising Eqs. 6.1 and 6.2 are given in Tab. 2.1 for the QUAIM model and Tab. 6.1 for DIPPIM.

QUAIM implementation in CP2K

The aspherical ion model (AIM) has been implemented into the CP2K molecular simulation software package during the work of this thesis for several reasons. CP2K is free and open-source and provides an accessible platform for anyone wanting to use the AIM interaction potentials. It also offers a variety of features (among which is the thermodynamic integration scheme used in this thesis) and a well developed first-principles simulation module next to a variety of additional classical interaction potentials. It shows very good scalability on modern supercomputing architectures and lastly, CP2K has an active community and new features are being developed and implemented constantly. The AIM is implemented into the classical mechanics module (FIST) of CP2K. Figure 6.1 shows the callgraph of a CP2K run using the new implementation. This example is a molecular dynamics run, so the first routine

Table 6.1: Interaction parameters, see equations (2.11), (2.12) and (2.14), in atomic units. Interactions not listed or left blank here, e.g., short-range repulsion for Si–Si, are taken to be absent in the model. Since $b_D^{ij} \neq b_D^{ji}$ for polarisable ions, both parameters are listed. Parameters courtesy Dr Volker Haigis.

i–j	O–O	Si–O	Al–O	La–O	Y–O	La–La	Y–Y
q_i	-2	+4	+3	+3	+3		
DIPPIM parameters							
A_{ij}	5328.3	44.624	39.404	49.165	95.048		
a_{ij}	3.1526	1.6513	1.6413	1.4658	1.6813		
B_{ij}				10^5			
b_{ij}				4.2			
C_6^{ij}	52.461			45.041	23.763	41.213	12.504
b_{disp}^{ij}	2.7370			1.0	1.4995	1.0	0.67066
α_i	10.754			7.3962	3.5475		
b_D^{ij}		1.6489	1.5573	1.3460	1.5056		
b_D^{ji}				3.2197	3.3585		

to be called is CP2K's MD module, *qs_mol_dyn_low*, from which the initial velocities are set up (*velocity_verlet*) and the main routine for FIST energy and forces ($fist\_calc\_energy\_force$) is called. In its most complex form, the AIM gives an oxide anion senventeen degrees of freedom to adjust to its local environment (dipoles, quadrupoles and shape deformations), mimicking the electronic density distribution of a first-principle calculation. At each time step, the code searches for the ground state configuration of these degrees of freedom using a conjugate gradient algorithm (Press et al, 1992; Shewchuk, 1994) i.e.

$$\begin{aligned} \left(\frac{\partial V^{rep}}{\partial \xi^j}\right)_{\{\xi^M\}} &= 0, \quad \text{where } \left\{\xi^M\right\} = \left\{\delta\sigma^N, \nu_\alpha^N, \kappa_{\alpha\beta}^N\right\} \\ \left(\frac{\partial V^{pol}}{\partial \xi^j}\right)_{\{\xi^M\}} &= 0, \quad \text{where } \left\{\xi^M\right\} = \left\{\mu_\alpha^N, \theta_{\alpha\beta}^N\right\} \end{aligned} \tag{6.3}$$

$\delta\sigma^N$,ν_α^N and $\kappa_{\alpha\beta}^N$ are the ionic shape deformation terms (spherical, dipolar and quadrupolar, respectively, see Chap. 2.3), μ_α^N and $\theta_{\alpha\beta}^N$ are the dipole and quadrupole moments. N are the number of ions of species j. Because the shape deformations and polarisations are converged independently, the corresponding CP2K calls are split up into a polarisation- ($fist\_pol\_evaluate\_cg$) and a deformation branch (aim_energy_cg). Typical convergence criteria are

are tolerated difference of 10^{-8} in the polarisation and 10^{-10} in the deformation minimisations. Because polarisation effects are partially treated in reciprocal space, the $fist\_pol\_evaluate\_cg$ into a long-range and a short-range ($ewald\_multipole\_SR$) part.

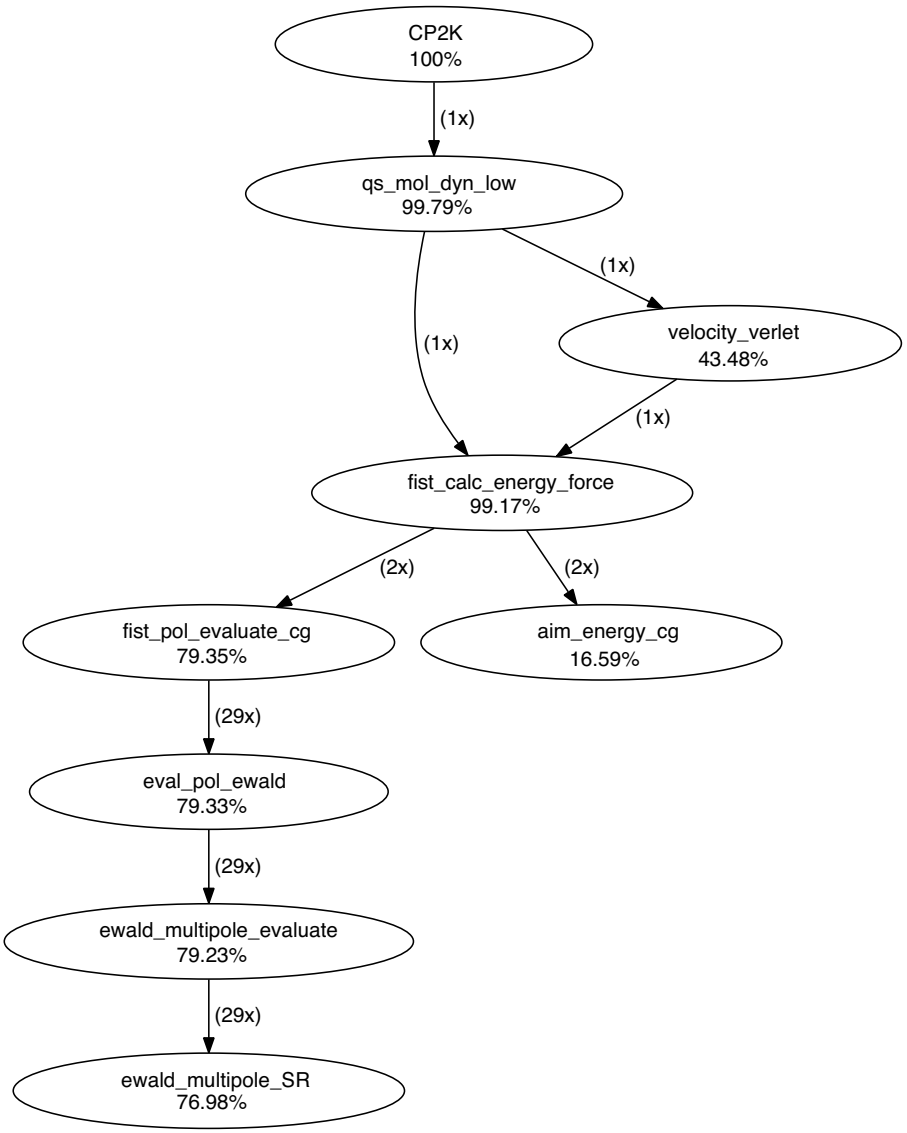

Figure 6.1: CP2K callgraph showing the subroutines involved in an QUAIM molecular dynamics simulation. For the implementation, the *fist_pol_evaluate_cg* routine has been modified to include quadrupoles. The conjugate gradient algorithm minimising the ion deformations has been newly implemented. The percentages give an estimate of the distribution of the computational effort. Thus, the computationally most expensive part of this example is the convergence of the induced multipoles.

Addendum to Chapter 4

This section contains the radial distribution functions of the asi200 and asi280 melts discussed in chapter 4 as well as the absolute compositions of all melts studied in that chapter. These are also the contents of an electronic supplement that is submitted together with original publication of chapter 4.

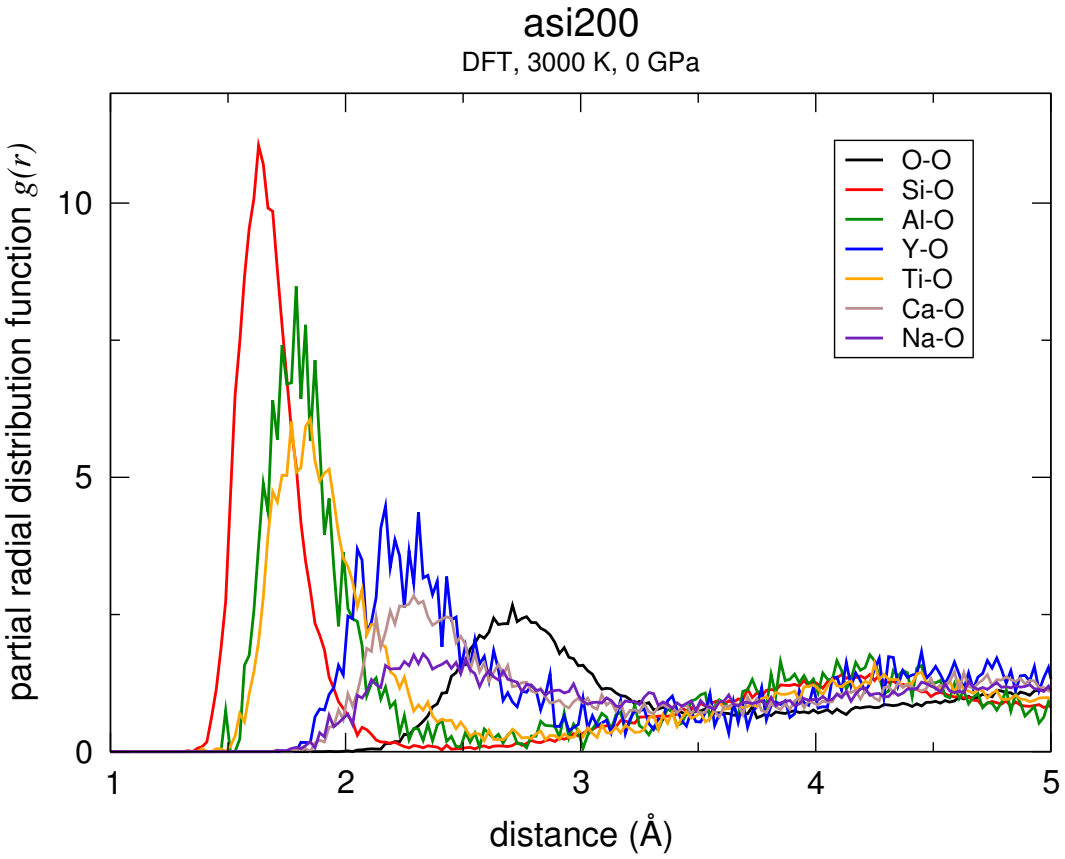

Figure 6.2: Partial radial distribution functions of the asi200 melt doped with one Y, derived from first-principles MD at 3000 K and 0 GPa.

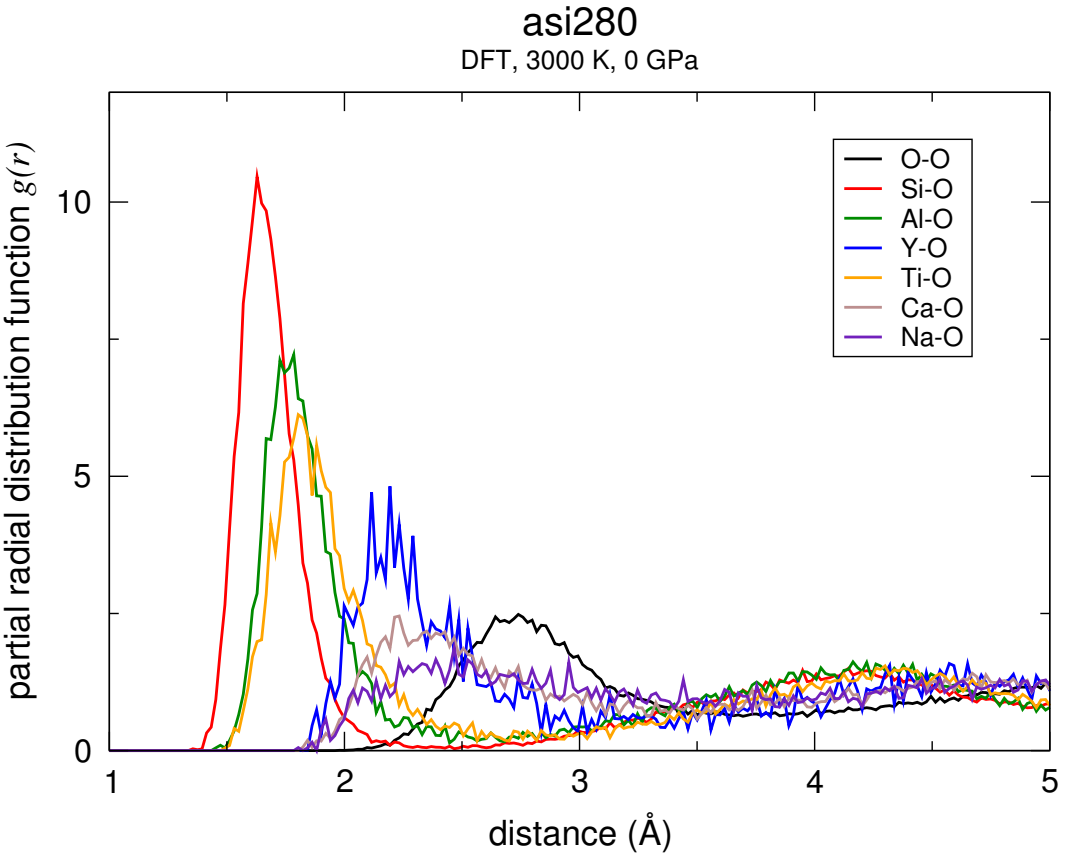

Figure 6.3: Partial radial distribution functions of the asi280 melt doped with one Y, derived from first-principles MD at 3000 K and 0 GPa.

melt	composition
granite	$Si_{26}Al_{4-X}Ca_3Na_6O_{64}A_X$
granite^{super}	$Si_{208}Al_{32-X}Ca_{24}Na_{48}O_{512}A_X$
gabbro	$Si_{18}Al_{3-X}Mg_{18}Ca_4Na_8O_{63}A_X$
gabbro^{super}	$Si_{144}Al_{24-X}Mg_{144}Ca_{32}Na_8O_{504}A_X$
asi200	$Si_{19}Al_{2-X}Ti_5Ca_6Na_{10}O_{62}A_X$
asi280	$Si_{18}Al_{6-X}Ti_5Ca_5Na_4O_{62}A_X$

Table 6.2: Chemical composition of all investigated melts. X is either 0, 1 or 2 (only in gabbro and granite). In gabbro and granite, A can be Y, La and As. In asi200 and asi280, only Y has been investigated.

Bibliography

Adjaoud O, Steinle-Neumann G, Jahn S (2008) Mg_2SiO_4 liquid under high pressure from molecular dynamics. Chem Geol 256:185-192, DOI 10.1016/j.chemgeo.2008.06.031

Adjaoud O, Steinle-Neumann G, Jahn S (2011) Transport properties of Mg_2SiO_4 liquid at high pressure: Physical state of a magma ocean. Earth Planet Sci Lett 312:463-470, DOI 10.1016/j.epsl.2011.10.025

Adjaoud O, Marquardt K, Jahn S (2012) Atomic structures and energies of grain boundaries in Mg_2SiO_4 forsterite from atomistic modeling. Phys Chem Miner 39:749-760, DOI 10.1007/s00269-012-0529-5

Aguado A, Bernasconi L, Madden PA (2003) Interionic potentials from ab initio molecular dynamics: The alkaline earth oxides CaO, SrO and BaO. J Chem Phys 118:5704-5717, DOI 10.1063/1.1556074

Alfè D, Gillan MJ, Price GD (2002) Composition and temperature of the Earth's core constrained by combining ab initio calculations and seismic data. Earth Planet Sci Lett 195:91-98, DOI 10.1016/S0012-821X(01)00568-4

Allan NL, Du Z, Lavrentiev MY, Blundy JD, Purton JA, van Westrenen W (2003) Atomistic simulation of mineral-melt trace-element partitioning. Phys Earth Planet Int 139:93-111, DOI 10.1016/S0031-9201(03)00147-X

Allen MP, Tildesley DJ (1987) Computer simulations of liquids. Oxford University Press Inc., New York

Ammann MW, Brodholt JP, Dobson DP (2010) Simulating diffusion. Rev Mineral Geochem 71:201-224, DOI 10.2138/rmg.2010.71.10

Ashcroft NW, Mermin ND (1976) Solid State Physics. Thomson Learning, Inc.

Beattie P, Drake M, Jones J, Leeman W, Longhi J, McKay G, Nielsen R, Palme H, Shaw D, Takahashi E, Watson B (1993) Terminology for

trace-element partitioning. Geochim Cosmochim Acta 57:1605-1606, DOI 10.1016/0016-7037(93)90015-O

Becke AD (1993) Density-functional thermochemistry. III. The role of exact exchange. J Chem Phys 98:5648-5652, DOI 10.1063/1.464913

van Beest BWH, Kramer GJ, van Santen RA (1990) Force fields for silicas and aluminophosphates based on *ab initio* calculations. Phys Rev Lett 64:1955–1958, DOI 10.1103/PhysRevLett.64.1955

Beyer C, Berndt J, Tappe S, Klemme S (2013) Trace element partitioning between perovskite and kimberlite to carbonatite melt: New experimental constraints. Chem Geol 353:132-139, DOI 10.1016/j.chemgeo.2012.03.025

Blundy J, Wood B (1994) Prediction of crystal-melt partition coefficients from elastic moduli. Nature 372:452-454, DOI 10.1038/372452a0

Blundy J, Wood B (2003) Partitioning of trace elements between crystals and melts. Earth Planet Sci Lett 210:383-397, DOI 10.1016/S0012-821X(03)00129-8

Bois L, Barré N, Guittet MJ, Guillopé S, Trocellier P, Gautier-Soyer M, Verdier P, Laurent Y (2002) Aqueous corrosion of lanthanum aluminosilicate glasses: influence of inorganic anions. J Nucl Mater 300:141-150, DOI 10.1016/S0022-3115(01)00748-6

Bussi G, Donadio D, Parrinello M (2007) Canonical sampling through velocity rescaling. J Chem Phys 126:014101, DOI 10.1063/1.2408420

Car R, Parrinello M (1985) Unified approach for molecular dynamics and density-functional theory. Phys Rev Lett 55:2471-2474, DOI 10.1103/PhysRevLett.55.2471

Chakraborty S, Farver JR, Yund RA, Rubie DC (1994) Mg tracer diffusion in synthetic forsterite and San Carlos olivine as a function of P, T and fO_2. Phys Chem Mineral 21:489–500, DOI 10.1007/BF00203923

Chuvil'deev VN (1996) Micromechanism of deformation-stimulated grain-boundary self-diffusion: I. Effect of excess free volume on the free energy and diffusion parameters of grain boundaries. Phys Met Metallogr 81:463-468

Chuvil'deev VN, Kopylov VI, Zeiger W (2002) A theory of non-equilibrium grain boundaries and its applications to nano- and micro-crystalline materials processed by ECAP. Ann Chim-Sci Mat 27:55-64

Clayden NJ, Esposito S, Aronne A, Pernice P (1999) Solid state ^{27}Al NMR and FTIR study of lanthanum aluminosilicate glasses. J Non-Cryst Solids 258:11-19, DOI 10.1016/S0022-3093(99)00555-4

Condit RH, Weed HC, Piwinskii AJ (1985) A technique for observing oxygen diffusion along grain boundary regions in synthetic forsterite, American Geophysical Union, pp 97–105. DOI 10.1029/GM031p0097

Corgne A, Wood BJ (2002) $CaSiO_3$ and $CaTiO_3$ perovskite-melt partitioning of trace elements: Implications for gross mantle differentiation. Geophys Res Lett 29:39-1–39-4, DOI 10.1029/2001GL014398

Corgne A, Armstrong LS, Keshav S, Fei Y, McDonough WF, Minarik WG, Moreno K (2012) Trace element partitioning between majoritic garnet and silicate melt at 10-17 GPa: Implications for deep mantle processes. Lithos 148:128-141, DOI 10.1016/j.lithos.2012.06.013

Davis FA, Humayun M, Hischmann MM, Cooper RS (2013) Experimentally determined mineral/melt partitioning of first-row transition elements (FRTE) during partial melting of peridotite at 3 GPa. Geochim Cosmochim Acta 104:232-260, DOI 10.1016/j.gca.2012.11.009

Demichelis R, Civalleri B, D'Arco P, Dovesi R (2010) Performance of 12 DFT functionals in the study of crystal systems: Al_2SiO_5 orthosilicates and Al hydroxides as a case study. Int J Quantum Chem 110:2260–2273, DOI 10.1002/qua.22574

Dohmen R, Milke R (2010) Diffusion in polycrystalline materials: Grain boundaries, mathematical models, and experimental data. Rev Mineral Geochem 72:921–970, DOI 10.2138/rmg.2010.72.21

Dohmen R, Chakraborty S, Becker HW (2002) Si and O diffusion in olivine and implications for characterizing plastic flow in the mantle. Geophys Res Lett 29:26-1–26-4, DOI 10.1029/2002GL015480

Dohmen R, Becker HW, Chakraborty S (2007) Fe–Mg diffusion in olivine i: experimental determination between 700 and 1,200°C as a function of composition, crystal orientation and oxygen fugacity. Phys Chem Mineral 34:389–407, DOI 10.1007/s00269-007-0157-7

Dreizler RM, Gross EKU (1990) Density Functional Theory. Springer Berlin Heidelberg, DOI 10.1007/978-3-642-86105-5

Drewitt JWE, Hennet L, Zeidler A, Jahn S, Salmon P, Neuville D, Fischer HE (2012) Structural transformations on vitrification in the fragile glass-forming system $CaAl_2O_4$. Phys Rev Lett 109:235501, DOI 10.1103/PhysRevLett.109.235501

Du J (2009) Molecular dynamics simulations of the structure and properties of low silica yttrium aluminosilicate glasses. J Am Ceram Soc 92:87-95, DOI 10.1111/j.1551-2916.2008.02853.x

Dupree R, Lewis MH, Smith ME (1989) A high-resolution NMR study of the La-Si-Al-O-N system. J Am Ceram Soc 111:5125-5132, DOI 10.1021/ja00196a016

Economou EN (2006) Green's Functions in Quantum Physics. Springer Series in Solid-State Sciences, vol 7, Springer, Berlin, Heidelberg, DOI 10.1007/3-540-28841-4

Evans TM, O'Neill HSC, Tuff J (2008) The influence of melt composition on the partitioning of REEs, Y, Sc, Zr and Al between forsterite and melt in the system CMAS. Geochim Cosmochim Acta 72:5708-5721, DOI 10.1016/j.gca.2008.09.017

Faber TE, Ziman JM (1965) A Theory of the Electrical Properties of Liquid Metals III. The Resistivity of Binary Alloys. Phil Mag 11:153-173, DOI 10.1080/14786436508211931

Farber DL, Williams Q, Ryerson FJ (1994) Diffusion in Mg_2SiO_4 polymorphs and chemical heterogeneity in the mantle transition zone. Nature 371:693–695, DOI 10.1038/371693a0

Farver JR, Yund RA (2000) Silicon diffusion in forsterite aggregates: Implications for diffusion accommodated creep. Geophys Res Lett 27:2337–2340, DOI 10.1029/2000GL008492

Farver JR, Yund RA, Rubie DC (1994) Magnesium grain boundary diffusion in forsterite aggregates at 1000-1300°C and 0.1 MPa to 10 GPa. J Geophys Res-Solid 99:19809–19819, DOI 10.1029/94JB01250

Fei H, Hegoda C, Yamazaki D, Wiedenbeck M, Yurimoto H, Shcheka S, Katsura T (2012) High silicon self-diffusion coefficient in dry forsterite. Earth Planet Sci Lett 345–348:95-103, DOI 10.1016/j.epsl.2012.06.044

Fei H, Wiedenbeck M, Yamazaki D, Katsura T (2013) Small effect of water on upper-mantle rheology based on silicon self-diffusion coefficients. Nature 498:213–215, DOI 10.1038/nature12193

Fei H, Koizumi S, Sakamoto N, Hashiguchi M, Yurimoto H, Marquardt K, Miyajima N, Yamazaki D, Katsura T (2016) New constraints on upper mantle creep mechanism inferred from silicon grain-boundary diffusion rates. Earth Planet Sci Lett 433:350-359, DOI 10.1016/j.epsl.2015.11.014

Finkelstein GJ, Dera PK, Jahn S, Oganov AR, Holl CM, Meng Y, Duffy TS (2014) Phase transitions and equation of state of forsterite to 90 GPa from single-crystal x-ray diffraction and molecular modeling. Am Mineral 99:35-43, DOI 10.2138/am.2014.4526

Fischer HE, Cuello GJ, Palleau P, Feltin D, Barnes AC, Badyal YS, Simonson JM (2002) D4c: A very high precision diffractometer for disordered materials. Appl Phys A 74:S160-S162, DOI 10.1007/s003390101087

Fischer HE, Barnes AC, Salmon PS (2006) Neutron and x-ray diffraction studies of liquids and glasses. Rep Prog Phys 69:233-299, DOI 10.1088/0034-4885/69/1/R05

Fisler DK, Mackwell SJ (1994) Kinetics of diffusion-controlled growth of fayalite. Phys Chem Mineral 21:156–165, DOI 10.1007/BF00203146

Florian P, Sadiki N, Massiot D, Coutures JP (2007) ^{27}Al NMR study of the structure of lanthanum- and yttrium-based aluminosilicate glasses and melts. J Phys Chem B 111:9747-9757, DOI 10.1021/jp072061q

Frenkel D, Smit B (2002) Understanding molecular simulation: from algorithms to applications. Academic Press, San Diego

Fumi FG, Tosi MP (1964) Ionic sizes and born repulsive parameters in the NaCl-type alkali halides—I: The Huggins-Mayer and Pauling forms. J Phys Chem Solids 25:31-43, DOI 10.1016/0022-3697(64)90159-3

Gardés E, Wunder B, Marquardt K, Heinrich W (2012) The effect of water on intergranular mass transport: new insights from diffusion-controlled reaction rims in the MgO–SiO_2 system. Contrib Mineral Petrol 164:1–16, DOI 10.1007/s00410-012-0721-0

Ghosh DB, Karki BB (2013) First principles simulations of the stability and structure of grain boundaries in Mg_2SiO_4 forsterite. Phys Chem Miner 41:163–171, DOI 10.1007/s00269-013-0633-1

Gillan MJ, Alfè D, Brodholt J, Vocadlo L, Price GD (2006) First-rinciples modelling of Earth and planetary materials at high pressures and temperatures. Rep Prog Phys 69:2365-2441

Girnis AV, Bulatov VK, Brey GP, Gerdes A, Höfer HE (2013) Trace element partitioning between mantle minerals and silico-carbonate melts at 6-12 GPa and applications to mantle metasomatism and kimberlite genesis. Lithos 160-161:183-200, DOI 10.1016/j.lithos.2012.11.027

Goedecker S, Teter M, Hutter J (1996) Separable dual-space Gaussian pseudopotentials. Phys Rev B 54:1703–1710, DOI 10.1103/PhysRevB.54.1703

Goldschmidt VM (1937) The principles of distribution of chemical elements in minerals and rocks. J Chem Soc pp 655–673, DOI 10.1039/JR9370000655

Green TH (1994) Experimental studies of trace-element partitioning applicable to igneous petrogenesis - Sedona 16 years later. Chem Geol 117:1-36, DOI 10.1016/0009-2541(94)90119-8

Gurmani SF, Jahn S, Brasse H, Schilling FR (2011) Atomic scale view on partially molten rocks: Molecular dynamics simulations of melt-wetted olivine grain boundaries. J Geophys Res 116:B12209, DOI 10.1029/2011JB008519

Haigis V (2013) Trace elements in silicate melts and the thermal conductivity of the earth's deep mantle: insights from atomistic modeling of geomaterials. PhD thesis, Freie Universität Berlin

Haigis V, Salanne M, Simon S, Wilke M, Jahn S (2013) Molecular dynamics simulations of Y in silicate melts and implications for trace element partitioning. Chem Geol 346:14-21, DOI 10.1016/j.chemgeo.2012.08.021

Hammersley AP, Svensson SO, Hanfland M, Fitch AN, Häusermann D (1996) Two-dimensional detector software: From real detector to idealised image or two-theta scan. High Pressure Res 14:235-248, DOI 10.1080/08957959608201408

Hansen LN, Zimmerman ME, Kohlstedt DL (2012) The influence of microstructure on deformation of olivine in the grain-boundary sliding regime. J Geophys Res-Solid 117:B09201, DOI 10.1029/2012JB009305

Harding JH, Pyper NC (1995) The meaning of the oxygen second-electron affinity and oxide potential models. Phil Mag Lett 71:113-121, DOI 10.1080/09500839508241003

Hartmann K, Wirth R, Markl G (2008) P-T-X-controlled element transport through granulite-facies ternary feldspar from Lofoten, Norway. Contrib Mineral Petrol 156:359–375, DOI 10.1007/s00410-008-0290-4

Hennet L, Thiaudière D, Gailhanou M, Landron C, Coutures JP, Price DL (2002) Fast x-ray scattering measurements on molten alumina using a 120 degrees curved position sensitive detector. Rev Sci Instrum 73:124-129, DOI 10.1063/1.1426228

Hirth G, Kohlstedt D (2013) Rheology of the upper mantle and the mantle wedge: A view from the experimentalists, American Geophysical Union, pp 83–105. DOI 10.1029/138GM06

Hohenberg P, Kohn W (1964) Inhomogeneous electron gas. Phys Rev 136:B864-B871, DOI 10.1103/PhysRev.136.B864

Hoover WG (1985) Canonical dynamics: Equilibrium phase-space distributions. Phys Rev A 31:1695-1697, DOI 10.1103/PhysRevA.31.1695

Huang F, Lundstrom CC, McDonough WF (2006) Effect of melt structure on trace-element partitioning between clinopyroxene and silicic, alkaline, aluminous melts. Am Mineral 91:1385-1400, DOI 10.2138/am.2006.1909

Hult E, Rydberg H, Lundqvist BI, Langreth DC (1999) Unified treatment of asymptotic van der Waals forces. Phys Rev B 59:4708–4713, DOI 10.1103/PhysRevB.59.4708

Hutter J, Iannuzzi M, Schiffmann F, VandeVondele J (2014) CP2K : atomistic simulations of condensed matter systems. Wiley Interdiscip Rev Comput Mol Sci 4:15-25, DOI 10.1002/wcms.1159

Ibers JA, Hamilton WC (eds) (1974) International tables for x-ray crystallography, vol 4. The Kynoch Press, Birmingham

Iftekhar S, Leonova E, Edén M (2009) Structural characterization of lanthanum aluminosilicate glasses by ^{29}Si solid-state NMR. J Non-Cryst Solids 355:2165-2174, DOI 10.1016/j.jnoncrysol.2009.06.031

Iftekhar S, Grins J, Gunwidjaja PN, Edén M (2011) Glass formation and structure-property-composition relations of the RE_2O_3-Al_2O_3-SiO_2 (RE = La, Y, Lu, Sc) systems. J Am Ceram Soc 94:2429-2435, DOI 10.1111/j.1551-2916.2011.04548.x

Iftekhar S, Pahari B, Okhotnikov K, Jaworski A, Stevensson B, Grins J, Edén M (2012) Properties and structures of RE_2O_3-Al_2O_3-SiO_2 (RE = Y, Lu) glasses probed by molecular dynamics simulations and solid-state NMR: the roles of aluminum and rare-earth ions for dictating the microhardness. J Phys Chem C 116:18394-18406, DOI 10.1021/jp302672b

Ikuhara Y, Nishimura H, Nakamura A, Matsunaga K, Yamamoto T, Lagerlöf KPD (2003) Dislocation structures of low-angle and near-Σ3 grain boundaries in alumina bicrystals. J Am Ceram Soc 86:595–602, DOI 10.1111/j.1151-2916.2003.tb03346.x

Jahn S (2010) Integral modeling approach to study the phase behavior of complex solids: Application to phase transitions in $MgSiO_3$ pyroxenes. Acta Crystallogr A66:535-541, DOI 10.1107/S0108767310026449

Jahn S, Madden PA (2007) Modeling Earth materials from crustal to lower mantle conditions: A transferable set of interaction potentials for the CMAS system. Phys Earth Planet Int 162:129-139, DOI 10.1016/j.pepi.2007.04.002

Jahn S, Madden PA (2008) Atomic dynamics of alumina melt: A molecular dynamics simulation study. Condens Matter Phys 11:169-178, DOI 10.5488/CMP.11.1.169

Jahn S, Martoňák R (2008) Plastic deformation of orthoenstatite and the ortho- to high-pressure clinoenstatite transition: A metadynamics simulation study. Phys Chem Miner 35:17-23, DOI 10.1007/s00269-007-0194-2

Jaworski A, Stevensson B, Pahari B, Okhotnikov K, Edén M (2012) Local structures and Al/Si ordering in lanthanum aluminosilicate glasses explored by advanced ^{27}Al NMR experiments and molecular dynamics simulations. Phys Chem Chem Phys 14:15866-15878, DOI 10.1039/c2cp42858j

Karato S, Wu P (1993) Rheology of the upper mantle: A synthesis. Science 260:771–778, DOI 10.1126/science.260.5109.771

Keller LM, Wirth R, Rhede D, Kunze K, Abart R (2008) Asymmetrically zoned reaction rims: assessment of grain boundary diffusivities and growth rates related to natural diffusion-controlled mineral reactions. J Metamorph Geol 26:99–120, DOI 10.1111/j.1525-1314.2007.00747.x

Kirkwood JG (1935) Statistical mechanics of fluid mixtures. J Chem Phys 3:300-313, DOI 10.1063/1.1749657

Klein M, Stosch HG, Seck HA, Shimizu N (2000) Experimental partitioning of high field strength and rare earth elements between clinopyroxene and garnet in andesitic to tonalitic systems. Geochim Cosmochim Acta 64:99-115, DOI 10.1016/S0016-7037(99)00178-7

Kohli JT, Shelby JE (1991) Magneto-optical properties of rare-earth aluminosilicate glasses. Phys Chem Glasses 32:109-114, DOI n/a

Kohn SC, Schofield PF (1994) Trace-element partitioning with application to magmatic processes the importance of melt composition in controlling trace-element behaviour: an experimental study of Mn and Zn partitioning between forsterite and silicate melts. Chem Geol 117:73-87, DOI 10.1016/0009-2541(94)90122-8

Kohn W, Sham LJ (1965) Self-consistent equations including exchange and correlation effects. Phys Rev 140:A1133-A1138, DOI 10.1103/PhysRev.140.A1133

de Koker N, Karki BB, Stixrude L (2013) Thermodynamics of the MgO-SiO_2 liquid system in Earth's lowermost mantle from first principles. Earth Planet Sci Lett 361:58-63, DOI 10.1016/j.epsl.2012.11.026

Kubo T, Shimojuku A, Ohtani E (2004) Mg–Fe interdiffusion rates in wadsleyite and the diffusivity jump at the 410-km discontinuity. Phys Chem Miner 31:456–464, DOI 10.1007/s00269-004-0412-0

Labiche JC, Mathon O, Pascarelli S, Newton MA, Ferre GG, Curfs C, Vaughan G, Homs A, Carreiras DF (2007) The fast readout low noise camera as a versatile x-ray detector for time resolved dispersive extended x-ray absorption fine structure and diffraction studies of dynamic problems in materials science, chemistry, and catalysis. Rev Sci Instrum 78:09130, DOI 10.1063/1.2783112

Laio A, Bernard S, Chiarotti GL, Scandolo S, Tosatti E (2000) Physics of iron at earth's core conditions. Science 287:1027–1030, DOI 10.1126/science.287.5455.1027

Lantelme F, Turq P (1982) Ionic dynamics in the LiCl–KCl system at liquid state. J Chem Phys 77:3177-3187, DOI 10.1063/1.444192

Lee C, Yang W, Parr RG (1988) Development of the Colle-Salvetti correlation-energy formula into a functional of the electron density. Phys Rev B 37:785–789, DOI 10.1103/PhysRevB.37.785

Lee SK, Stebbins JF (2006) Disorder and the extent of polymerization in calcium silicate and aluminosilicate glasses: O-17 NMR results and quantum chemical molecular orbital calculations. Geochim Cosmochim Acta 70:4275-4286, DOI 10.1016/j.gca.2006.06.1550

Leydier M (2010) Méthodes complémentaires pour l'étude de verres et liquides fondus sur grands instruments. PhD thesis, Université d'Orléans

Loewenstein W (1954) The distribution of aluminum in the tetrahedra of silicates and aluminates. Am Mineral 39:92-96

Madden PA, Heaton R, Aguado A, Jahn S (2006) From first-principles to material properties. J Mol Struc-THEOCHEM 771:9-18, DOI 10.1016/j.theochem.2006.03.015

Marchi J, Morais DS, Schneider J, Bressiani JC, Bressiani AHA (2005) Characterization of rare earth aluminosilicate glasses. J Non-Cryst Solids 351:863-868, DOI 10.1016/j.jnoncrysol.2005.01.078

Marquardt K, Petrishcheva E, Gardés E, Wirth R, Abart R, Heinrich AJ (2011) Grain boundary and volume diffusion experiments in yttrium aluminium garnet bicrystals at 1,723 K: a miniaturized study. Contrib Mineral Petrol 162:739-749, DOI 10.1007/s00410-011-0622-7

Marquardt K, Rohrer GS, Morales L, Rybacki E, Marquardt H, Lin B (2015) The most frequent interfaces in olivine aggregates: the gbcd and its importance for grain boundary related processes. Contrib Mineral Petrol 170:1–17, DOI 10.1007/s00410-015-1193-9

Martyna GJ, Tobias DJ, Klein ML (1994) Constant pressure molecular dynamics algorithms. J Chem Phys 101:4177-4189, DOI 10.1063/1.467468

Marx D, Hutter J (2000) Ab initio molecular dynamics: Theory and implementation. In: Grotendorst J (ed) Modern Methods and Algorithms of Quantum Chemistry, Forschungszentrum Jülich, NIC Series, vol 1, pp 301–449

Marx D, Hutter J (2012) Ab initio molecular dynamics: Basic Theory and Advanced Methods. Cambridge University Press

Marzari N, Vanderbilt D (1997) Maximally localized generalized Wannier functions for composite energy bands. Phys Rev B 56:12847-12865

Massiot D, Trumeau D, Touzo B, Farnan I, Rifflet JC, Douy A, Coutures JP (1995) Structure and Dynamics of $CaAl_2O_4$ from liquid to glass: a high-temperature ^{27}Al NMR time-resolved study. J Phys Chem 99:16455-16459, DOI 10.1021/j100044a038

McQuarrie DA (2000) Statistical mechanics. University Science Books, Sausalito

Mysen B, Richet P (2005) Silicate glasses and melts. Properties and Structure. Elsevier, Amsterdam

Mysen BO (2004) Element partitioning between minerals and melts, melt composition, and melt structure. Chem Geol 213:1-16, DOI 10.1016/j.chemgeo.2004.08.028

Nosé S (1984) A molecular dynamics method for simulations in the canonical ensemble. Mol Phys 52:255-268, DOI 10.1080/00268978400101201

Nosé S, Klein ML (1983) Constant pressure molecular dynamics for molecular systems. Mol Phys 50:1055-1076, DOI 10.1080/00268978300102851

Okhotnikov K, Stevensson B, Edén M (2013) New interatomic potential parameters for molecular dynamics simulations of rare-earth (RE = La, Y, Lu, Sc) aluminosilicate glass structures: exploration of field-strength effects. Phys Chem Chem Phys 15:15041-15055, DOI 10.1039/C3CP51726H

O'Neill HSC, Eggins SM (2002) The effect of melt composition on trace element partitioning: an experimental investigation of the activity coefficients of FeO, NiO, CoO, MoO_2 and MoO_3 in silicate melts. Chem Geol 186:151-181, DOI 10.1016/S0009-2541(01)00414-4

Parr RG, Yang W (1989) Density-functional theory of atoms and molecules. Oxford University Press

Perdew JP, Chevary JA, Vosko SH, Jackson KA, Pederson MR, Singh DJ, Fiolhais C (1992) Atoms, molecules, solids, and surfaces: Applications of the generalized gradient approximation for exchange and correlation. Phys Rev B 46:6671–6687, DOI 10.1103/PhysRevB.46.6671

Perdew JP, Burke K, Ernzerhof M (1996) Generalized gradient approximation made simple. Phys Rev Lett 77:3865–3868, DOI 10.1103/PhysRevLett.77.3865

Pertermann M, Hirschmann MM, Hametner K, Günther D, Schmidt MW (2004) Experimental determination of trace element partitioning between garnet and silica-rich liquid during anhydrous partial melting of MORB-like eclogite. Geochem Geophys Geosyst 5:Q05A01, DOI 10.1029/2003GC000638

Petegem SV, Torre FD, Segers D, Swygenhoven HV (2003) Free volume in nanostructured Ni. Scripta Mater 48:17-22, DOI 10.1016/S1359-6462(02)00322-6

Pommier A, Leinenweber K, Kohlstedt DL, Qi C, Garnero EJ, Mackwell SJ, Tyburczy JA (2015) Experimental constraints on the electrical anisotropy of the lithosphere-asthenosphere system. Nature 522:202–206, DOI 10.1038/nature14502

Pozdnyakova I, Sadiki N, Hennet L, Cristiglio V, Bytchkov A, Cuello GJ, Coutures JP, Price DL (2008) Structures of lanthanum and yttrium aluminosilicate glasses determined by x-ray and neutron diffraction. J Non-Cryst Solids 354:2038-2044, DOI 10.1016/j.jnoncrysol.2007.11.012

Press WH, Flannery BP, Teukolski SA, Vetterling WT (1992) Numerical Recipes. Cambridge University Press

Price GD, Parker SC, Leslie M (1987) The lattice dynamics and thermodynamics of the Mg_2SiO_4 polymorphs. Phys Chem Minerals 15:181–190, DOI 10.1007/BF00308782

Prowatke S, Klemme S (2005) Effect of melt composition on the partitioning of trace elements between titanite and silicate melt. Geochim Cosmochim Acta 69:695-709, DOI 10.1016/j.gca.2004.06.037

Purton JA, Allan NL, Blundy JD (1997) Calculated solution energies of heterovalent cations in forsterite and diopside: Implications for trace element partitioning. Geochim Cosmochim Acta 61:3927-3936, DOI 10.1016/S0016-7037(97)00198-1

Purton JA, Blundy JD, Allan NL (2000) Computer simulation of high-temperature, forsterite-melt partitioning. Am Mineral 85:1087-1091, DOI 10.2138/am-2000-0726

Muñoz Ramo D, Stixrude L (2014) Spin crossover in Fe_2SiO_4 liquid at high pressure. Geophys Res Lett 41:4512-4518, DOI 10.1002/2014GL060473

Ringwood AE (1966) Chemical evolution of the terrestrial planets. Geochim Cosmochim Acta 30:41-104, DOI 10.1016/0016-7037(66)90090-1

Rowley AJ, Jemmer P, Wilson M, Madden PA (1998) Evaluation of the many-body contributions to the interionic interactions in MgO. J Chem Phys 108:10209-10219, DOI 10.1063/1.476481

Salanne M, Rotenberg B, Jahn S, Vuilleumier R, Simon C, Madden P (2012a) Including many-body effects in models for ionic liquids. Theor Chem Acc 131:1143, DOI 10.1007/s00214-012-1143-9

Salanne M, Siqueira LJA, Seitsonen AP, Madden PA, Kirchner B (2012b) From molten salts to room temperature ionic liquids: Simulation studies on chloroaluminate systems. Faraday Discuss 154:171-188, DOI 10.1039/C1FD00053E

Schaller T, Stebbins JF (1998) The structural role of lanthanum and yttrium in aluminosilicate glasses: A ^{27}Al and ^{17}O MAS NMR study. J Phys Chem B 102:10690-10697, DOI 10.1021/jp982387m

Schmidt MW, Connolly JAD, Günther D, Bogaerts M (2006) Element partitioning: the role of melt structure and composition. Science 312:1646-1650, DOI 10.1126/science.1126690

Sears VF (1992) Neutron scattering lengths and cross sections. Neutron News 3:26-37, DOI 10.1080/10448639208218770

Shannon RD (1976) Revised effective ionic radii and systematic studies of interatomic distances in halides and chalcogenides. Acta Cryst A32:751-767, DOI 10.1107/S0567739476001551

Shaw DM (2006) Trace elements in magmas. A theoretical treatment. Cambridge University Press, Cambridge

Shelby JE, Kohli JT (1990) Rare-earth aluminosilicate glasses. J Am Ceram Soc 73:39-42, DOI 10.1111/j.1151-2916.1990.tb05087.x

Sherrill CD, Schaefer III HF (1999) The configuration interaction method: Advances in highly correlated approaches. Advances in Quantum Chemistry, vol 34, Academic Press, pp 143–269, DOI 10.1016/S0065-3276(08)60532-8

Shewchuk JR (1994) An Introduction to the Conjugate Gradient Method Without the Agonizing Pain. Tech. rep., Pittsburgh, PA, USA

Shimojuku A, Kubo T, Ohtani E, Yurimoto H (2004) Silicon self-diffusion in wadsleyite: Implications for rheology of the mantle transition zone and subducting plates. Geophys Res Lett 31:L13606, DOI 10.1029/2004GL020002

Shimojuku A, Kubo T, Ohtani E, Nakamura T, Okazaki R, Dohmen R, Chakraborty S (2009) Si and O diffusion in $(Mg,Fe)_2SiO_4$ wadsleyite and ringwoodite and its implications for the rheology of the mantle transition zone. Earth Planet Sci Lett 284:103-112, DOI 10.1016/j.epsl.2009.04.014

Silvestrelli PL, Parrinello M (1999) Water Molecule Dipole in the Gas and in the Liquid Phase. Phys Rev Lett 82:3308–3311, DOI 10.1103/PhysRevLett.82.3308

Simon S, Wilke M, Chernikov R, Klemme S, Hennet L (2013) The influence of composition on the local structure around yttrium in quenched silicate melts — Insights from EXAFS. Chem Geol 346:3–13, DOI 10.1016/j.chemgeo.2012.09.017

Spiekermann G, Wilke M, Sandro J (2016) Structural and dynamical properties of supercritical H_2O–SiO_2 fluids studied by ab initio molecular dynamics. Chem Geol 426:85 - 94, DOI 10.1016/j.chemgeo.2016.01.010

Stalder R, Foley SF, Brey GP, Horn I (1998) Mineral-aqueous fluid partitioning of trace element at 900-1200°C and 3.0-5.7 GPa: New experimental data for garnet, clinopyroxene, and rutile, and implications for mantle metasomatism. Geochim Comsochim Acta 62:1781-1801, DOI 10.1016/S0016-7037(98)00101-X

Stebbins JF, McMillan PE, Dingwell DB (eds) (1995) Structure, dynamics and properties of silicate melts. Mineralogical Society of America, Washington DC

Stebbins JF, Dubinsky EV, Kanehashi K, Kelsey KE (2008) Temperature effects on non-bridging oxygen and aluminum coordination number in calcium aluminosilicate glasses and melts. Geochim Cosmochim Acta 72:910-925

Stone AJ (1996) The theory of intermolecular forces. Oxford University Press Inc., New York

Stone AJ (2008) Intermolecular potentials. Science 321:787–789, DOI 10.1126/science.1158006

Stukowski A (2010) Visualization and analysis of atomistic simulation data with OVITO – the Open Visualization Tool. Model Simul Mater Sc 18:015012, DOI 10.1088/0965-0393/18/1/015012

Sun C, Liang Y (2011) Distribution of REE between clinopyroxene and basaltic melt along a mantle adiabat: effects of major element composition, water, and temperature. Contrib Mineral Petrol 163:807–823, DOI 10.1007/s00410-011-0700-x

Sun C, Liang Y (2013) The importance of crystal chemistry on REE partitioning between mantle minerals (garnet, clinopyroxene, orthopyroxene, and olivine) and basaltic melts. Chem Geol 358:23-36, DOI 10.1016/j.chemgeo.2013.08.045

Tanabe S (1999) Optical transitions of rare earth ions for amplifiers: how the local structure works in glass. J Non-Cryst Solids 259:1-9, DOI 10.1016/S0022-3093(99)00490-1

Tang KT, Toennies JP (1984) An improved simple model for the van der Waals potential based on universal damping functions for the dispersion coefficients. J Chem Phys 80:3726-3741, DOI 10.1063/1.447150

Tosi MP, Fumi FG (1964) Ionic sizes and born repulsive parameters in the NaCl-type alkali halides—II: The generalized Huggins-Mayer form. J Phys Chem Solids 25:45-52, DOI 10.1016/0022-3697(64)90160-X

Troullier N, Martins JL (1991) Efficient pseudopotentials for plane-wave calculations. Phys Rev B 43:1993-2005, DOI 10.1103/PhysRevB.43.1993

Tucker GJ, McDowell DL (2011) Non-equilibrium grain boundary structure and inelastic deformation using atomistic simulations. Int J Plasticity 27:841-857, DOI 10.1016/j.ijplas.2010.09.011

VandeVondele J, Hutter J (2007) Gaussian basis sets for accurate calculations on molecular systems in gas and condensed phases. J Chem Phys 127:114105, DOI 10.1063/1.2770708

VandeVondele J, Krack M, Mohamed F, Parrinello M, Chassaing T, Hutter J (2005) Quickstep: Fast and accurate density functional calculations using a mixed Gaussian and plane waves approach. Comput Phys Commun 167:103-128, DOI 10.1016/j.cpc.2004.12.014

Veksler IV, Dorfman AM, Danyushevsky LV, Jakobsen JK, Dingwell DB (2006) Immiscible silicate liquid partition coefficients: implications for crystal-melt element partitioning and basalt petrogenesis. Contrib Mineral Petrol 152:685–702, DOI 10.1007/s00410-006-0127-y

Wannberg A, Mellergård A, Zetterström P, Delaplane R, M Grönros LEK, McGreevy R (1999) SLAD: A Neutron Diffractometer for the Study of Disordered Materials. J Neutron Res 8:133-154, DOI 10.1080/10238169908200050

Watson EB (1986) An experimental study of oxygen transport in dry rocks and related kinetic phenomena. J Geophys Res-Solid 91:14117–14131, DOI 10.1029/JB091iB14p14117

Watson GW, Oliver PM, Parker SC (1997) Computer simulation of the structure and stability of forsterite surfaces. Phys Chem Mineral 25:70-78, DOI 10.1007/s002690050088

van Westrenen W, Draper DS (2007) Quantifying garnet-melt trace element partitioning using lattice-strain theory: new crystal-chemical and thermodynamic constraints. Contrib Mineral Petrol 154:717–730, DOI 10.1007/s00410-007-0222-8

van Westrenen W, Allan NL, Blundy JD, Purton JA, Wood BJ (2000) Atomistic simulation of trace element incorporation into garnets - comparison

with experimental garnet-melt partitioning data. Geochim Cosmochim Acta 64:1629-1639, DOI 10.1016/S0016-7037(00)00336-7

van Westrenen W, Wood BJ, Blundy JD (2001) A predictive thermodynamic model of garnet–melt trace element partitioning. Contrib Mineral Petrol 142:219–234, DOI 10.1007/s004100100285

Wilding MC, Benmore CJ, McMillan PF (2002) A neutron diffraction study of yttrium- and lanthanum-aluminate glasses. J Non-Cryst Solids 297:143-155, DOI 10.1016/S0022-3093(01)00933-4

Wilson M, Madden PA (1993) Polarization effects in ionic systems from first principles. J Phys: Condens Mat 5:2687-2706, DOI 10.1088/0953-8984/5/17/004

Wood BJ, Blundy JD (1997) A predictive model for rare earth element partitioning between clinopyroxene and anhydrous silicate melt. Contrib Mineral Petrol 129:166-181, DOI 10.1007/s004100050330

Acknowledgements

I would like to thank first and foremost Prof Dr Sandro Jahn who has tirelessly guided my through my entire PhD. His example on how to faithfully conduct high quality research has inspired me to stick to science and keep on working on the publications that make up this thesis. He has introduced me to all theoretical and practical aspect of molecular modelling and I could never have wished for better support during the entire course of my PhD.
I would also like to thank all my co-workers at GFZ Potsdam who have always provided advice and a very pleasant and inviting environment to work in. Many thanks go to Volker Haigis, Katharina Marquardt, Daniela Künzel and Omar Adjaoud for reading and improving the manuscripts of this thesis.
A special thanks goes to Julia Pohlenz, Roman Rahner and Novid Ghassemi as well as my family, who have always silently stood by my side, providing me with the energy needed to go through the writing of this thesis, never tiring to withstand my bad moods.

Erklärung der Eigenständigkeit

Ich versichere hiermit an Eides statt, dass diese Arbeit von niemand anderem als meiner Person verfasst worden ist. Alle verwendeten Hilfsmittel wie Berichte, Bücher, Internetseiten oder ähnliches sind im Literaturverzeichnis angegeben, Zitate aus fremden Arbeiten sind als solche kenntlich gemacht. Die Arbeit wurde bisher in gleicher oder ähnlicher Form keiner anderen Prüfungskommission vorgelegt und auch nicht veröffentlicht.

Berlin, Juli 2016

Johannes Wagner